Conduction Processes in Spinel Ferrites.

Peter John Phillips BSc (Hons)

A thesis submitted for the degree of Doctor of Philosophy

July 1991

University of Warwick

Department of Physics
University of Warwick
United Kingdom

This Thesis is dedicated to

My

Parents

Abstract.

An apparatus has been designed, constructed and tested for measurements of resistivity and thermopower, having the following novel features:

I) buffer amplifiers with driven shields to make measurements on highly resistive specimens,

II) "in house" software and hardware developed to automate the measurements and,

III) a new method of temperature measurement for thermopower studies.

Measurements have been carried out on single crystal $Zn_XFe_{3-X}O_4$ and $Mn_XFe_{3-X}O_4$ with $0 \leq X < 1$ in the temperature range 4.2K-300K.

The results strongly suggest that substitutional disorder plays an important role in the electrical transport properties of ferrites. The electrical conductivity for high X near 300K is interpreted in terms of nearest-neighbour hopping. The temperature dependence of $G(\sigma T)=dLn(\sigma T)/d(1/T)$ between 300K and 100K and the concentration dependence of $G(\sigma T)$ at 100K provides evidence for the formation of a Coulomb Gap at low X. At low temperatures, variable-range and many-electron hopping for high and low X respectively is observed. An estimate of the effective radius of the carrier wavefunction is obtained from the conductivity measurements, which at ~ 0.4Å is comparable to that previously deduced for nickel ferrite.

For all X a peak in the thermopower at about 50K was observed. The peak for high X has been attributed to the high temperature limit of variable-range hopping, while for low X interpreted as the transition from activation across a Coulomb Gap to many-electron hopping. In the high temperature range, the temperature variation is shown to be consistent with degenerate statistics for low X and non-degenerate statistics for high X. In the latter case it is possible to extract the dopant concentrations, which compare favourably with the values found by Electron Probe Micro-Analysis (EPMA). The high temperature thermopower and resistivity behaviour have been used to deduce the variation of the energy width of the conduction states, or bandwidth, with X and this is shown to be consistent with the expected behaviour. A polaron energy of ~ 0.04eV is calculated at 300K for high values of X, which compares favourably with previous work.

Declaration.

This thesis is submitted to the University of Warwick in support of my application to the degree of Doctor of Philosophy. It contains an account of my own research carried out in the Department of Physics at Portsmouth Polytechnic and the Department of Physics at University of Warwick during the period September 1985 and June 1991 under the supervision of Dr. T.E. Whall. No part of it has previously been used in a degree thesis submitted to this or any other university. The work described in this thesis is the result of my own research except where specifically acknowledged in the text.

July 1991 Peter J. Phillips.

Contents

		Page
	Abstract	iii
	Declaration	iv
	Contents	v
	Acknowledgements	ix
	List of Figures	x
	List of Tables	xviii
1	INTRODUCTION	1
1.1	Spinel Ferrites	1
1.2	Spinel Ferrite Crystalline Structure	2
1.3	Layout of Thesis	3
2	THEORIES OF CONDUCTION	5
2.1	Introduction	5
2.2	Single-Electron Conduction Models	6
2.2.1	Camphausen, Coey and Chakraverty Model	6
2.2.2	Cullen and Callen	7
2.2.3	Anderson localization	7
2.2.4	Hopping conduction between localized states (Miller-Abrahams)	8
2.2.5	Variable Range Hopping	10
2.2.6	Nearest Neighbour Hopping	13
2.3	Many-Electron Effects	15
2.3.1	Introduction	15
2.3.2	The model of Lorenz and Ihle for Fe_3O_4	16
2.3.3	The Coulomb Gap	17

2.3.4 Transport Properties in the Vicinity of the Coulomb Gap 18
2.3.5 Multi- / Many-Electron Hopping 19
2.4 Small "Dielectric" Polarons 22
2.4.1 Introduction 22
2.4.2 Polaron Size and its Binding Energy 23
2.4.3 Polaron Hopping Motion 24
2.4.4 Polaron Hopping in a Disordered Lattice — Conductivity and Thermopower 25
2.5 Summary 26

3 SURVEY OF PREVIOUS INVESTIGATIONS 27
3.1 Introduction 27
3.2 Early Measurements on Ferrite Samples 28
3.2.1 Cobalt Ferrite $(Co_xFe_{3-x}O_4)$ 28
3.2.2 Nickel Ferrite $(Ni_xFe_{3-x}O_4)$ 30
3.2.3 Zinc Ferrite $(Zn_xFe_{3-x}O_4)$ 33
3.2.4 Manganese Ferrite $(Mn_xFe_{3-x}O_4)$ 34
3.2.5 Titanium Ferrite $(Ti_xFe_{3-x}O_4)$ 36
3.2.6 Fluorine Ferrite $(Fe_3O_{4-x}F_x)$ 38
3.3 Summary 39

4 EXPERIMENTAL WORK 41
4.1 Introduction 41
4.2 Samples Measured 42
4.2.1 Preparation of Samples 43
4.2.2 Characterization of Samples 43

4.3	Sample Holder	44
4.3.1	Choice of Thermopower Technique	45
4.3.2	Thermopower and Resistivity Configurations	46
4.4	Choice of Temperature Sensor	47
4.4.1	Silicon Diodes	48
4.4.2	Calibration of Diodes	49
4.5	PTFE Clamps	50
4.6	Thermal Anchoring	51
4.7	Cryogenic System	53
4.8	Electronics	54
4.8.1	Thermopower Circuits	55
4.8.2	Resistivity Circuit	55
4.9	Driven Shields	56
4.10	Software	56
4.10.1	Thermopower Software	56
4.10.2	Resistivity Software	57
4.10.3	PID Control	58
4.11	Test Results and Conclusion	60
5	RESULTS AND DISCUSSION	61
5.1	Introduction	61
5.2	Reasons for Present Work	61
5.3	Calibration of Apparatus	62
5.4	Outline of Thermopower and Electrical Conductivity Results	64
5.5	Analysis of the Electrical Conductivity Results	65
5.5.1	High Temperatures — $T > T_G$	69

5.5.2 Low Temperatures — T<T_G 71
5.6 Analysis of the Thermopower Results 75
5.6.1 High Temperatures — T>T_S 75
5.6.2 Bandwidth 79
5.6.3 Comparison of G(σT) and ϵII 80
5.6.4 Low Temperatures — T<T_S 81
6 SUMMARY AND CONCLUSION 86
REFERENCES 88

Acknowledgements.

The author in indebted to his supervisor, Dr T.E. Whall, for discussions on experiment and theory and his patience during the writing of this thesis, and to Prof. E.H.C. Parker for encouragement support.

I am grateful to the chairman of the Physics Department, Prof. S. Palmer, for his interest in the work and to the Science and Engineering Research Council for the funding of the studentship.

For the provision of single crystal specimens, my thanks go to Dr. V.A.M. Brabers of Eindhoven University, Holland.

This investigation would have never been completed if it was not for the skillful work of Mr. B.G. Pearcey of Portsmouth Polytechnic who commenced the assembly of the cryostat, and Mr. D. Lawlor in the mechanical workshop at Warwick who patiently completed the apparatus. We also wish to thank Mr. D.J.M. Lee for the machining of the ferrite specimens and Mr. T. Naylor for useful discussions on equipment.

Finally, the author is forever grateful for the support from my parents and brother (Steve) while a student at University.

July 1991 Peter J. Phillips.

List of Figures

		Following Page
1.1	The arrangement of the atoms in a unit cell of a spinel ferrite, showing the fourfold and sixfold coordination positions (Verwey and Heilmann, (1947))	2
2.1	Single electron energy diagram for Fe_3O_4 according to the Camphausen, Coey and Chakraverty model (1972)	6
2.2	A periodic lattice without disorder. (Mott and Davis (1979))	7
2.3	A periodic lattice with vertical disorder. (Mott and Davis (1979))	7
2.4	A Gaussian density of states with a mobility edge showing the localised and extended states. (Mott and Davis (1979))	7
2.5	Two potential wells and their resulting wavefunction states Ψ_a and Ψ_b	9
2.6	A diagram showing three possible high conductance links within a solid	11
2.7	Qualitative behaviour of the short range and long range ordering about the Verwey temperature T_V.	11
2.8	The influence of temperature on the nearest neighbour interactions for magnetite. (Lorenz and Ihle (1975))	16
2.9	A density of states with a Coulomb Gap showing possible peak broadening due to impurities — according to Lorenz and Ihle (1975)	17
2.10	A density of states with a Coulomb Gap according to Pollak and Knotek (1979). Pollak and Knotek predict that v is small but finite whilst Efros and Shklovskii (1975) predict $v=0$	17

2.11 A graph of resistivity against reciprocal temperature showing three temperature regions as defined by Pollak and Knotek (1979) 17
2.12 Polaron–like multi–electron hopping conduction according to Mott (1976) 20
2.13 Correlated multi–electron hopping, according to Pollak and Knotek (1979) 20
2.14 An electron causing lattice deformation: the polarised cloud plus the electron is called a "dielectric" polaron 22
2.15 The displacement of a molecule's energy when an electron is added. (Austin and Mott, 1969) 22

3.1 Room temperature values of log resistivity for a series of mixed crystals of $Co_{3-X}Fe_XO_4$ near the composition $CoFe_2O_4$. (Jonker, 1959) 29
3.2 Thermopower data of $Co_{3-X}Fe_XO_4$. (Jonker, 1959) 29
3.3 Activation energies (at T=450K) of the conductivity of mixed crystals $Co_{3-X}Fe_XO_4$. (Jonker, 1959) 29
3.4 Activation energies (ϵ) of $(MeFe_2O_4)_{1-y}(Fe_3O_4)$ versus y; the symbols are Δ: Ni; $\bigcirc$: Mn; and $\times$: Zn. (Miyata, 1961) 29
3.5 Thermopower for $Ni_{1-X}Fe_{2+X}O_4$ versus 1000/T; $\blacktriangledown$: X=0.046; o: X=0.076; $\times$: X=0.13; $\bullet$: X=0.21. (Griffiths et al, 1970) 30
3.6 Temperature dependence of $\sigma T/X$ for $Ni_{1-X}Fe_{2+X}O_4$; $\bullet$: X=0.21; $\times$: X=0.13; Δ: X=0.06; $\blacktriangledown$: X=0.046; $\triangledown$: X=0.03. (Griffiths et al, 1970) 30
3.7 $|G(\sigma T)|$ (see equation 5.5) for $Ni_XFe_{3-X}O_4$ plotted against temperature. (Whall et al, 1986) 31
3.8 Ln[G(σ)] versus Ln[T] for $Ni_XFe_{3-X}O_4$ for X$\geq$0.6. (Whall et al, 1986) . 31

3.9 T_G versus X. ▲: for low concentrations; ●: for higher concentrations. (Whall et al, 1986) 31

3.10 Ln[G(σ)] versus Ln[T] for $Ni_XFe_{3-X}O_4$ for X≤0.2: lines of slope 1. (Whall et al, 1986) 31

3.11 Thermopower of $Ni_XFe_{3-X}O_4$ versus temperature for X≤0.2. (Whall et al, 1986) 31

3.12 Thermopower of $Ni_XFe_{3-X}O_4$ versus temperature for X>0.2. (Whall et al, 1986) 31

3.13 Temperature dependence of the Seebeck coefficient of Mn ferrites. The symbols indicate the various contents. (Simsa et al, 1988) 35

3.14 Demonstration of Mott's law for Mn-ferrites. (Simsa et al, 1988) 35

3.15 The variation of the thermoelectric power versus temperature for manganese ferrite, according to Salerno (1986). 36

3.16 A plot of $G(\sigma T^{3/2})$ versus temperature for manganese ferrite. T_N is the Néel temperature. (Salerno, 1986) 36

3.17 Logarithm of the conductivity of $Fe_{3-X}Ti_XO_4$ versus 1000/T. The dashed lines indicate the linear part of the curves from which the activation energies E_σ have been calculated. (Kuipers, 1978) 37

3.18 The temperature dependence of the thermopower of the mixed series $Fe_{3-X}Ti_XO_4$. (Kuipers, 1978) 37

3.19 The magnetic transition temperature T_M of $Fe_{3-X}Ti_XO_4$ as a function of X. (Kuipers, 1978) 37

3.20 The composition dependence of the activation energies E_σ in $Fe_{3-X}Ti_XO_4$ determined from figure [3.17]. (Kuipers, 1978) 37

3.21 The low temperature data of figure [3.17] plotted versus $T^{-1/4}$. The dashed lines indicate the linear part of the curve. (Kuipers, 1978) 37

3.22 The transition temperature (T_C) from $T^{-1/4}$ law to T^{-1} law plotted versus X for $Fe_{3-X}Ti_XO_4$. (Kuipers, 1978) 37

3.23 Conductivity of $Fe_3O_{4-X}F_X$ versus 1000/T. The arrows indicate the Verwey temperatures of the samples X=0 and X=0.035. (Whall et al, 1977) 38

3.24 Seebeck coefficient of $Fe_3O_{4-X}F_X$ as a function of temperature. The Verwey temperature (T_V) and the Néel temperature (T_N) of the sample X=0 are indicated on the figure. (Whall et al, 1977) 38

3.25 Measurements of the thermopower of $Fe_3O_{4-X}F_X$ (at T=300K) compared against the predictions of the Heike's formula. (Jones, 1985) . 38

4.1 Diagram of the arc image furnace used in the floating zone technique. (Brabers, 1971) 42

4.2 The integral method for measuring the thermopower. T/S temperature sensor 45

4.3 The differential method for measuring the thermopower. Sample X has a temperature gradient dT along its length. T/S temperature sensor. 45

4.4 A typical plot of the ΔV versus ΔT at room temperature for magnetite. The relative seebeck coefficient can be found from the slope 45

4.5 A schematic diagram of a silicon diode used for measuring the temperature. (Igra et al, 1986) 45

4.6 A typical plot of the voltage (for $10\mu A$) versus temperature for a diode, shown in figure [4.5]. (ref. Southampton University — data sheet) 49

4.7 Schematic diagrams of one of the PTFE clamps used for anchoring a diode to the sample (S) 49

4.8 A schematic diagram showing the main details of the sample holder. P1 and P2 are the copper probes within the PTFE clamps 51
4.9 A schematic diagram of the thermal anchor used, indicating the thermal tempering rods and position of a small heater 52
4.10 A schematic diagram of the cryostat showing the electronic junction boxes, sample contraction compensator and sample holder 53
4.11 The electronics used by Keem (1975) for thermopower and resistivity measurements 54
4.12 The experimental configurations used by Keem (1975) for measuring the thermopower and resistivity 54
4.13 The electronics used by the present author for measuring the thermopower using the differential method 55
4.14 The electronics used by the present author for measuring the resistivity 55
4.15 A schematic diagram of the pin seal used. Designed by the present author so that driven shields could be used within the cryostat 56
4.16 A block diagram showing the major pieces of electronics used, which are interfaced to a Hewlett Packard computer for automation 56
4.17 A flow chart showing the main features of the software for automation. 57
4.18 A flow chart showing the main features of the software for automation. 58

5.1 A plot of G(σT) versus temperature for $Ni_XFe_{3-X}O_4$ with X$\leq$0.2. The Verwey transitions, T_V, are clearly shown; o: present author; ■: Yeung, (1982) 63
5.2 The G-factor of $Ni_XFe_{3-X}O_4$ versus temperature; X=0.8 — present author, X=0.9 — Yeung (1982) 63

5.3 The thermopower of magnetite versus temperature. ○: present author used silicon diodes as the temperature sensors, ×: Whall et al (1986) used thermocouples 63

5.4 Thermopower of pure Nickel metal versus temperature; ×: present author; ■: Blatt et al, (1967); ●: Grieg and Harrison, (1965) 63

5.5 $Ni_XFe_{3-X}O_4$ thermopower data plotted against temperature; ●: present author; ×: Whall et al, (1986); □: Griffiths et al, (1970) 63

5.6 Plot of $Log_{10}\sigma$ versus 100/Temp for $Zn_XFe_{3-X}O_4$ 64

5.7 Plot of $Log_{10}\sigma$ versus 100/Temp for $Zn_XFe_{3-X}O_4$ 64

5.8 Plot of $Log_{10}\sigma$ versus 100/Temp for $Mn_XFe_{3-X}O_4$ 64

5.9 Plot of $Log_{10}\sigma$ versus 100/Temp for $Mn_XFe_{3-X}O_4$ 64

5.10 The thermopower of $Zn_XFe_{3-X}O_4$ with $X \leq 0.1$ plotted against temperature 64

5.11 The thermopower of $Zn_XFe_{3-X}O_4$ with $X > 0.1$ plotted against temperature 64

5.12 The thermopower of $Mn_XFe_{3-X}O_4$ with $0 \leq X < 1$ plotted against temperature 64

5.13 $G(\sigma T)$ $[dLn(\sigma T)/d(1/T)]$ of $Zn_XFe_{3-X}O_4$ with $0 \leq X \leq 1$ plotted against temperature. Each plot has a shifted origin, which is indicated on the right hand side. The sharp rise on the $Zn_{0.8}Fe_{2.2}O_4$ plot is interpreted as being due to the onset of magnetic disorder at the Neel point, T_N ... 66

5.14 $G(\sigma T)$ $[dLn(\sigma T)/d(1/T)]$ of $Mn_XFe_{3-X}O_4$ with $0 \leq X < 1$ plotted against temperature. Each plot has a shifted origin, which is indicated on the right hand side 66

5.15 $G(\sigma T^{3/2})$ $[dLn(\sigma T^{3/2})/d(1/T)]$ of $Zn_XFe_{3-X}O_4$ with $0 \leq X \leq 1$ plotted against temperature. Each plot has a shifted origin, which is indicated on the right-hand side. The sharp rise on the $Zn_{0.8}Fe_{2.2}O_4$ plot is interpreted as being due to the onset of magnetic disorder at the Néel point, T_N 66

5.16 $G(\sigma T^{3/2})$ $[dLn(\sigma T^{3/2})/d(1/T)]$ of $Mn_XFe_{3-X}O_4$ with $0 \leq X < 1$ plotted against temperature. Each plot has a shifted origin, which is indicated on the right-hand side 66

5.17 Values of $G(\sigma T).k$ versus X for $Zn_XFe_{3-X}O_4$ at different temperatures; T=150K: o; T=290K: □; T_G: ▲. Gillot et al (1981) data at 290K: ×. . 69

5.18 Values of $G(\sigma T).k$ versus X for $Mn_XFe_{3-X}O_4$ at different temperatures; T=150K: o; T=290K: □; T_G: ▲ 69

5.19 The measured inductance of $Zn_{0.8}Fe_{2.2}O_4$ versus temperature. The temperature at which dI/dT is the largest is taken as the Neel temperature 69

5.20 A plot of $Ln|G(\sigma)|$ for $Zn_XFe_{3-X}O_4$ with $0 \leq X \leq 1$ versus temperature. The $T^{-1/4}$ law is indicated by the solid line 71

5.21 A plot of $Ln|G(\sigma)|$ for $Mn_XFe_{3-X}O_4$ with $0 \leq X < 1$ versus temperature. The $T^{-1/4}$ law is indicated by the solid line 71

5.22 $G(\sigma)$ versus temperature for $Zn_XFe_{3-X}O_4$ with $X \leq 0.1$. The solid lines have a slope$\sim$15 73

5.23 $G(\sigma)$ versus temperature for $Mn_XFe_{3-X}O_4$ with $X \leq 0.2$. The solid lines have a slope$\sim$15 73

5.24 Thermopower versus 1000/Temperature for $Zn_{0.8}Fe_{2.2}O_4$ 77

5.25 Thermopower versus 1000/Temperature for $Mn_{0.8}Fe_{2.2}O_4$ 77

5.26 A plot of eΠ versus the square of the temperature for $Zn_XFe_{3-X}O_4$ with $0 \leq X \leq 1$. The number of data points fitting the solid line falls for increasing X 78

5.27 A plot of eΠ versus the square of the temperature for $Mn_XFe_{3-X}O_4$ with $0 \leq X < 1$. The number of data points fitting the solid line falls for increasing X 78

5.28 The calculated half-bandwidths plotted versus X; ×: $Zn_XFe_{3-X}O_4$; o: $Mn_XFe_{3-X}O_4$. •: $\sqrt{AX(1-X)}$ — the expected half-bandwidth curve due to disorder on the A-sites 79

5.29 A plot of G(σT)-eΠ versus X at room temperature; o: $Mn_XFe_{3-X}O_4$; ×: $Zn_XFe_{3-X}O_4$ 80

5.30 A plot of G(σT)-eΠ versus X at T=200K; o: $Mn_XFe_{3-X}O_4$; ×: $Zn_XFe_{3-X}O_4$ 80

5.31 A plot of G(σT)-eΠ versus X at T=150K; o: $Mn_XFe_{3-X}O_4$; ×: $Zn_XFe_{3-X}O_4$ 80

5.32 Thermopower of $Zn_{0.8}Fe_{2.2}O_4$ versus temperature; o: measured; ×: calculated using equation (5.38) 82

5.33 Thermopower of $Mn_{0.8}Fe_{2.2}O_4$ versus temperature; o: measured; ×: calculated using equation (5.38) 82

List of Tables

		Page
4.1	Polynomial Coefficients	51
5.1	EPMA results and calculated values of X using Ln[(1–X)/2] — see section 5.6.1 — for $Zn_XFe_{3-X}O_4$	83
5.2	EPMA results and calculated values of X using Ln[(1–X)/2] — see section 5.6.1 — for $Mn_XFe_{3-X}O_4$	83
5.3	Zinc Ferrite	84
5.4	Manganese Ferrite	84
5.5	Zinc Ferrite	85
5.6	Manganese Ferrite	85

Chapter 1

INTRODUCTION

1.1 Spinel Ferrites

Spinel ferrites have been used successfully in the electronics industry for over forty years. Their usefulness stems from the ability to introduce a wide range of chemical species into the spinel lattice. By controlling the cation concentration in the general spinel formula $M_xFe_{3-x}O_4$ their electrical and magnetic properties can be tailored. Their applications are many and include microwave devices, information storage chips, inductors for filters and recording heads. Recently they have been introduced to silicon wafers to make an improved memory chip (Cole, (1989)). These applications use the spinel ferrite's magnetic properties. The current scientific interest in ferrites is mainly concerned with their electrical properties which share numerous features with other important electrical materials — for instance high T_C superconductors.

In 1939 Verwey studied magnetite (Fe_3O_4) and found that the conductivity changed by two orders of magnitude — a "metal–insulator" transition occurred at approximately 120K. Since Verwey many theoreticians and experimentalists have

studied not only magnetite but magnetite doped with different cations. Nevertheless, the conduction processes are still not fully understood.

1.2 Spinel Ferrite Crystalline Structure

The unit cell of spinel ferrite contains 32 oxygen ions (O^{2-}) in the form of a cubic close packed lattice (Verwey and Heilmann, (1947)). Amongst these oxygen ions are 64 tetrahedral and 32 octahedral interstices. Of these interstices only 8 tetrahedral and 16 octahedral are occupied. Shown in figure [1.1] is the arrangement of the atoms in a unit cell of a spinel showing the fourfold and sixfold coordination positions.

The general chemical equation is $[X]_A[Y_2]_BO_4$ where subscript A denotes a tetrahedral interstitial and B an octahedral interstitial. Magnetite has iron ions on both sublattices and the ionic formula is:

$$[Fe^{3+}]_A[Fe^{2+}Fe^{3+}]_BO_4^{2-} \tag{1.1}$$

As first pointed out by Verwey (1939) the conduction process may be thought of as the movement of an electron on the B sites which can be represented by the following chemical reaction:

$$Fe^{2+} + Fe^{3+} = Fe^{3+} + Fe^{2+} \tag{1.2}$$

This conduction process can be influenced by introducing impurities that replace some of the iron ions on either A or B sites. Thus, for example, zinc and manganese ferrous ferrites which are to be studied in the present work, have the ionic formula (see Chapter 3):

$$[M_X^{2+}Fe_{1-X}^{3+}]_A[Fe_{1-X}^{2+}Fe_{1+X}^{3+}]_BO_4^{2-} \tag{1.3}$$

where $0 \leq X \leq 1$ and M is either a zinc or manganese cation. The important features of these materials as far as conduction is concerned are:

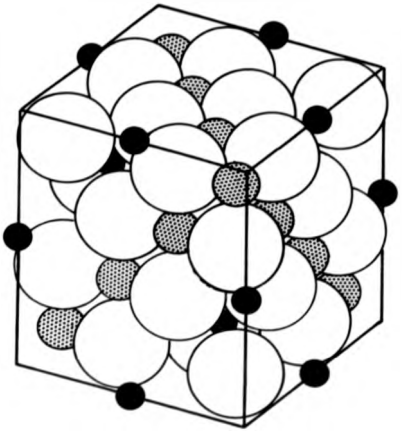

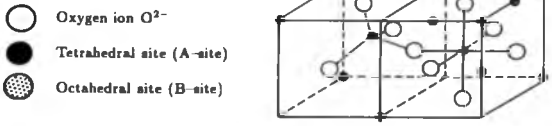

Figure 1.1: The arrangement of the atoms in a unit cell of a spinel ferrite, showing the fourfold and sixfold coordination positions (Verwey and Heilmann, (1947)).

(a) the substitutional disorder of the manganese and zinc ions on the A-sites should favour Anderson localization (Anderson, (1956)).

(b) the high electron concentration is conducive to electron correlation effects.

(c) the ionic nature of the materials favours localization by polaron formation (Holstein, (1959)).

(d) the ferrimagnetic ordering which will play a role in the conduction.

In the present work electrical conductivity and thermopower measurements down to 4.2K are described, the aim of which is an understanding of mechanisms (a), (b) and (c). Recent work by Barlow (1991) deals in some detail with item (d).

1.3 Layout of Thesis

Chapter 2 gives an up to date review of some of the relevant theories that have been developed since Verwey (1939) discovered the two orders of magnitude change in the conductivity of magnetite. Particular attention is paid the electrical conductivity and thermopower. Chapter 3 gives a survey of some previous work on ferrites including, for historical reasons, the work of Verwey (1939) and of Jonker (1959) and provides in its final section a justification for the present work. The present author has developed experimental techniques for the measurement of resistivity and thermopower, in order to make more accurate measurements on more resistive samples, and these are described in some detail in Chapter 4. Chapter 5 describes the results of such measurements and compares them with previous experimental work and with theories of hopping conduction.

Finally, in Chapter 6 a summary is given of the major achievements and

conclusions of this work.

Chapter 2

THEORIES OF CONDUCTION

2.1 Introduction

Verwey (1939) was the pioneer of investigations into the conduction processes in magnetite. He assumed conduction of d electrons on octahedral (B) sites as described by the following combined chemical and ionic equation:

$$[Fe^{3+}]_A[Fe^{2+} + Fe^{3+} = Fe^{3+} + Fe^{2+}]_B O_4^{2-} \tag{2.1}$$

Because magnetite is the parent material of ferrites an energy level diagram and the conduction processes as described by Camphausen, Coey and Chakraverty (1972) and Cullen and Callen (1970, 1971 and 1973) — sections 2.2.1 and 2.2.2 respectively — will be given.

Since the publication of Verwey's results on magnetite many studies have been carried out on both experimental and theoretical fronts. A general consensus is that the charge carrier in a ferrite material is to be treated as a localized particle. Conduction occurs when a localized particle hops from one site to another (Austin and Mott, (1969)). Some possible hopping processes within these samples will be considered in sections 2.2.5 and 2.2.6, with particular reference to

the Miller–Abrahams (1960) paper on single–phonon assisted hopping conduction between localized sites (section 2.2.4) and developments thereof.

The Miller Abrahams theory is for single electron hops from one site to another and not influenced by other electrons. When electrons become close to each other, owing to a high concentration of localized carriers, an electron will be influenced by neighbouring electrons. Therefore, in section 2.3 many electron conduction is reviewed which starts with correlation effects giving a Coulomb Gap for one–electron hops and then concludes with the types of many–electron hopping possible.

When an electron is surrounded by positive and negative ions a lattice distortion is possible (section 2.4). Section 2.4.3 describes in more detail this lattice distortion termed a "polaron" and section 2.4.4 briefly comments on polaron conduction.

2.2 Single–Electron Conduction Models

2.2.1 Camphausen, Coey and Chakraverty Model

In 1972 Camphausen, Coey and Chakraverty constructed a one electron energy diagram for Fe_3O_4 based on data from soft x ray, cathodoluminescence and optical absorption measurements. The result is shown in figure [2.1]. Two parameters determine the main features:

I) Crystal field splitting (Δ_{c-f}) – deduced from optical data, and

II) Hund's rule – exchange splitting between spin–up and spin–down orbitals on the same cation.

The electron arrangement for Fe is $(Ar)3d^64s^2$ and the two ions Fe^{3+} and Fe^{2+} are $(Ar)3d^5$ and $(Ar)3d^6$ respectively. All these d–electrons lie in a gap between

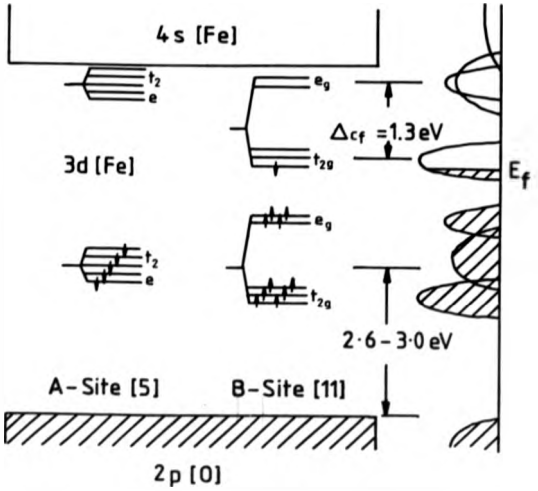

Figure 2:1 Single-electron energy diagram for Fe_3O_4 according to the Camphausen, Coey and Chakraverty model (1972).

the filled 2p(O) and empty 4s(Fe) states: five spin–down electrons reside on the tetrahedral (A) sites and ten spin–up plus one spin–down electrons on the octahedral (B) sites.

This one–electron energy diagram shows that a solitary electron is possibly the reason for metallic like conduction, but more information is required to examine the electrical characteristics of Fe_3O_4 at low temperatures.

2.2.2 Cullen and Callen

Cullen and Callen in a series of papers (1970, 1971, 1973) consider a band model based on an energy level scheme similar to that of Camphausen et al for magnetite. They suggest that a half filled band causes "metallic" behaviour above T_V, due to a finite overlap of electronic wavefunctions. While below T_V, inter–atomic coulomb repulsion splits this band giving a Verwey transition. This approach might work for a regular array of constant potential wells like that of Fe_3O_4, but does not explain what would happen when disorder is introduced i.e. by the addition of nickel or zinc or manganese.

2.2.3 Anderson localization

Anderson (1958) was the first person to consider conduction within a disordered system using a quantum–mechanical theory to describe localization. Consider the periodic lattices shown in figures [2.2–2.3]. If the potential wells are far apart such that only the nearest neighbour interactions can occur and then they are gradually brought closer together increasing the overlap of the wavefunctions then a conduction band forms of energy width:

$$E_B = 2.z.I \tag{2.2}$$

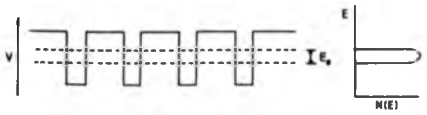

Figure 2:2 A periodic lattice without disorder (Mott and Davis (1979)).

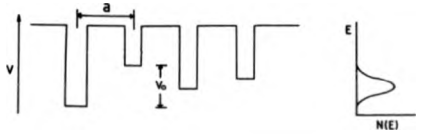

Figure 2:3 A periodic lattice with vertical disorder (Mott and Davis (1979)).

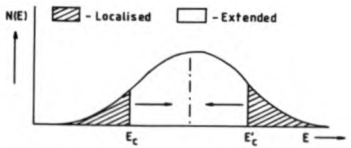

Figure 2:4 A Gaussian density of states with a mobility edge showing the localised and extended states (Mott and Davis (1979)).

where z is the coordination number and I the overlap integral number. This is known as the tight-binding approximation.

Anderson then considered what would happen when disorder is introduced. He pointed out that when V_0/E_B was greater than a certain value depending upon z then there would be no diffusion at T=0. This condition has been studied by Edwards and Thouless (1972) who have calculated $V_0/E_B \approx 2$ for z=6.

Mott (1966, 1967) took this further and pointed out that when the disorder is large (as in figure [2.3]) and the Anderson criterion not satisfied then there exists a certain energy E_C such that when $E<E_C$ there is no diffusion. Hence at T=0,

$$< \sigma_E > \begin{cases} = 0 & E < E_C \\ \neq 0 & E > E_C \end{cases} \tag{2.3}$$

E_C is referred to as the "mobility edge". If the Fermi level can be swept in some way through E_C, from extended to localized states or vice-versa, a metal-insulator transition occurs (see figure [2.4]).

2.2.4 Hopping conduction between localized states (Miller-Abrahams)

Miller-Abrahams (1960) consider two sites i and j separated by a large distance in a disordered lattice and assume that an electron will have energy and wavefunction ε_i, ϕ_i respectively when occupying site i and ε_j, ϕ_j when occupying site j. By analogy with the hydrogen molecular ion it is expected that when the sites are brought closer together the resulting possible wavefunctions will be linear combinations of ϕ_i and ϕ_j:-

$$\Psi = C_j\phi_j \pm C_i\phi_i \tag{2.4}$$

The resulting wavefunctions are found to be:

$$\Psi_a = \phi_i + (I/\Delta)\phi_j \quad \text{and} \quad \Psi_b = \phi_j - (I/\Delta)\phi_i \tag{2.5}$$

where $\Delta = \varepsilon_j - \varepsilon_i$, $\varepsilon_j > \varepsilon_i$ and

$$I = \mathrm{EXP}[-r_{ij}/a].e^2/\kappa r_{ij} \tag{2.6}$$

for 1s states, where "a" is the Bohr radius. The states a and b are illustrated in figure [2.5]. The electron–phonon interaction H_{ep} may be thought of as changing the relative potential energies of the two wells, leading to the possibility of states a and b of total energy:-

$$E_n^l = c_l + (n_q + 1/2).\hbar\omega_q, \quad \ldots\ldots \quad l = a, b \tag{2.7}$$

where the second term is the vibrational energy. Transitions occur according to the Fermi's golden rule for the transition probability:-

$$\omega_{ab}(n, n') = \frac{2\pi}{\hbar^2} < b, n' \mid H_{ep} \mid a, n >^2 .\delta(E_b n' - E_a n) \tag{2.8}$$

This formula expresses a law of energy conservation according to which a change in the electron energy must be balanced by the absorption of one or more phonons.

Miller–Abrahams (1960) assume:-

$$\hbar\omega_q = \varepsilon_b - \varepsilon_a \tag{2.9}$$

i.e. the absorption of a single phonon. Evaluating equation (2.8) and summing over all combinations n, n' they obtain a total intrinsic transition probability:-

$$\omega_{ij} = \omega_0.\mathrm{EXP}[-2r_{ij}/a].n_q \tag{2.10}$$

With

$$n_q \approx \mathrm{EXP}[-\hbar\omega_q/kT] \tag{2.11}$$

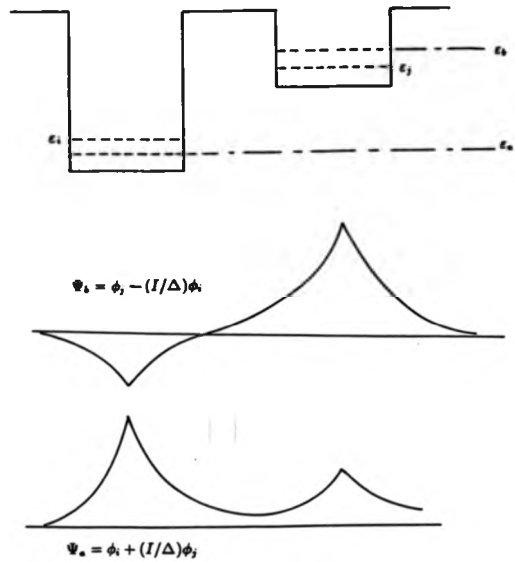

Figure 2:5 Two potential wells and their resulting wavefunction states Ψ_a and Ψ_b.

from equation (2.9) and with $\varepsilon_j \cong \varepsilon_b$, $\varepsilon_i \cong \varepsilon_a$ we get:-

$$\omega_{ij} = \omega_0.\mathrm{EXP}[-(\varepsilon_j - \varepsilon_i)/kT].\mathrm{EXP}[-2r_{ij}/a] \tag{2.12}$$

Equation (2.12), together with figure [2.5] may be thought of describing a process in which a phonon gives an electron on site i just sufficient energy for it to tunnel to site j, ω_{ij} being proportional to the number of phonons (equation (2.10)) and a tunnelling factor $\mathrm{EXP}[-2r_{ij}/a]$. Finally, taking account of the occupancies of sites i and j the average transition rate is:-

$$\Gamma_{ij} = f_i(1 - f_j).\omega_{ij} \tag{2.13}$$

and assuming all energies measured with respect to ε_f and greater than kT:-

$$\Gamma_{ij} \approx \Gamma_0.\mathrm{EXP}[-2\alpha R_{ij}].\mathrm{EXP}\left[-\left[\frac{|\varepsilon_i| + |\varepsilon_j| + |\varepsilon_i - \varepsilon_j|}{2kT}\right]\right] \tag{2.14}$$

2.2.5 Variable Range Hopping

The two site conductance corresponding to equation (2.14) is (Ambegaokar et al, (1971)):-

$$G_{ij} = (e^2/kT).\Gamma_{ij} \tag{2.15}$$

which has been obtained by assuming that the site energy difference in the presence of a field is:-

$$\varepsilon_j - \varepsilon_i + eF.\hat{r}_{ij} \tag{2.16}$$

The solid is now usefully considered as a network of conductances G_{ij}. Mott (1968) in an early calculation produced a simple estimate of the overall conductivity of this network by assuming that the electrons flowed through links of maximum conductance. Taking the density of electron states equal to a constant, Mott constructed a sphere of radius r_{ij} around site i. In order for an electron to hop to a site of

energy ε_j within this sphere the number of sites in the energy range $(\varepsilon_j - \varepsilon_i)$ within the volume should be:-

$$4/3.\pi R^3.(\varepsilon_j - \varepsilon_i).N(E) \geq 1 \tag{2.17}$$

Taking ε_i=0, ε_j >0 (i.e. two sites of energy greater than ε_f):-

$$G_{ij} = G_0.\mathrm{EXP}[-2\alpha R].\mathrm{EXP}[-\varepsilon_j/kT] \tag{2.18}$$

and substituting for ε_j from equation (2.17) and maximizing Mott obtained:

$$R = [9/(8\pi\alpha N(E)kT)]^{1/4} \tag{2.19}$$

with N(E)=N_0 giving finally:

$$\sigma = \sigma_0.\mathrm{EXP}[-(T_0/T)^{1/4}] \tag{2.20}$$

with

$$T_0 = 1.55.\left[\frac{\alpha^3}{kN_0}\right] \tag{2.21}$$

More rigorous derivations of equation (2.20) followed, including that of percolation theory. Taking advantage of the exponential dependence of G on R a network of conductances is built up starting with the highest G (refer to figure [2.6]). The last conductance added to form a complete link between contacts A and B is called the critical conductance G_c. Since G_c is exponentially smaller than any other conductance in the chain the overall conductance of the chain is approximately equal to G_c. Now, when further conductances are added to form parallel chains, these later chains are effectively shorted out by the first. Therefore the overall conductance of the network is G~G_c. Proceeding in this way Pollak (1978) and Ambegaokar et al (1971) obtain equation (2.19). We may write:

$$\sigma = \sigma_0.\mathrm{EXP}[-W/kT] \tag{2.22}$$

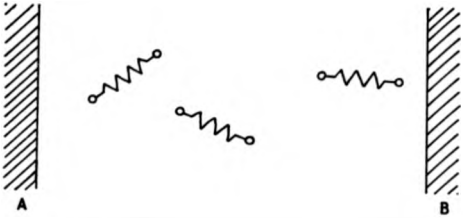

Figure 2:6 A diagram showing three possible high conductance links within a solid.

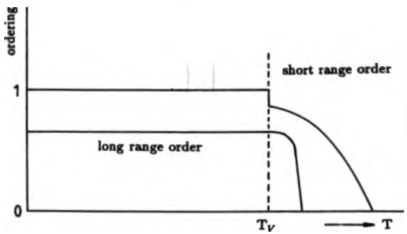

Figure 2:7 Qualitative behaviour of the short range and long range ordering about the Verwey temperature T_V.

with

$$W = kT_0^{1/4}.T^{3/4} \tag{2.23}$$

It follows from the percolation argument that states of energies $|\epsilon_i|$>W are disconnected from the critical network i.e. there is an energy layer of width 2W centred around E_f which gives rise to conduction.

The pre–exponential factor has been calculated by Kirkpatrick (1974) to be $\sigma_0 \propto (B/T)^{-.35}$.

The above result (equation (2.20)) is derived on the assumption of a constant density of states. Pollak (1978) using, a density of states proportional to E^n obtained:–

$$\mathrm{Ln}(\sigma) = 1/T^{(n+1)/(n+4)} \tag{2.24}$$

Mott's $T^{-1/4}$ law is achieved if n=0 i.e. a constant density of states. If $n \rightarrow \infty$ then T^{-1} results i.e activated hopping conduction. Movaghar and Schirmacher (1981) have used a density of states which has an exponential band tail but which is constant towards the middle of the band and place the Fermi level in the middle of the band tail. For low temperatures they obtain a $T^{-1/4}$ dependence. Vescan et al (1972) obtained the same result when considering a linear tail in the density of states instead of an exponential tail.

We note that a $T^{-1/4}$ law is associated with a constant density of states in the "conduction layer" and therefore it is clear that the law should always be obtained at the lowest temperatures, providing that N(E) is finite at E_f.

Analysing many authors data Hill (1976) concluded that the $T^{-1/4}$ law presumed by most of the original authors had been observed. However, a $T^{-1/4}$ law is not necessarily the consequence of variable–range hopping: Emin (1974) has noted that a similar behaviour is a consequence of multiphonon hopping transitions.

A $T^{-1/2}$ law for the conductivity has also been observed by Mobius (1983)

on amorphous $Si_{1-X}Cr_X$ films. On this occasion the conductivity may be influenced by the Mobility edge (see section 2.2.3) because the T_0 values — as defined by equation (2.20) — are in the range between 5×10^4K and 5×10^{-3}K, suggesting that the localisation radius α^{-1} varies considerably.

The Peltier heat for hopping within an energy layer defined by equation (2.23) has been calculated by Zvyagin (1973):-

$$\epsilon\Pi = \frac{\int_{E_f-W}^{E_f+W} N(E).(E-E_f).dE}{\int_{E_f-W}^{E_f+W} N(E).dE} \tag{2.25}$$

where the conducting layer is of width $E_f+W \geq E \geq E_f-W$. Expanding about E_f for small enough W and using $S=\Pi/T$ numerous authors (Zvyagin (1973), Kosarev (1975), Overhof (1975)) obtain:-

$$S \approx \frac{W^2}{3eT}\left\{\frac{d\mathrm{Ln}[N(E)]}{dE}\right\}_{E=E_f} \tag{2.26}$$

and from equation (2.23):-

$$S \propto T^{1/2} \tag{2.27}$$

2.2.6 Nearest Neighbour Hopping

Equation (2.19) shows that R falls as T increases — hence the name variable-range hopping. This continues until R reaches its minimum value corresponding to hops between nearest neighbours. Then, from equation (2.17):-

$$W = \varepsilon_j = 1/(4/3.\pi a^3.N_0) \tag{2.28}$$

and

$$N = \int_0^B N_0.dE \tag{2.29}$$

where B is the width of the Anderson band (i.e. energy distribution of states) and N the number of hopping sites/unit volume. Therefore, with $N \sim 1/a^3$ then $W \sim B$. This is intuitively obvious since $W \propto T^{3/4}$ we must have $W_{Max} \sim B$ corresponding to a situation in which all states in the band contribute to conduction. Referring to equation (2.18), we note that a transition from variable-range hopping (VRH) to nearest-neighbour hopping (NNH) corresponds to a transition from a situation in which hopping routes are determined by ε_j and therefore the carrier will hop long distances (equation (2.17)) so as to minimize ε_j (VRH) to a high temperature situation (NNH) where a minimum in G is obtained by minimizing R (NNH), ε_j/kT being small. The temperature at which this transition occurs (Pollak and Knotek, (1979)) is of approximate magnitude:-

$$T \simeq 3.3W/(\alpha a k) \tag{2.30}$$

The thermopower for NNH may be obtained from equation (2.25) by integrating between limits 0 and B (Zvyagin, (1973)) giving:-

$$S \propto 1/T \tag{2.31}$$

for a constant density of states. Movaghar and Schirmacher (1981) obtained the same result using an "Effective Medium Approximation" (EMA) on a density of states having exponential tails at the band edges to approximate to a Gaussian. At almost the same time Whall (1981) using EMA to calculate the Peltier heat on a constant density of states found that $e\Pi=0$ when the Fermi level is in the middle of the band. Therefore, he added a slope to the density of states such that it increased with increasing energy i.e. N(E) = A + BE, and obtained for $E_f \sim B/2$:-

$$e\Pi = \frac{5}{6}.\left[\frac{W(0)^2}{2} + \frac{2\pi^2}{3}.(kT^2)\right].\frac{d\mathrm{Ln}[N(E)]}{dE} \tag{2.32}$$

where W(0) is the (nearest neighbour) conductivity activation energy extrapolated to T=0. If W(0)=0 equation (2.32) then reduces to the metallic form (Mott and Jones, (1936)). For a wide range of Fermi energies Whall calculated the thermopower to be:-

$$S = A/T + B.T \tag{2.33}$$

2.3 Many–Electron Effects

2.3.1 Introduction

The previous sections have dealt with single electron hopping mechanisms which neglect the electron–electron interactions. A Coulomb term may be necessary when there are many electrons in close proximity to each other. Such an interaction is believed to cause the "metal–insulator" transition at the Verwey temperature in magnetite where long range order is lost. Lorenz and Ihle ((1975), Ihle and Lorenz (1973, 1974 and 1980)) have produced what is perhaps the most promising theoretical description of the interaction effects leading to the Verwey transition in Fe_3O_4. Pollak and Knotek (1979) first pointed out that electron–electron interactions should be important in the impurity conduction. Numerous papers have been published by Pollak and other authors, most notably Efros and Shklovskii (1984), on this problem. Mott (1979) first applied these ideas to $Fe_3O_{4-X}F_X$.

Lorenz and Ihle (see section 2.3.2) consider the Coulomb interactions between nearest neighbours and next nearest neighbour for pure magnetite — the Verwey transition is associated in their model with a complicated interplay between short range order and long range order.

Many electron correlation effects in impurity state hopping conduction materials have been shown theoretically to produce a Coulomb Gap in the density of

states. Efros and Shklovskii (1975) have shown that, near E_f, the density of states to be $N(E) \propto |E - E_f|^2$, and find a conductivity with a $T^{-1/2}$ law. While Mott (1975, 1979) agrees with Pollak and Knotek that N(E) is finite in the Gap giving a conductivity with a $T^{-1/4}$ law at low enough temperatures. Section 2.3.3 gives a description of the nature of the Coulomb Gap. In section 2.3.4 the properties in the vicinity of the Coulomb Gap are described. Section 2.3.5 gives details on how the Coulomb Gap can be alleviated by different types of many electron hopping.

Firstly, electron electron interactions in magnetite are considered.

2.3.2 The model of Lorenz and Ihle for Fe_3O_4

Cullen and Callen (1970, 1971 and 1973) described magnetite as having a half filled band with inter atomic Coulomb repulsion splitting the band to give a Verwey transition. Lorenz and Ihle take an alternative approach in which crystal field splitting gives $U_1 \gg I > U_2$, where U_1 is the nearest neighbour Coulomb interaction energy, U_2 is the Coulomb energy due to the next nearest neighbours and I is the overlap integral (see equation 2.2). At the highest temperatures there is complete disorder and the density of states approximates to a set of delta functions at 0, U_1, $2U_1$, $3U_1$, $4U_1$, $5U_1$ and $6U_1$, with $E_f = 3U_1$. Lorenz and Ihle consider that conduction is due to tunnelling between nearest neighbour sites of the same Coulomb energy. Whall et al (1977) have pointed out that this state of affairs is similar to that suggested by Mott (1974) in which the electron sees an Anderson localization potential due to other electrons, but in which hopping between sites of different energies occurs. As the temperature is lowered there is a gradual increase in short range order as shown in figure [2.7], lowering the density of states at $3U_1$ — figure [2.8]. Next nearest neighbour interactions are responsible for the development of long range order, which is complete at T_V. The interplay of long range ordering

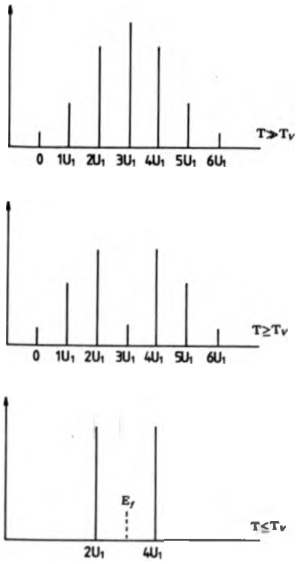

Figure 2:8 The influence of temperature on the nearest neighbour interactions for magnetite (Lorenz and Ihle (1975)).

and short range ordering leads to an abrupt further increase of short range order at T_V (figure [2.7]), completing the short range order process and giving the sharp two orders of magnitude decrease in conductivity at T_V. The major accomplishment of this model is that it gives suitably low values of T_V - because T_V is determined by long range ordering associated with $U_2 \ll U_1$.

Lorenz and Ihle calculate $kT=0.09U_1$ and $U_1/U_2=0.04$, yielding the values $U_1=0.11eV$ and $U_2=0.004eV$ for $T_V \sim 120K$. They further show that the conductivity activation energies near T_V are $\varepsilon_A(T \leq T_V)=U_1=0.11eV$ and $\varepsilon_A(T>T_V)=U_1/2=0.055eV$, in good agreement with Adler (1968). Also, they show that a considerable amount of SRO exists above T_V.

2.3.3 The Coulomb Gap

When impurities are introduced into Fe_3O_4 the static ionic disorder introduced (of Zn^{2+}, Mn^{2+}, Ni^{2+}, F^-, etc) might be expected to broaden the levels $2U_1$ and $4U_1$ as shown in figure [2.9] leaving a Coulomb Gap. Here the disorder might be thought of as perturbing the electron-electron interaction effects. This situation has not been dealt with by theorists. However, it is expected that the converse situation i.e. impurity conduction perturbed by electron-electron interactions will serve as an excellent guide. Remembering that in Fe_3O_4 the electrons order as a result of their mutual coulomb repulsion, we follow Pollak and consider what happens when we add electrons to a disordered medium. First consider impurity conduction. The first electrons to go into the disordered medium will enter sites which minimize their Coulomb energy associated with the presence of a random distribution of static ions. This will continue until there is a sufficient density of electrons for inter-electronic interactions to be important. There will thus be a group of electrons which are randomly distributed and of low potential energy and a second group which have

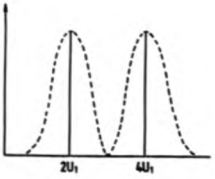

Figure 2:9 A density of states with a Coulomb Gap showing possible peak broadening due to impurities according to Lorens and Ihle (1975).

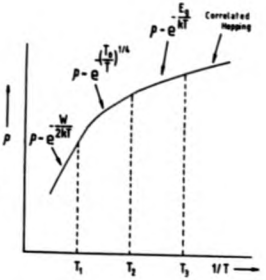

Figure 2:11 A graph of resistivity against reciprocal temperature showing three temperature regions as defined by Pollak and Knotek (1979)

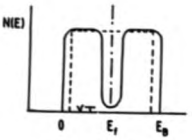

Figure 2:10 A density of states with a Coulomb Gap according to Pollak and Knotek (1979). They predict that υ is small but finite whilst Efros and Shklovskii (1975) predicts υ=0.

a tendency to order, situated around E_f. This second group can be modeled by a periodic electronic "lattice". If an electron moves into a "wrong" site on this lattice, it costs an energy ε_G, the Coulomb Gap energy. Various authors have calculated ε_G (Efros (1976), Srinivasan (1971), Pollak and Knotek (1979)). The most useful expression for our purpose (Pollak and Knotek) is:

$$\varepsilon_G \approx E_C[E_C/(E_C + \Delta)]^{1/2} \tag{2.34}$$

where Δ is the disorder energy and $E_C = e^2/\kappa a$ the Coulomb repulsion between carriers separated by an average distance a, where κ is the dielectric constant. Pollak and Knotek (1979) predicts that the density of states in the vicinity of E_f varies as:

$$N(E) = \upsilon + A(E - E_f)^2 \tag{2.35}$$

Efros and Shklovskii (1975) predicted that the density of states will vanish at E_f i.e. υ=0, see figure [2.10].

2.3.4 Transport Properties in the Vicinity of the Coulomb Gap

Pollak and Knotek (1979) define three temperature regions for the low temperature d.c. conductivity (see figure [2.11]). At the highest temperatures, nearest neighbour hopping occurs, but is replaced by variable range hopping at intermediate temperatures having a $T^{-1/4}$ behaviour. At even lower temperatures the electrons must be activated across the Coulomb Gap. The authors give for the dividing temperatures:

$$kT_1 \approx 3.3W/\alpha a \quad \text{and} \quad kT_2 \sim 2E_G/\alpha a \tag{2.36}$$

where $1/\alpha$ is the radius of the localized state. T_1 separates variable range hopping from nearest neighbour hopping and T_2 divides the activation across the Gap and variable range hopping regimes.

The behaviour at the lowest temperatures is controversial. Using the fact that at the Fermi level for single–electron hops the density of states is $N(E)=(E-E_f)^2$ and applying Mott's conductivity maximization procedure, Efros and Shklovskii (1975) show that the conductivity in this temperature regime is (c.f. equation (2.24)):-

$$\sigma(T) \propto \text{EXP}[-(T_0/T)^{1/2}], \qquad T_0 = \beta e^3/\kappa a \tag{2.37}$$

where e is the electronic charge, κ is the dielectric constant and β is a numerical coefficient.

For conduction in states outside the Coulomb Gap, where the density of states is constant, these authors agree with Mott that the conductivity obeys a $T^{-1/4}$ law.

However, Pollak and Knotek (1979) and also Mott (1976) believe that correlated multi–electron hopping will dominate over single–electron hopping and this will be dealt with in the next section.

2.3.5 Multi– / Many–Electron Hopping

Mott (1976), Pollak (1980) and Pollak and Knotek (1979) have analysed the lowest temperature regime where multi–electron hopping is thought to occur. They obtain similar results although taking different approaches. The two techniques are as follow:-

Many–Electron Hopping according to Mott

Mott considers electron–electron interactions in the following way. An electron at a site A will create an electronic polaron in which neighbouring electrons are displaced because of Coulomb repulsion, see figure [2.12]. A Coulomb Gap will exist if when the electron hops from site A to B the neighbouring electrons at site B remain fixed in space. Processes in which the Coulomb Gap is suppressed will involve short range hops of electrons at site B i.e. the electron takes its polaron

with it. If short hops occur they occur with a probability proportional to T^S, where $S=3\alpha r_0/2Ln2$ and r_0 is the hopping distance. The long hops are of the normal variable-range hopping type with,

$$\sigma = A'.T^S \mathrm{EXP}[-B/T^{1/4}] \tag{2.38}$$

and S~10.

Efros (1976) has also considered polaron like hopping for low temperatures but obtains different results. Efros obtains:

$$\sigma \propto \mathrm{EXP}[-(T_0/T)^n] \tag{2.39}$$

with n=1/2.

Many-Electron Hopping according to Pollak and Knotek

Pollak and Knotek (1979) consider a collective hopping configuration, see figure [2.13]. Four sites are shown where the first and third sites are occupied while the other two are empty. The electron on site 1 must overcome a certain amount of Coulomb repulsion if it wants to hop to site 2. This Coulomb repulsion can be reduced if the electron on site 3 simultaneously hops to site 4. This is called correlated multi-electron hopping. To find which process is the most probable at a given temperature one needs to compare the Miller-Abrahams impedances for one and two electron hops. The essential factors for the one-electron and two-electron transitions are respectively:

$$\mathrm{EXP}[2R/a].\mathrm{EXP}[\varepsilon/kT] \tag{2.40}$$

and

$$\mathrm{EXP}[2R/a].\mathrm{EXP}[2R'/a].\mathrm{EXP}[\varepsilon/kT].\mathrm{EXP}[-\Delta/kT] \tag{2.41}$$

Figure 2:12 Polaron–like multi–electron hopping conduction according to Mott (1976).

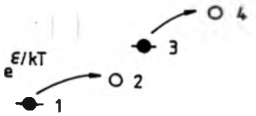

Figure 2:13 Correlated multi–electron hopping, according to Pollak and Knotek (1979).

where ε is the energy difference between initial and final states for the one–electron hop and Δ is the energy reduction when the second electron hops from site 3 to site 4. The process having the smallest impedance will the one that dominates the conduction. The transition from a one–electron to a two–electron process will occur when:–

$$\mathrm{EXP}[2R'/a].\mathrm{EXP}[-\Delta/kT] = 1 \tag{2.42}$$

If the following approximations are made:–

$$\Delta = e^2/\kappa r_C,$$

where

$$R' = r_C = (4\pi/3)^{-1/3}.N^{-1/3} \tag{2.43}$$

and N is the density of carriers, then the transition temperature between single and multi–electron hopping is:–

$$kT_3 \approx \frac{e^2 a}{\kappa}.\left[\frac{4\pi N}{3}\right]^{1/3} \tag{2.44}$$

Although this derivation has used relatively crude approximations it agrees very well with a more accurate derivation (Knotek and Pollak, (1971)).

For n–electron transitions at very low temperatures Pollak writes:–

$$\sigma(T) \;\; \propto \;\; \mathrm{EXP}[-2\Sigma r_{ij}/a].\mathrm{EXP}[-E/kT] \tag{2.45}$$

where E is the n–electron transition excitation energy and Σr_{ij} the sum of all hopping distances involved in the cascade process. Letting the average hopping distance of n electrons be <r>, the first term of equation (2.45) becomes EXP[–2n<r>/a]. Pollak then calculates the average excitation energy for an n–electron excitation to be:–

$$E \sim n^2 \varepsilon_C / d^n \tag{2.46}$$

where d is the average number of directions in which the electron can hop and ε_C is a typical "Coulomb energy". Using this information and Mott's maximization

procedure Pollak calculates the optimum conductivity to be:

$$\sigma(T) \propto T^{(2/Lnd)<r>/s} \tag{2.47}$$

This is only valid for large n. Equation (2.47) approximates to that obtained by Mott (see equation (2.38)) over a certain temperature range i.e. $\sigma(T) \propto T^{S}$ where $s \gg 1$, but is based on a different many–electron hopping process. Pollak has given, for this conduction process, the label "cascade–like multi–electron hopping" whilst Fleishman et al (1978) labeled it "variable number hopping".

2.4 Small "Dielectric" Polarons

2.4.1 Introduction

An electron moving through a periodic lattice with a low mobility ($<1 cm^2V^{-1}s^{-1}$) may be influenced by the positive (and negative) centres at the sites. See figure [2.14]. If the electron is slow, as compared with the movement of the positive ions, then the positive centres become attracted to the electron (and the negative centres repelled) causing a distortion in the lattice and inducing a potential well. If the electron is very slow then the electron becomes self trapped; this polarised cloud plus electron is termed a "dielectric polaron". The electron can only move, when the potential well is deep, if it effectively takes the polaron cloud with it. ("Dielectric polarons" are different to "electronic polarons" – see figure [2.12]).

Polarons have been seen in a number of different materials; single crystal As_4S_4 (Street and Gill, (1966)), orthorhombic sulphur crystals (Gibbons and Spear, (1966)) and Li doped MnO (Crevecoeur and Wit, (1970)). All these authors obtain electron mobilities of order $10^{-2} cm^2V^{-1}s^{-1}$ at room temperature and above. Perhaps the most interesting of the samples mentioned is MnO, because it is the d–electrons

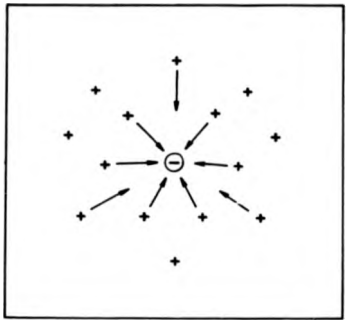

Figure 2:14 An electron causing lattice deformation: the polarised cloud plus the electron is called a "dielectric" polaron.

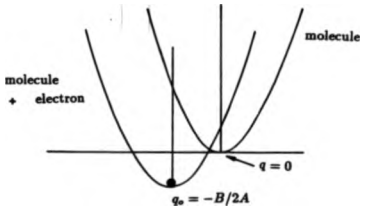

Figure 2:15 The displacement of a molecule's energy when an electron is added. (Austin and Mott, 1969)

on the manganese ions which are the current carriers as in the manganese and zinc ferrites measured in this investigation. More recently polaron hopping has been inferred in ferrites (Yeung, (1982) Because the polaron concept is applicable to ferrites it is worth discussing some of its main features.

2.4.2 Polaron Size and its Binding Energy

There are two sizes of polaron, the size depending upon the magnitude of lattice deformation. When the lattice around an electron is only affected slightly such that the electron is loosely bound then this is termed a "large" polaron i.e. the effective radius (r_P) of the polaron is greater than the lattice constant. Since this type of polaron is less relevant to ferrites then it shall not be considered any further. When the lattice is greatly deformed the electron becomes trapped inside a deep potential well and hence is tightly bound; this is termed a "small" polaron i.e. r_P less than the lattice constant.

Austin and Mott (1969) have shown for small polarons r_P to be:-

$$r_P = \frac{<a>}{2}\left[\frac{\pi}{6}\right]^{1/3} \tag{2.48}$$

where <a> is the mean intersite separation. These authors also show that the polaron binding energy is:-

$$W_P = e^2/2\kappa_P r_P \tag{2.49}$$

with $1/\kappa_P = 1/\kappa(\infty) - 1/\kappa$, where κ and $\kappa(\infty)$ are the dielectric constants with and without the electron respectively.

2.4.3 Polaron Hopping Motion

Austin and Mott (1969) review the molecular crystal model of Holstein (1959). A solid is assumed to consist of diatomic molecules having vibrational energies Aq^2

without an electron, where q is a configurational constant. When an electron is added to a molecular site the energy is modified to Aq^2-Bq, where $-Bq$ is the energy of the electron (see figure [2.15]). The polaron binding energy W_P (i.e. minimum energy) is then:-

$$W_P = B^2/4A \tag{2.50}$$

with equilibrium coordinate,

$$q_0 = B/2A \tag{2.51}$$

The result corresponds to a situation in which the tunnelling probability is small, i.e. $I \to 0$ where I is defined by equation (2.2), and is known as non adiabatic hopping. In the case where the electron can move backwards and forwards several times during each excitation of the lattice the work required to achieve the approximate lattice configuration is offset by a reduction in the kinetic energy and

$$W_H = W_P/2 - I \tag{2.52}$$

This is known as adiabatic hopping. For an electron to jump from one molecule to another, the configurational parameters q_1, q_2 must be such that the electron's energy is the same in either molecule: thus

$$Bq_1 = Bq_2 \tag{2.53}$$

The energies required to distort molecules 1 and 2 to configurations in which $q_1=q_2=q$ are:

$$A(q_0 - q)^2 \quad \text{and} \quad Aq^2,$$

which add up to a total energy W_H given by:

$$W_H = A(q_0^2 - 2q_0q + 2q^2). \tag{2.54}$$

This is a minimum when:-

$$q = q_0/2 \tag{2.55}$$

Substituting (2.55) into (2.54) the activation energy for hopping is thus:

$$W_H = W_P/2 \tag{2.56}$$

and the conductivity is proportional to EXP[W_H/kT].

At high temperatures W_H is temperature independent. At low temperatures an intersite hop can involve the absorption and emission of large numbers of phonons ("multi phonon assisted hopping"). The numbers emitted and absorbed must be roughly equal to conserve energy. Since the average number of phonons of a particular wavevector is:

$$N_q = \frac{1}{EXP(\hbar\omega_q/kT) - 1} \tag{2.57}$$

processes involving a large number (N_q) of phonons freeze out for kT<$\hbar\omega_q$ (Emin, (1974)). For optical phonons the jump rate tends to EXP($\hbar\omega_0$/kT) for T<$\hbar\omega_0$/3k, corresponding to the emission of a phonon and absorption of another phonon of energy $\hbar\omega_0$. For acoustic phonons Emin finds that the jump rate is rather similar to a $T^{-1/4}$ law.

2.4.4 Polaron Hopping in a Disordered Lattice — Conductivity and Thermopower

Böttger and Bryksin (1977a d) have investigated nearest neighbour hopping in a disordered medium for strong electron phonon coupling. They find the two site conductance:

$$G_{ij} \propto \frac{f_i(1-f_j)}{(kT)^{3/2}} \mathrm{EXP}\left[-\left\{2\alpha N^{-1/3} + \frac{W_H}{kT}\right\}\right] EXP\left[\frac{(\varepsilon_i - \varepsilon_j)}{2kT}\right] \tag{2.58}$$

where N is the concentration of sites, α is the reciprocal Bohr radius of a localised state, f_i and f_j are the probabilities of site i and j being occupied and W_H is given by equation (2.56). Emin has pointed out that in this situation multi-phonon hopping will freeze out at low temperatures leaving single phonon hopping. Thus, in equation (2.58), as $T \rightarrow 0$ $W_H \rightarrow 0$ giving a form similar to the Miller-Abrahams expression, with $Ln\sigma \propto 1/T^{1/4}$. The transition temperature to single phonon hopping should be given by $\Delta \sim \hbar\omega_0$, where Δ is a typical difference in energy between two sites, $\Delta \sim kT_0^{1/4}T^{3/4}$ (equation (2.23)).

Emin (1975) has considered the thermopower for strong electron-phonon coupling and finds:

$$S \propto T^{1/2} \tag{2.59}$$

Emin's treatment is of somewhat limited application for a real system since he has only considered the two site hopping probability, has not taken into account of site occupation probabilities and not averaged over the whole conductance network. Therefore, his results can only serve as a rough guide.

2.5 Summary

The present author has attempted to summarize theories which he believes are most useful for an explanation of his results on ferrites. It remains to make a synthesis of these ideas in Chapter 5 in order to throw some light on the observed electrical behaviour of these complex materials.

Chapter 3

SURVEY OF PREVIOUS INVESTIGATIONS

3.1 Introduction

Since Verwey (1939) showed that there was a two orders of magnitude transition in the electrical conductivity at ~120K in "pure" magnetite, many workers have investigated this oxide to try to understand the conduction processes involved. By doping with impurities a further understanding of the conduction process can be achieved. The spinel ferrous ferrites have been found to have the common chemical formula $M_XFe_{3-X}O_4$, where M is a cation that usually has a site preference and an ionic valency of 1+, 2+, 3+ or 4+: in some cases, e.g. manganese, a combination of valences is possible. It has been over fifty years since Verwey published his results and many workers have produced papers since then.

This chapter is devoted to a survey of previous work on only a selected number of spinel ferrous ferrites; these are Cobalt, Nickel, Zinc, Manganese, Titanium and Fluorine doped ferrites. Each section will start with the earliest work on a par-

ticular type of ferrite and then give the ionic formula to indicate the site preference of the cation. Then the papers of selected authors will be reviewed, showing their results and their conclusions on the conduction process believed to be taking place. Corroborative work will also be cited, and finally an in-depth review will be given of the most up to date publication on a particular ferrite system.

Throughout this chapter, when the ionic formula is given the characters A and B indicate tetrahedral and octahedral site preferences, respectively.

3.2 Early Measurements on Ferrite Samples

3.2.1 Cobalt Ferrite $(Co_XFe_{3-X}O_4)$

Jonker (1959) became interested in the fact that by increasing the cobalt concentration in magnetite, at room temperature, the resistivity gradually increased until X=1 where upon the resistivity increased sharply and then began to fall slowly for increasing X. Consequently, he investigated this ferrite system, by making resistivity and thermopower measurements on polycrystalline cobalt ferrite with 0.9<X<1.1, having ionic formulae:-

$$0 < X < 1 \qquad [Fe^{3+}]_A[Co_X^{2+}Fe_{1-X}^{2+}Fe^{3+}]_BO_4^{2-} \tag{3.1}$$

$$1 < X < 2 \qquad [Fe^{3+}]_A[Co^{2+}Co_{X-1}^{3+}Fe_{2-X}^{3+}]_BO_4^{2-} \tag{3.2}$$

An advantage of this system is that both cobalt and iron show the Verwey type conduction:-

$$Fe^{2+} \equiv Fe^{3+} + e^- \qquad Co^{3+} \equiv Co^{2+} + h^+ \tag{3.3}$$

where e^- and h^+ represent an electron and hole respectively. Hence, both n- and p-type semiconductivity can be studied by simply changing the cobalt concentration.

An oilbath was used to obtain the elevated temperatures for the resistivity and thermopower measurements and a two-probe method for the resistivity. The results obtained by Jonker are shown in figures [3.1-3.3] — Jonker has used $Co_{3-X}Fe_XO_4$ with $1.9 \leq X \leq 2.1$ to represent colbalt ferrite.

Jonker suggested a hopping type conduction, and rejected the band theory on the grounds that a low mobility with an exponential temperature dependence was observed. Jonker used equation (2.58) to calculate the mobility i.e. he assumed adiabatic polaron hopping in a medium in which disorder was small.

Assuming that every Fe^{2+} contributed an electron and every Co^{3+} contributed a hole to the conductivity, Jonker calculated the mobilities for electrons to be $\sim 10^{-4} cm^2V^{-1}s^{-1}$ and $\sim 10^{-8} cm^2V^{-1}s^{-1}$ for holes, with activation energies 0.2eV and 0.5eV respectively. Using these μ and W_H values in equation (2.58) Jonker calculated the phonon frequencies to be in the interval 10^{12} 10^{14}Hz. This he claimed was satisfactorily close to the expected 10^{13}Hz, considering ω_0 was sensitive to the activation energy. Using approximately the same measuring techniques Gillot and Jemmali (1983) obtained comparable values to that of Jonker for μ, W_H and frequency.

Gillot (1982) in a subsequent paper analysed cobalt ferrite with $0<X<1$ by measuring the thermopower, with a $20 \rightarrow 25$K temperature gradient across the sample. Taking a small polaron approach to the conduction, the theoretical expression he obtained was identical to the Heikes formula,

$$\text{Heikes} \qquad \Theta = \frac{-k}{e}\left[\text{Ln}\left[\frac{1-c}{c}\right] + \alpha\right] \tag{3.4}$$

if the kinetic term (α) was assumed to be approximately zero and $c=(1-X)/(2-X)$, where c is the fractional number of divalent B-site iron ions:-

$$\Theta = \frac{-k}{e}\text{Ln}\left[\frac{1}{1-X}\right] \tag{3.5}$$

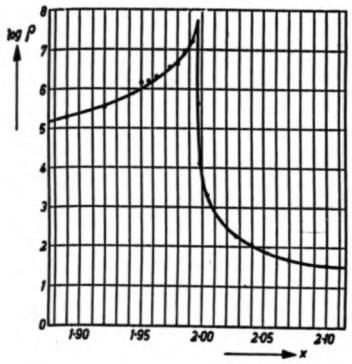

Figure 3:1 Room temperature values of log resistivity for a series of mixed crystals of $Co_{3-x}Fe_xO_4$ near the composition $CoFe_2O_4$. (Jonker, 1959)

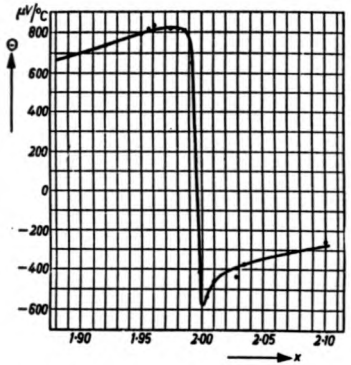

Figure 3:2 Thermopower data of $Co_{3-x}Fe_xO_4$. (Jonker, 1959)

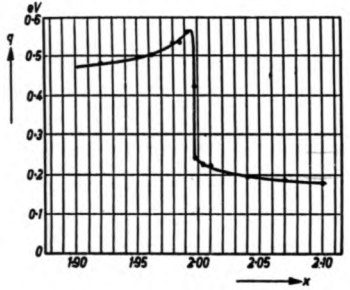

Figure 3:3 Activation energies (at T=450K) of the conductivity of mixed crystals $Co_{3-x}Fe_xO_4$. (Jonker, 1959)

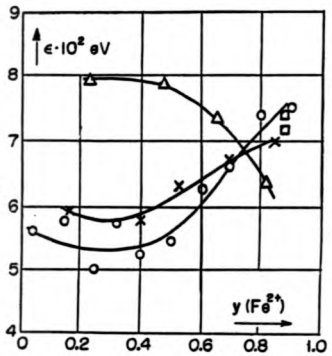

Figure 3:4 Activation energies (ϵ) of $(MeFe_2O_4)_{1-y}(Fe_3O_4)$ versus y; the symbols are Δ: Ni; $\bigcirc$: Mn; and $\times$: Zn. (Miyata, 1961)

Gillot achieved a good agreement with the results obtained and concluded that small polaron hopping occurred only between octahedral lattice sites.

3.2.2 Nickel Ferrite $(Ni_XFe_{3-X}O_4)$

The ionic formula is:-

$$0 \leq X \leq 1 \qquad [Fe^{3+}]_A[Ni_X^{2+}Fe_{1-X}^{2+}Fe^{3+}]_BO_4^{2-} \tag{3.6}$$

Nickel ferrite has been investigated for nearly thirty years. Because there have been vast numbers of papers published on nickel ferrites, only a few of the most important papers will be discussed.

Miyata (1961) made conductivity measurements on $Ni_{1-Y}Fe_{2+Y}O_4$ in the temperature range 100K-300K. Fitting the data to equation (2.58) and calculating the activation energies, Miyata found them to be in the range $(5\sim8)\times10^{-2}$eV, which were comparable with Lavine's (1959) results. Miyata found, as can be seen from figure [3.4], that the activation energy decreased with increasing Y (alternatively, increases with X in equation (3.6)). This agreed with the later results of Kohane and Silverman (1962) to within $\pm5\%$.

A more thorough investigation into nickel doped ferrites was made by Griffiths et al (1970). For all Y ($0\leq Y\leq1$) they made thermopower and four-probe resistivity measurements between 20K and 1100K. At low temperatures when the resistivity became too high a two-probe technique was implemented. The results are shown in figures [3.5-3.6]: figure [3.5] shows the thermopower versus reciprocal temperature. The most striking feature is the development of a peak for sample Y=0.046 (i.e. high nickel concentration) as the temperature is lowered. They attributed this behaviour to imperfections within the sample and consequently did not consider this feature any further.

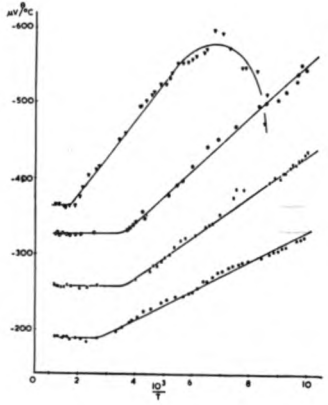

Figure 3:5 Thermopower for $Ni_{1-X}Fe_{2+X}O_4$ versus 1000/T; ▼: X=0.046; ○: X=0.076; ×: X=0.13; ●: X=0.21. (Griffiths et al, 1970)

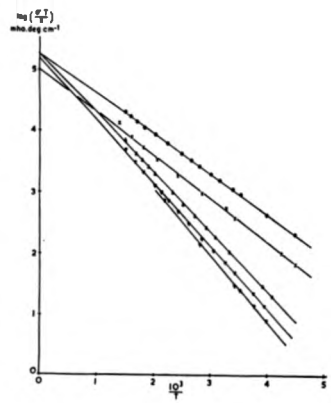

Figure 3:6 Temperature dependence of $\sigma T/X$ for $Ni_{1-X}Fe_{2+X}O_4$; ●: X=0.21; ×: X=0.13; Δ: X=0.06; ▼: X=0.046; ▽: X=0.03. (Griffiths et al, 1970)

Griffiths et al (1970) used equation (2.58) to discuss their resistivity results and obtained good agreement with the experimental data as can be seen in figure [3.6]. For the thermopower analysis they used equation (3.4). They found that their thermopower data did not agree accurately with this equation and did not give a reason why. Over a substantial temperature range the thermopower varied as 1/T, but the authors could not suggest a conduction mechanism that would account for this behaviour.

Whall et al (1986) have made electrical conductivity and thermopower measurements on single crystals of nickel ferrous ferrite in the temperature range 10K–300K. The results are shown in figures [3.7–3.12]. They discussed the features in depth and in terms of variable-range and nearest-neighbour hopping between Anderson localized states commencing with the conductivity as follows:

The $G(\sigma T)$ peaks shown in figure [3.7] [$G(\sigma T)$=dLn(σT)/d(1/T) – see section 5.5], which indicate a Verwey transition, become suppressed for $X \geq 0.2$. This transition was taken as evidence for the disappearance of long range order as predicted by Lorenz and Ihle (1975). For higher values of X a broader peak is still observed. The authors believed that this broad peak, in $G(\sigma T)$ (see section 2.3), was caused by the formation of a Coulomb Gap in the density of states followed by a transition to many-electron hopping, which required a smaller activation energy, at the lower temperatures.

For very high concentrations of X, they assumed that the Coulomb Gap was suppressed by disorder and they expected to observe a $T^{-1/4}$ law for low temperatures. As can be seen in figure [3.8] this is indeed observed for X=0.8 and X=0.9, but not so convincingly for X=0.6.

Ignoring a polaron contribution, the transition temperature between variable-range and nearest-neighbour hopping was calculated using $T_G \sim W/k\alpha a$ (Pollak and Knotek, (1979)), where α^{-1} is the radius of localization and "a" the lattice spac-

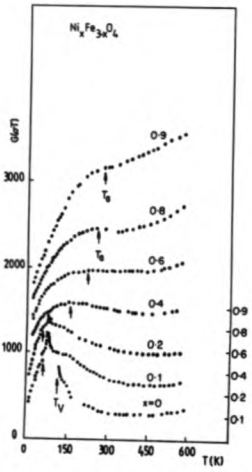

Figure 3:7 $|G(\sigma T)|$ (see equation 5.5) for $Ni_XFe_{3-X}O_4$ plotted against temperature. (Whall et al, 1986)

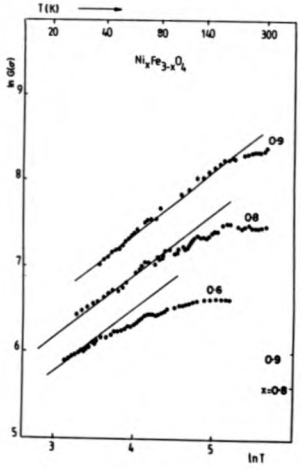

Figure 3:8 $Ln[G(\sigma)]$ versus $Ln[T]$ for $Ni_XFe_{3-X}O_4$ for $X \geq 0.6$. (Whall et al, 1986)

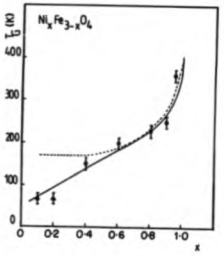

Figure 3:9 T_G versus X. ▲: for low concentrations; ●: for higher concentrations. (Whall et al, 1986)

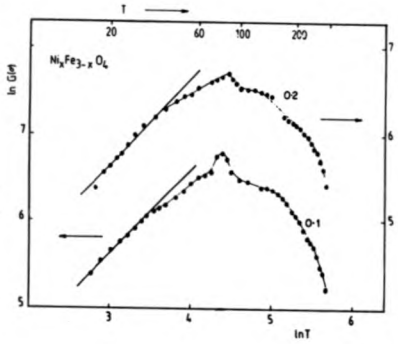

Figure 3:10 Ln[G(σ)] versus Ln[T] for $Ni_XFe_{3-X}O_4$ for X$\leq$0.2: lines of slope 1. (Whall et al, 1986)

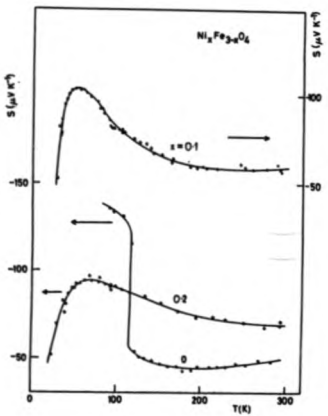

Figure 3:11 Thermopower of $Ni_XFe_{3-X}O_4$ versus temperature for X≤0.2. (Whall et al, 1986)

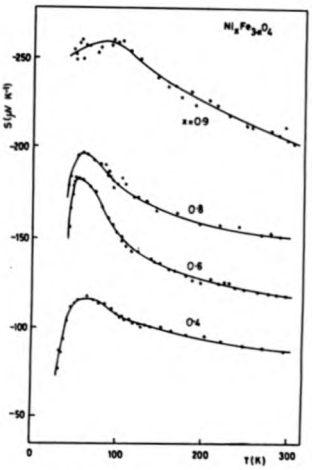

Figure 3:12 Thermopower of $Ni_XFe_{3-X}O_4$ versus temperature for X>0.2. (Whall et al, 1986)

ing, and compared with the values taken from the experimental results (see figure [3.9]). As can be seen the fit is good, thus suggesting that the conduction is by a single-electron hopping mechanism. For low concentrations of X a slope of $\sim$1 is observed in figure [3.10] where LnG(σ) is plotted versus Ln(T), which was noted to be consistent with the predictions of Pollak and Knotek (1979) for many-electron hopping. None of the samples measured at low temperatures showed the Ln$\sigma \propto T^{-1/2}$ tendency predicted by Efros and Shklovskii (1975), thus suggesting that the density of states was non-zero in the Coulomb Gap (see sections 2.3.3 and 2.3.4).

The thermopower results of Whall et al (1986) (figures [3.11-3.12]) show a maximum at low temperatures for each value of X. This was interpreted as being due to a transition from nearest-neighbour to variable-range hopping for high values of X, and due to a transition from excitations across a Coulomb Gap to many-electron hopping at low X. The thermopower maxima for various X occur at approximately the same temperatures. Below this peak the thermopower falls off more rapidly than the expected $T^{1/2}$ law predicted by Zvyagin (1973), Kosarev (1975) and Overhof (1975). The authors dedicated the remaining part of their paper to this feature. They examined the thermopower using equation (2.25) with a density of states rectangular in shape and obtained:-

$$S = \Pi/T = (kT_0^{1/4}.T^{3/4} - E_f)/2eT \tag{3.7}$$

where T_0 was a constant. In this interpretation S initially rises as the temperature decreases, passing through a maximum at:

$$T_S \sim (4E_f/kT_0^{1/4})^{4/3} \tag{3.8}$$

and subsequently falling more rapidly than $T^{1/2}$. Good agreement was claimed between the experimental and theoretical results considering the crudeness of the analysis.

3.2.3 Zinc Ferrite $(Zn_XFe_{3-X}O_4)$

There is very little literature on this ferrite system, especially for liquid helium temperatures. Possibly the reason for this is the high resistivity at such extreme temperatures, see Chapter 5.

According to Verwey and Heilmann (1947) and Gillot et al (1981) the zinc ion has an A-site preference, thus the ionic formula for zinc ferrite is:-

$$[Zn_X^{2+}Fe_{1-X}^{3+}]_A[Fe_{1-X}^{2+}Fe_{1+X}^{3+}]_BO_4^{2-} \tag{3.9}$$

Miyata (1961) obtained activation energies by plotting Lnρ versus 1000/T in the temperature range 77K-300K and his results are shown in figure [3.4] . It can be clearly seen that the activation energy gradually increases for increasing y, which corresponds to decreasing X in formula (3.9). The temperature at which these activation energies were calculated has not been given, which is an important omission, because the activation energy is a function of temperature. The author says that this result at present has no theoretical explanation and so cannot take the analysis further. This activation energy trend has been confirmed by Gillot et al (1981).

A more in-depth investigation into the conductivity processes in zinc ferrite was carried out by Srinivasan and Srivastava (1981). Thermopower measurements, in the temperature range 77K-700K, were made upon polycrystalline samples. Thermopower data at 300K are compared with -k/e.Ln(c), where c=(1-X)/2, which show good agreement between the theoretical and experimental results (see Table 3.1). Gillot (1982) obtained similar values. For the analysis of the conductivity results the authors assumed that the electrons which participate in the $Fe^{2+} \rightleftharpoons Fe^{3+} + e^-$ exchange process tunnelled from one to another due to a phonon-induced transfer mechanism which was essentially the same as Miller-Abrahams. They applied equation (2.58) and found a good fit but the temperature range was limited to 77K and

above.

For completeness, the results by Gillot et al (1981) will be tabulated (Table 3.2) because they will be relevant to the Results and Discussion chapter.

No literature presented here has given results for thermopower and/or electrical conductivity below liquid nitrogen temperature. Consequently no comprehensive discussion of the conduction processes involved for this system of spinel ferrous ferrite, at such temperatures, has been tested or developed.

3.2.4 Manganese Ferrite $(Mn_XFe_{3-X}O_4)$

Because of its many possible valences, manganese can replace all the iron ions in magnetite i.e. a complete range of solid solutions is possible, $Fe_3O_4 \rightarrow Mn_3O_4$ (Hausmanite). Lotgering (1964) and Yamzin et al (1962) were some of the first workers to study the manganese ion distribution in ferrites. $Mn_XFe_{3-X}O_4$ can be represented by the formula:

$$[Mn^{2+}_{X-Y}Fe^{3+}_{1-X+Y}]_A[Mn^{2+}_{Y}Fe^{2+}_{1-X}Fe^{3+}_{1+X-Y}]_BO_4^{2-} \qquad (3.10)$$

for $0<X<1$. The cation distribution was investigated by Hastings and Corliss (1956) who found, by using neutron diffraction studies, that at least 80% were residing on the tetrahedral sites, suggesting that manganese has an A-site preference. Lotgering analysed the stability of the following chemical reaction:

$$Mn^{2+} + Fe^{3+} \rightarrow Mn^{3+} + Fe^{2+} \qquad (3.11)$$

on the octahedral sites, and found it to be endothermic. Lotgering further assumed that the Mn^{2+} ions on the B-sites acted as donor centres but did not contribute directly to conduction. Therefore, conduction was attributed to valence transfer between Fe^{2+} and Fe^{3+} on the B-sites, which was confirmed by Brabers (1969). The percentage of octahedral sites occupied by Mn^{2+} ions has been estimated by

Yamzin et al (1962) to be less than 10%. However, Brabers (private communication) recently measured the occupancy site of the manganese ions and discovered that with controlled heat treatment nearly 100% reside on the B-sites — much greater than previously measured. Therefore, "effectively" the manganese ionic formula is the same as that of zinc ferrite i.e. $Y \sim 0$ — see equation (3.9).

Funatogawa et al (1959) in a short note showed, using a four-probe technique for measuring the resistivity on $Mn_X Fe_{3-X} O_4$ where $0 \leq X \leq 1.14$ in the temperature range 100K-280K, that the activation energy fell with increasing X. He gave no explanation of this feature.

Simsa et al (1972a, 1972b and 1988) analysed manganese ferrites in more detail. In the first publication Simsa et al (1972a) measured this ferrite system with $X=0$ and $0.5 \leq X \leq 1$ below liquid nitrogen temperature and observed the samples obeying a $T^{-1/4}$ law for a short temperature interval but took the analysis no further. In a subsequent paper of Simsa et al (1972b) the conduction process was explained in terms of non-adiabatic small polaron hopping, because equation (2.58) gave a straight line in the temperature interval 150K-500K, but again no further analysis was made. A slightly more in-depth analysis was made in the last paper by Simsa et al (1988) on manganese ferrites. The thermopower and conductivity were measured on single crystals of $X=0$ and $0.5<X<0.95$ in the temperature range 10K-300K. A two-probe technique was used to measure the conductivity when the resistance became $\geq 10^6 \Omega$. The results obtained are shown in figures [3.13-3.14]. The authors observed a peak in the thermopower between 50K and 150K (figure [3.13]). From calculations the activation energy was seen to fall for increasing X, which confirmed Funatogawa et al's (1959) results. Simsa et al stated that the thermopower "seemed" to follow the relationship given by Zvyagin (1973) (equation (2.27)) $\Theta \propto T^{1/2}$, but no graph was shown as proof, or further information given. They also have fitted their results to a $T^{-1/4}$ law for variable-range hopping in the temperature range

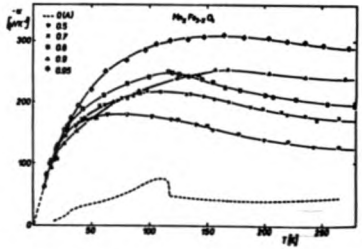

Figure 3:13 Temperature dependence of the Seebeck coefficient of Mn–ferrites. The symbols indicate the various contents. (Simsa et al, 1988)

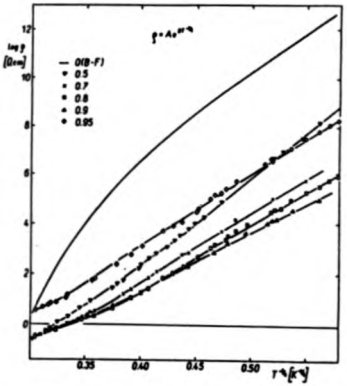

Figure 3:14 Demonstration of Mott's law for Mn–ferrites. (Simsa et al, 1988)

T<50K, as shown in figure [3.14]. However, it must be pointed out following Hill (1976) that other fractional powers of T will also give a straight line. More rigorous methods of determining the power of T are discussed in Chapter 5.

There is one point Simsa et al failed to comment on and it is shown in figure [3.13]. As can be clearly seen the thermopower results for $Mn_{0.8}Fe_{2.1}O_4$ cross the data for other samples and the question is why? Is it due to the variation in activation energy with temperature? or the measuring technique? or some other reason? Salerno (1986) measured the thermopower and electrical conductivity on single crystal manganese ferrites and this feature of "cross over" did not occur: shown in figure [3.15] is the thermopower versus temperature and in figure [3.16] a G-function of the conductivity versus temperature, where the G function is:

$$G(\sigma T^{3/2}) = \mid d\ln(\sigma T^{3/2})/d(1/T) \mid \tag{3.12}$$

The $T^{3/2}$ term comes from the assumption of non-adiabatic small polaron hopping in a disordered system (see equation (2.58)). The small cusp, associated with magnetic ordering is superimposed upon a gently increasing $G(\sigma T^{3/2})$ which is believed to be partly due to increasing disorder from the redistribution of the manganese cations.

Further in-depth investigation needs to be done to begin to understand the complex conduction processes in this ferrite system, especially at low temperatures.

3.2.5 Titanium Ferrite $(Ti_XFe_{3-X}O_4)$

Naturally occurring magnetite and its "alloys" have been analysed by geophysicists because they are rock forming minerals which are largely responsible for the earth's magnetism. In these magnetites the most frequently found impurity is titanium (Nicholls, (1955)).

According to Kuipers (1978) the ionic formulae for titanium ferrite are:

$$X < 0.5 \qquad [Fe^{3+}]_A[Fe^{2+}_{1+X}Fe^{3+}_{1-2X}Ti^{4+}_X]_BO_4^{2-} \tag{3.13}$$

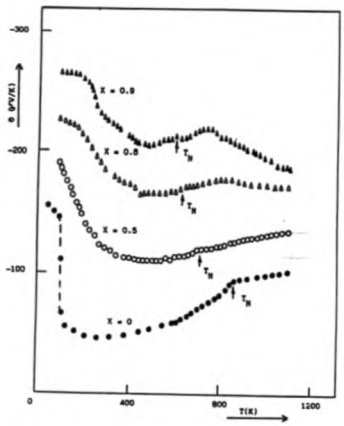

Figure 3:15 The variation of the thermoelectric power versus temperature for manganese ferrite, according to Salerno (1986).

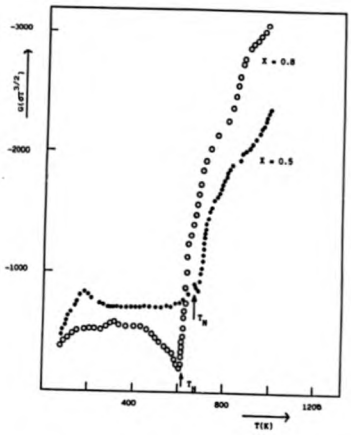

Figure 3:16 A plot of $G(\sigma T^{3/2})$ versus temperature for manganese ferrite. T_N is the Néel temperature. (Salerno, 1986)

$$0.5 < X < 1 \qquad [Fe^{2+}_{2X-1}Fe^{3+}_{2-2X}]_A[Fe^{2+}_{1-X}Ti^{4+}_{X}]_B O^{2-}_4 \qquad (3.14)$$

Kuipers (1978) measured single crystals of titanium ferrite with $0 \leq X \leq 1$ in the temperature range 77K–1000K. The results of the thermopower, electrical conductivity and Néel temperatures are shown in figures [3.17–3.19]. As can be seen the conductivity has a straight line on the Arrhenius plot but deviates from linearity in the lower temperature region. The activation energies were calculated from this plot and the variation with concentration is shown in figure [3.20]. However, no allowance was made for the pre-exponential factor (equation (2.58)). Kuipers took this to be independent of temperature which could influence further interpretation of the results (see section 5.5).

To aid interpretation of the lower temperature region the logarithm of the conductivity data was plotted versus $T^{-1/4}$ (figure [3.21]). This law appeared to be obeyed, but calculation of the G-factor (see section 5.5) would have been preferable to find the power of T, instead of merely assuming Mott's law. The temperature (T_C) at which the conductivity "switches" from a $T^{-1/4}$ law to a T^{-1} law was plotted versus concentration (see figure [3.22]). The graph is linear passing through the origin, but several workers have found that magnetite itself obeys a $T^{-1/4}$ law at low temperatures. (Graener, Rosenberg, Whall and Jones (1979) for instance). This could be due to a small but finite concentration of residual impurities.

The thermopower is negative for all the temperature range when $X \leq 0.5$, becoming positive for increasing X, indicating a breakdown of Heikes law.

Kuipers believed that the conduction was by hopping between localized sites because the laws T^{-1} and $T^{-1/4}$ were obeyed and $\alpha a \sim 20$, calculated from the data, which suggested a high degree of localization (see section 5.5.2). At no point did the electrical conductivity or the thermopower directly indicate magnetic ordering effects at the Néel temperature. Because of this Kuipers concluded that magnetic

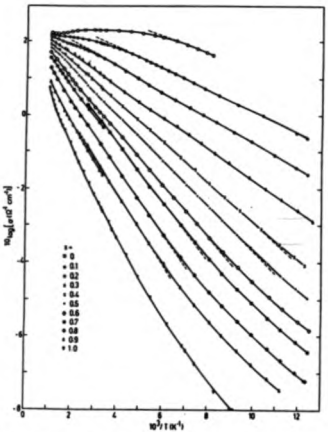

Figure 3:17 Logarithm of the conductivity of $Fe_{3-x}Ti_xO_4$ versus 1000/T. The dashed lines indicate the linear part of the curves from which the activation energies E_σ have been calculated. (Kuipers, 1978)

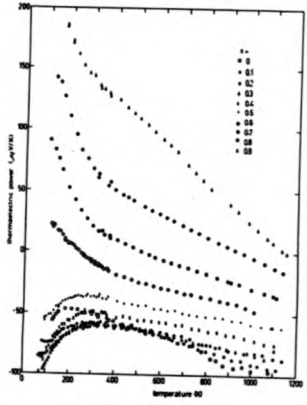

Figure 3:18 The temperature dependence of the thermopower of the mixed series $Fe_{3-x}Ti_xO_4$. (Kuipers, 1978)

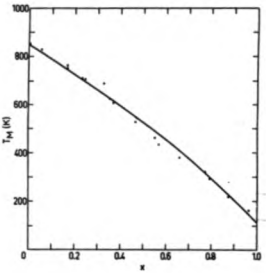

Figure 3:19 The magnetic transition temperature T_M of $Fe_{3-X}Ti_XO_4$ as a function of X. (Kuipers, 1978)

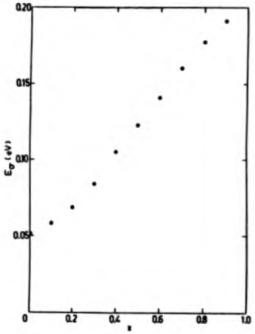

Figure 3:20 The composition dependence of the activation energies E_σ in $Fe_{3-X}Ti_XO_4$ determined from figure [3.17]. (Kuipers, 1978)

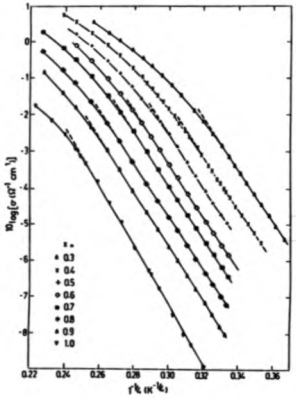

Figure 3:21 The low temperature data of figure [3.17] plotted versus $T^{-1/4}$. The dashed lines indicate the linear part of the curve. (Kuipers, 1978)

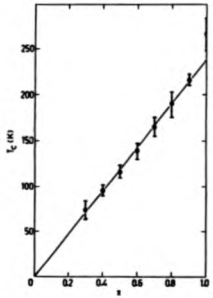

Figure 3:22 The transition temperature (T_C) from $T^{-1/4}$ law to T^{-1} law plotted versus X for $Fe_{3-X}Ti_XO_4$. (Kuipers, 1978)

ordering had little effect on the hopping process. Also, there was no mention of why the thermopower became more negative for increasing in X before becoming progressively positive.

3.2.6 Fluorine Ferrite $(Fe_3O_{4-X}F_X)$

Fluorine has almost the same ionic radius as oxygen and can therefore substitute relatively easily (Schieber, (1964)). The ionic formula is:-

$$[Fe^{3+}]_A[Fe^{2+}_{1+X}Fe^{3+}_{1-X}]_B O^{2-}_{4-X}F^-_X \tag{3.15}$$

Therefore, the ratio of Fe^{2+} to Fe^{3+} can be altered without introducing impurity ions into the cation sublattices where the conduction takes place.

Whall, Rigo, Jones and Pointon (1977) were one of the first workers to analyse fluorine doped magnetite and try to understand its conduction mechanisms. They made electrical conductivity and thermopower measurements down to liquid nitrogen temperature on samples having $0 \leq X \leq 0.25$. Their results are shown in figures [3.23–3.24].

The Heikes formula based on small polaron hopping (equation (3.4)) was applied to the thermopower data at T=300K, where $c=(1+X)/2$. As can be seen in figure [3.25] for increasing X the thermopower becomes more negative while Heikes formula predicts the exact opposite. Whall et al concluded from this that the influence of disorder was crucial.

Graener, Rosenberg, , Whall and Jones (1979) have investigated fluorine ferrite further and paid more attention to lower temperatures. Below 100K all the samples have a $T^{-1/4}$ behaviour, even those with a Verwey transition. The authors believed this feature to be due to the electron "seeing" a random field caused by substitutional disorder. They attributed the maximum in the thermopower to a

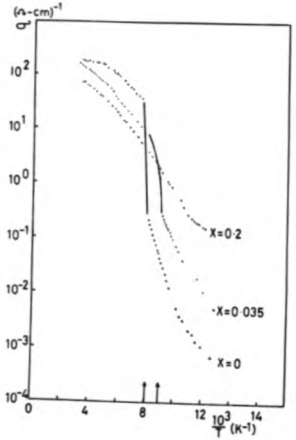

Figure 3:23 Conductivity of $Fe_3O_{4-X}F_X$ versus 1000/T. The arrows indicate the Verwey temperatures of the samples X=0 and X=0.035. (Whall et al, 1977)

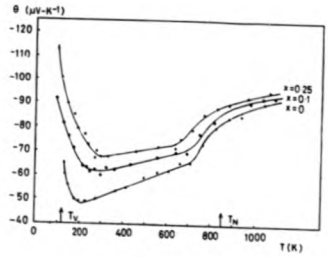

Figure 3:24 Seebeck coefficient of $Fe_3O_{4-X}F_X$ as a function of temperature. The Verwey temperature (T_V) and the Néel temperature (T_N) of the sample X=0 are indicated on the figure. (Whall et al, 1977)

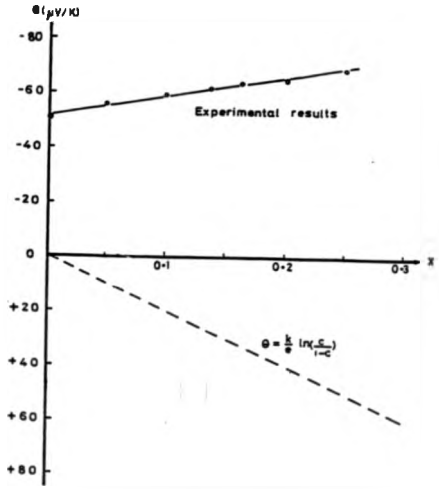

Figure 3:25 Measurements of the thermopower of $Fe_3O_{4-x}F_x$ (at T=300K) compared against the predictions of the Heike's formula. (Jones, 1985)

transition from nearest-neighbour to variable-range hopping and using equation (2.30) found $\alpha a \sim 7$.

3.3 Summary

Early workers (Gillot (1982), etc) assumed small polaron hopping, ignored disorder and used the Heikes formula to discuss their thermopower data. Subsequently the breakdown of the Heikes formula in Fe_3O_4–Ni, Fe_3O_4–F and Fe_3O_4–Ti cast doubt on this approach. The observation of a $T^{-1/4}$ law in the conductivity for Fe_3O_4–F, Fe_3O_4–Ti and Fe_3O_4–Ni suggested that disorder effects were crucial to an understanding of the conduction mechanisms. The peak in $d\mathrm{Ln}(\sigma T^N)/d(1/T)$ observed near 100K in $Ni_XFe_{3-X}O4$ indicated that the Coulomb Gap in Fe_3O_4 was not completely suppressed by disorder and that its presence was also influencing conduction.

Further work is needed to disentangle the effects of polarons, disorder and electron–electron interaction effects. Much of the early work was on polycrystalline material and covered a limited temperature range. The production of single crystals of $Mn_XFe_{3-X}O_4$ and $Zn_XFe_{3-X}O_4$ by Brabers (1971) has made these materials suitable for study. They are attractive because their cation distributions:-

$$[Mn^{2+}_{X-Y}Fe^{3+}_{1-X+Y}]_A[Mn^{2+}_{Y}Fe^{2+}_{1-X}Fe^{3+}_{1+X-Y}]_BO_4^{2-} \tag{3.16}$$

$$[Zn^{2+}_{X}Fe^{3+}_{1-X}]_A[Fe^{2+}_{1-X}Fe^{3+}_{1+X}]_BO_4^{2-} \tag{3.17}$$

give systems having vertical disorder but no horizontal disorder: but of particular significance is the fact that because Mn and Zn have A-site preferences the disorder potential on the B-sites is small and narrow, which should yield much more prominent features associated with the Coulomb Gap. The present work has been concerned with these materials and its results are discussed in Chapter 5.

Table 3.1: Properties of $Zn_XFe_{3-X}O_4$ at 300K — Srinivasan and Srivastava, (1981)

Value X	Θ (exp.) (μV/K)	Θ (theor.) (μV/K)
0.0	− 48	− 52
0.2	− 75	− 79
0.4	120	104
0.6	140	139

Table 3.2: Properties of $Zn_XFe_{3-X}O_4$ — Gillot et al, (1981)

Value X	Θ (μV/K)	W_A (eV)
0.00	− 55	0.000
0.15	71	0.041
0.27	77	0.055
0.57	153	0.059

Chapter 4

EXPERIMENTAL WORK

4.1 Introduction

The cryostat used in this investigation has been inherited from Yeung (1982). After a close examination of the sample holder and inspection of the results obtained by Yeung, it was felt that several improvements could be made. Firstly, the lower temperature limit for thermopower and resistivity could be pushed closer to 4.2K — for thermopower the lowest temperature reached previously in this cryostat was $\simeq$28K, and $\simeq$10K for resistivity. Secondly, measurements of resistivity could be extended to higher values of source resistivity — previous measurements being limited to $<5\times10^{8}\Omega$.cm. This improvement could be achieved by utilizing driven shield techniques to lower RC time constants and reduce leakage currents. A special pinseal for these shields was designed (see section 4.9). Close examination suggested that the thermal anchoring of the electrical leads could be improved and this was carried out (see section 4.6). Yeung in common with most other workers used thermocouples for thermopower measurements — however, they have low sensitivities and therefore suffer from a poor signal to noise ratio. To overcome this problem

silicon diodes were considered and implemented for the first time as they appeared to be far superior to thermocouples (see section 4.4). These changes to the cryostat required the achievement of a sample isolation of $>10^{14}\Omega$.

Before these points are discussed in more detail, the samples measured are described.

4.2 Samples Measured

The samples used for measuring thermopower and resistivity were as follows:

$Mn_XFe_{3-X}O_4$ X = 0.1, 0.2, 0.5, 0.8, 0.9

$Zn_XFe_{3-X}O_4$ X = 0.1 (Poly), 0.1, 0.4, 0.6, 0.8, 1.0 (Poly).

All the samples discussed are single crystals except for two which are indicated as "Poly".

The single crystals were grown by Brabers using a zone-melting method (Brabers, (1971)). An arc-image furnace consisting of two elliptical mirrors and a xenon lamp produced the hot zone. The technique uses polycrystalline bars of desired chemical composition with a seed crystal having a crystalline orientation of <110> attached to one end. The bar shaped sample, enclosed inside a silica tube, allowing for inert atmospheres, is passed vertically through the hot zone (see figure [4.1]). A 5mm diameter bar several centimetres in length can be grown, which is always oriented in the <110> direction (Kuipers, (1978)). Because of the technique employed, large thermal stresses are present within the sample. To overcome such stresses, Brabers anneals the samples for ~70hrs at 1200°C.

The polycrystalline samples X=0.1 and X=1.0 were manufactured at Portsmouth Polytechnic. They were produced by ballmilling the desired compositions for several hours, sieving and then compressing them into 10mm diameter x 12mm length pellets. Lastly, they were fired at 1200°C in an inert atmosphere for ~12hrs

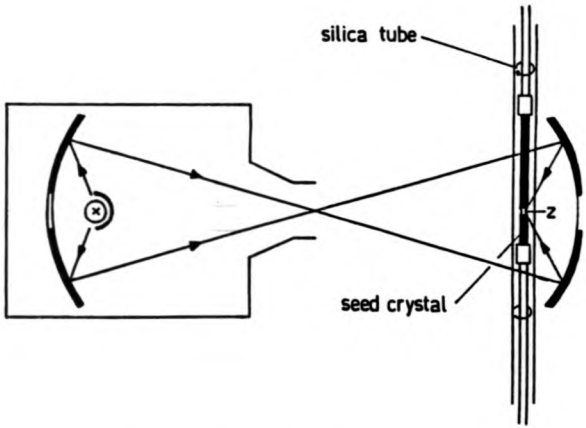

Figure 4:1 Diagram of the arc–image furnace used in the floating zone technique. (Brabers, 1971)

(Griffiths et al, (1970)).

4.2.1 Preparation of Samples

The technique used by Brabers to grow $Zn_XFe_{3-X}O_4$ samples (see section 4.1) tends to evaporate a small amount of zinc oxide from the sample surface. Evaporation did not occur for $Mn_XFe_{3-X}O_4$ ferrites during growth (V.A.M. Brabers, private communication). To obtain a standard size for both sets of samples and to increase the homogeneity across the diameter, they were turned using a diamond encrusted grinding wheel to give 4mm diameter rods. The polycrystalline zinc ferrites were sectioned and then turned to size as for the single crystals.

All the samples were cut to $\simeq$10mm lengths and their end faces made parallel for mounting in the sample holder (see section 4.3). For chemical composition analysis, using the EPMA technique (see section 4.2.2), a small piece of each ferrite was put into separate cylinders of bakelite and polished using 1-micron diamond paste.

4.2.2 Characterization of Samples

Electron Probe Micro-Analysis (EPMA) is a technique for measuring sample compositions non-destructively. A beam of high energy electrons focussed on a material produces X-rays, a consequence of an electron falling to a lower energy level stabilizing the atom. The energy of the X-ray is determined by the sharply defined energy levels in the atom. Because different atomic number atoms have different energy levels, the X-ray produced is characteristic of a particular atom.

The apparatus is calibrated against a standard element (Cobalt) that is extremely chemically stable. These calibration data are then used as a reference point for the other elements. The nominal and measured X values are shown in the Results

and Discussion chapter, Tables 5.1–5.2.

As a check that the measurements taken were accurate, a piece of the polycrystalline $ZnFe_2O_4$ ferrite was sent to Birmingham University for "Flame Atomic Absorption Spectrometry", which has a typical accuracy of ±3%. The technique involves dissolving a pre–weighed quantity of the powdered sample into hydrochloric acid (HCl) giving an overall acidity of ≃0.1M. A duplicate dilution was prepared as a check, and also a blank using the same technique. The sample under test was compared with zinc and iron standards, produced from high purity Fe_2O_3 and $ZnSO_4.7H_2O$ compounds, giving $Zn_{0.95}Fe_{2.05}O_4$ as the chemical composition. Comparing this zinc ferrite result with that shown in Table 5.1, they agree favourably.

The homogeneity of the samples was measured. EPMA measurements across the diameter and along the length of the ferrites showed that the concentrations was constant to within the measurement accuracy (±3%) of the EPMA apparatus.

4.3 Sample Holder

The design of the sample holder was based on the desirability of carrying out measurements of thermopower and resistivity on the same sample during one cryogenic temperature cycle. By this means, fewer wires were necessary to the sample holder, thereby reducing the total heat flow down inside the cryostat. This arrangement also reduced liquid helium consumption.

Thermopower measurements require samples large enough so that a temperature interval ΔT can be produced across them. Because the samples were uniform rods of 4mm diameter and length ≃10mm, a conventional four probe rather than a van de Pauw (1958) technique could be used to measure resistivity.

4.3.1 Choice of Thermopower Technique

There are two methods of measuring the Seebeck coefficient of a material, these being the Differential and Integral methods. Both principles are discussed in certain thermoelectricty text books (e.g. Heikes and Ure, (1961)) and are shown schematically in figures [4.2–4.3]. For the integral method one end of the sample is kept at a constant but known temperature T_0 whilst the other is raised or lowered through a temperature range. The thermally induced voltage is measured as a function of temperature. Since,

$$V(T) = \int_{T_0}^{T} S(T).dT \tag{4.1}$$

then the Seebeck coefficient can be calculated by differentiating V(T) with respect to temperature. For this measurement to work over an appreciable temperature range the sample needs to be long and thin, like a piece of wire, to achieve the large temperature gradients necessary.

The differential method requires a smaller temperature gradient across it, between 3K–5K, and so the samples under investigation can be considerably smaller. The Seebeck coefficient can be calculated easily once the thermal voltage has been measured since,

$$S(T) = \lim_{\Delta T \to 0} \frac{\Delta V(T)}{\Delta T} \tag{4.2}$$

Because ΔT is small, this technique is sensitive to spurious voltage offsets. To overcome these, several measurements of ΔV(T) versus ΔT must be taken whilst keeping the mean temperature as constant as possible. The gradient of a ΔV(T) versus ΔT plot then gives the Seebeck coefficient. A typical graph obtained by the author is shown in figure [4.4] for magnetite (Fe_3O_4) at room temperature. Because the samples to be measured in this case were small, the differential method was chosen; although a slow process it does have the advantage of immediately indicating any discontinuities in the thermopower e.g. occurring at the Verwey transition.

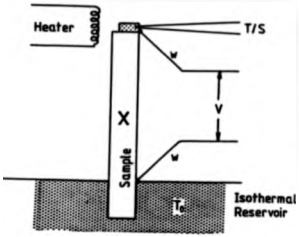

Figure 4:2 The integral method for measuring the thermopower. T/S – temperature sensor.

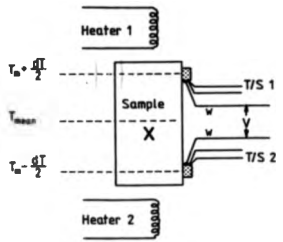

Figure 4:3 The differential method for measuring the thermopower. Sample X has a temperature gradient dT along its length. T/S – temperature sensor.

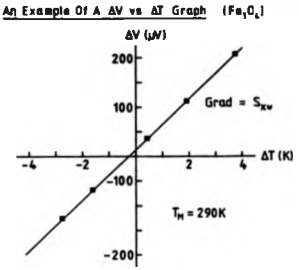

Figure 4:4 A typical plot of the ΔV versus ΔT at room temperature for magnetite. The relative seebeck coefficient can be found from the slope.

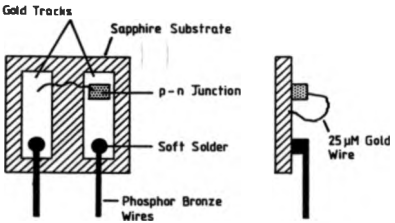

Figure 4:5 A schematic diagram of a silicon diode used for measuring the temperature. (Igra et al, 1986)

For both integral and differential methods the Seebeck coefficient calculated is the sum of both sample (S_X) and reference wire (S_W). To find S_X, the absolute Seebeck coefficient for the wire is required throughout the whole temperature range. Hence,

$$S_X = S_W - \frac{\Delta V(T)}{\Delta T} \tag{4.3}$$

Most semiconductors tend to have relatively high absolute Seebeck coefficients compared with copper; Cu having $\sim 3\mu V/K$ at room temperature unlike that of cromel and other materials used for thermocouples ($\sim 21\mu V/K$). Even if the Seebeck coefficient of copper has a low accuracy (in fact <10%) it will have little effect on the final result because ferrites tend to have Seebeck coefficients $>|50\mu V/K|$. For this very reason copper was used as the reference material, hence $S_W \cong S_{Cu}$ (Landolt-Börnstein, (1959)).

4.3.2 Thermopower and Resistivity Configurations

The arrangement for making four-probe measurements of resistivity, which of course been influenced by the need to make differential measurements of thermopower on the same sample and in the same experimental run, is shown in figure [4.3]. A copper platelet at each end of the sample gave electrical contacts for the current when making resistivity measurements. The copper wires attached to the side of the sample allowed for the thermoelectric and resistivity voltages to be measured.

The setup is intended to avoid the the two obvious pitfalls in the resistivity and thermopower measurements i.e. the existence of charge and heat flow across potential and thermometer contacts which give rise to errors.

4.4 Choice of Temperature Sensor

For accurate thermopower measurements the thermoelectric voltage wires need to be in good electrical contact with the sample and extremely close to the temperature sensor. In some aspects, thermocouples are well suited to this purpose because one "leg" of each thermocouple can be used to measure the thermoelectric voltage (see Yeung, (1982)). Thermocouples are widely used for measuring ΔT because they are easily fabricated, reasonably stable and reproducible. The most common types used are copper versus constantan for the range 77K to 300K and gold(0.07at%/iron) versus cromel (Ni90%/Cr10%) for the 4K to 300K temperature range. For a thermocouple to work well a reference junction is essential such as ice or a cryogenic fluid. If an ice junction is used its temperature needs to be continuously monitored and replenished with fresh ice, sometimes stirred, to achieve good temperature stability and even then problems can occur (Caldwell, (1965)). Liquid nitrogen is widely used in cryogenics but will drift in temperature if allowed to absorb air. An alternative is liquid helium but its use as a reference junction, without breaking the wires to the sample, is difficult to implement — virtually impossible if the preferred gold(0.07at%/iron) versus cromel thermocouple is used. For a thermocouple to work accurately it needs to be calibrated 'in situ' because its calibration may change during removal or installation. Calibration tables for gold alloy thermocouples are difficult to achieve accurately because of inhomogeneities (Powell et al, (1962)). Thermoelectric offsets $\simeq 1\mu$V can cause serious problems (Hall, (1966)) as thermocouples tend to have low sensitivities i.e. $\simeq 16\mu$V/K for gold(0.07at%/iron) versus cromel throughout the 4K to 300K temperature range (White, (1979)). Because of these disadvantages an alternative temperature sensor was sought.

Semiconductor diodes have been used as temperature sensors for more than twenty years and have been commercially available since 1974 (Lake Shore Cryogen-

ics Bulletin, CT-742). In the present work silicon diode thermometers have been used for the first time to make thermoelectric power measurements as reported in "The Journal of Scientific Instruments", (Phillips et al, (1989)).

4.4.1 Silicon Diodes

Owing to their greater sensitivity below 100K (Swartz and Swartz, (1974)) silicon diodes are preferred to the gallium arsenide diodes. The diodes used are small as compared with ordinary resistance thermometers, are better in sensitivity than thermocouples and also hold their calibration if not damaged. They have been purchased from Southampton University (ref. Southampton University) and called "Southampton Miniature Diode Temperature sensors", (SMDT). A schematic diagram of an SMDT diode is shown in figure [4.5]. It consists (Igra et al, (1986)) of a p-n junction deposited upon a 2mm × 2mm × 1mm sapphire platelet which gives it an excellent thermal response ($\simeq 5\mu$S at 4.2K, ref. Southampton University - - data sheet) and electrical isolation. A parylene coating to help prevent damage and contamination covers the p-n junction, two electrical tracks and the 25μM gold wire that connects the two tracks. Two 36swg phosphor bronze wires are soldered to the tracks for ease of electrical connection. Typical silicon diode voltages are 0.5V at 300K and 1.7V at 4.2K; their sensitivity is nearly constant between 300K and 27K changing from -2.2mV/K to -1.8mV/K, and then to -64mV/K at ~8K. A voltage versus temperature graph of an SMDT diode is shown in figure [4.6].

To overcome contact resistance problems a four probe technique was used, but reversal of the current to overcome thermoelectric offset voltages was not possible. However, errors from this source were found to be small, because of the large thermal coefficients of the diode ($\simeq$-2mV/K).

For the purpose of temperature measurement the diode is operated in the

forward bias mode with the current being supplied from a constant current source (10μA to 100μA). Considerations of dynamic resistance, power dissipation (Rao et al, (1983)) and reproducibility usually dictate a current of 10μA. For simplicity a constant current source (Horowitz and Hill, (1989)) based on a 2N3819 FET and a ten-turn pot for biasing was used. The circuit has very good temporal stability and a temperature coefficient of 0.15%/K. The constant current source will last approximately one year if supplied by two PP3 batteries. Because two silicon diodes were used a Keithley 705 Scanner with a Low Voltage Scanner card switched the diode voltages individually to a Keithley 181 Nanovoltmeter for measurement. The Keithley 181 Nanovoltmeter was chosen for this measurement because of its extremely good accuracy, temperature coefficient, high input impedance (>1GΩ) and resolution of better than 10μV on the 2V range. A high input impedance instrument is necessary to achieve a 0.01% accuracy, because the static resistance of the diode at 4.2K is $\simeq$170KΩ.

4.4.2 Calibration of Diodes

A small error in the temperature can give a substantially large error in the thermopower. So the diodes were sent to Oxford University (ref. Oxford University) for a 70 point calibration over the temperature range 1.56K to 300.04K, having a reproducibility of better than 30mK (ref. Southampton University). The calibration data paid particular attention to the "knee" of the curve to reduce errors (see figure [4.6]). A polynomial given by,

$$T(x) = \sum_{N=0} A_N . x^N \tag{4.4}$$

was fitted to the voltage versus temperature measurements, where x is a normalized value given by,

$$x = \frac{(V_M - V_L) - (V_U - V_M)}{(V_U - V_L)} \tag{4.5}$$

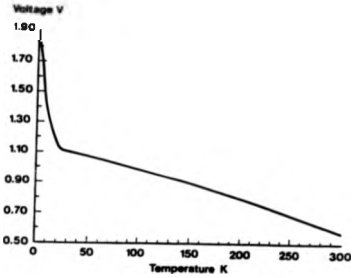

Figure 4:6 A typical plot of the voltage (for 10μA) versus temperature for a diode, shown in figure [4.5]. (ref. Southampton University — data sheet)

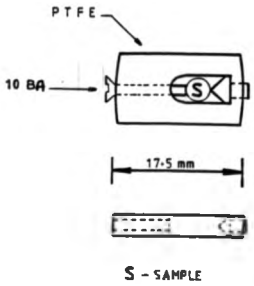

Figure 4:7 Schematic diagrams of one of the PTFE clamps used for anchoring a diode to the sample (S).

V_L and V_U are the voltage extremities of a pre–determined temperature interval and V_M is the voltage measured. To obtain the highest possible accuracy of polynomial fit the whole temperature range was broken into five sections, paying special attention to the "knee" of the curve. The intervals were as shown in Table 4.1.

Table 4.1: Polynomial Coefficients

Temperature Range	Number of Coefficients
300 – 100 K	11
100 – 40 K	8
40 – 20 K	8
20 – 10 K	10
10 – 1 K	9

These coefficients for all the silicon diodes used were incorporated in the software for computer automation.

4.5 PTFE Clamps

As the differential method of measuring the thermopower was chosen, two silicon diodes were required to be in thermal contact with the sample. For ideal temperature measurements the temperature sensor should be a point contact at the sample. Owing to the physical dimensions of the diode that was not possible, so two clamps were designed as shown in figure [4.7]. The clamps were connected to a sample as indicated in figure [4.8]. Copper potential probes (P1 and P2) make point electrical and thermal contact to the sample at two places along its length. Because the diodes were calibrated using GE7031 varnish the thermometers were therefore glued to the

probes using this brand of varnish. The varnish provides good adhesion without cracking and satisfactory thermal contact if thinned by means of a 1:1 mixture of methanol and toluene to water consistency before application. For fast thermal response the clamps were made of PTFE. A small groove was produced in the sample where the point of a probe was to go, so the clamp would not move when thermally cycled. Once the sample had been cleaned in an ultrasonic bath containing a beaker of Trichloroethane ($CH_3C.Cl_3$) solvent, indium amalgam was put into this groove to achieve good electrical contact between the copper and the sample. Under test, it was found that the thermometer mounting provided a sufficiently fast thermal response for thermopower measurements. When loading the sample into the holder, indium amalgam was put onto the parallel faces of the sample to form a good electrical and thermal contact to the copper platelets.

4.6 Thermal Anchoring

Some of the samples under investigation were expected to be highly insulating at low temperatures, e.g. $>10^{12}\Omega$.cm at $\leq$.2K, so the system was designed to have an electrical isolation greater than $10^{14}\Omega$ between all the leads in contact with sample to the cryostat. (This resistance limit was set by the electronics used). The isolation was checked using a Keithley 616 Electrometer which could measure $>200T\Omega$. Very few materials have this high resistivity specification; such materials are PTFE, alumina and sapphire.

Electrical leads travelling down the inside of the cryostat to the sample holder from the outside world carry heat. This heat can give erroneous results if not dealt with (Kopp and Slack, (1971)). In most cryogenic set-ups the electrical wires are thermally anchored to a cryogenic bath using GE7031 varnish as the adhesive (White, (1979)), in order to shunt the heat flow away from the sample. Alterna-

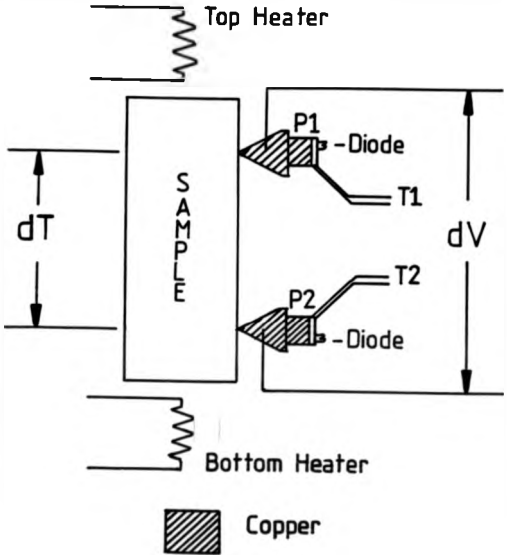

Figure 4:8 A schematic diagram showing the main details of the sample holder. P1 and P2 are the copper probes within the PTFE clamps.

tively, if a very high degree of electrical isolation from the vacuum jackets of the cryostat is required an alumina substrate is used (or similar material) as the thermally conducting medium. Ideally, the thermal anchor temperature should be as close to the sample temperature as possible to reduce the quantity of heat flow between the anchor and sample. Using liquid nitrogen, or any other cryogenic fluid, causes a large temperature gradient when the sample temperature is at 300K. For this reason, a special thermal tempering anchor (Hust, (1970)) was designed and is shown in figure [4.9]. The idea behind the design was to effectively "mix" the heat flow down the wires to the sample with the heat of the small heaters of the sample holder. Extremely good thermal contact between the wires and pieces of sapphire next to the copper platelets was essential and achieved using GE7031 varnish. A preliminary test on this design using a calibrated 30 point Rhodium/Iron resistor showed that at 4.2K the resistor and diode agreed to within their errors of calibration. For each side of the sample, three temperature tempering copper rods of 10mm diameter by 10mm in length were grouped together: first rod for the diode wires, the second for the voltage sensing wire and a third spare rod for future possible use. All three rods therefore were in thermal equilibrium and electrically isolated from each other (see figure [4.9]). This design was only possible because of the characteristics of sapphire which has good thermal conductivity at low temperatures, repels water from its surface and is an extremely good electrical isolator — $10^{16}\Omega$.cm at 300K.

Two small 40Ω constantan non-inductively wound resistance heaters were mounted on PTFE "bobbins". One of these at each end of the sample, produced the temperature gradient across the sample for the differential method of measuring the Seebeck coefficient. Using PTFE, electrically isolated the heaters from all the leads and sample (see figure [4.9]).

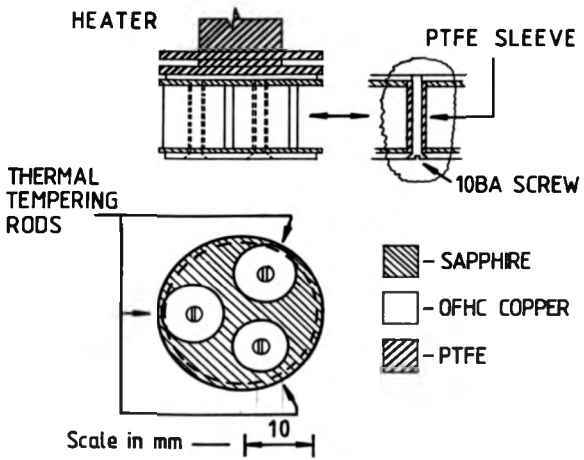

Figure 4:9 A schematic diagram of the thermal anchor used, indicating the thermal tempering rods and position of a small heater.

4.7 Cryogenic System

The cryostat consists of two German Silver tubes one inside the other and both capped at the bottom (see figure [4.10]). The inner tube housing the sample holder while the other forms a vacuum/exchange jacket separating the cryogenic fluid from the centre space. Two glass dewars one inside the other surround the above mentioned metal cans. The outer glass dewar holds liquid nitrogen acting as a radiation shield while the other dewar holds liquid helium.

For sample ambient temperature control a non-inductively wound resistance heater was mounted, using GE7031 varnish, onto an Oxygen Free High Conductivity (OFHC) copper cap which is at the end of the inner German Silver tube. A 3 point calibrated silicon diode for temperature sensing was mounted also on the copper cap to give a fast and positive response. An Oxford Instruments ITC4 temperature controller used the resistive winding and diode to control the sample ambient temperature to within 0.1K. Advantageously, the controller outputs d.c. power so introducing very little radiated noise to the sample.

The sample holder is held in a three bar cage supported by a German Silver tube. Another German Silver tube is inside this, which is connected to the top half of the sample holder. At the other end of this tube is a tensioned spring which compresses the copper platelets to the sample for good electrical and thermal contact. Three metal boxes surround the pin seals: one box for high impedance connections, another for low impedance connections and housing a constant current source for the diodes, and lastly a spare for future possible work. These metal boxes terminated the wires from the sample holder at electrical sockets. By doing this the external electronics could be disconnected from the cryostat when the sample holder needed to be removed.

A one inch pumping system using a diffusion pump, a liquid nitrogen trap

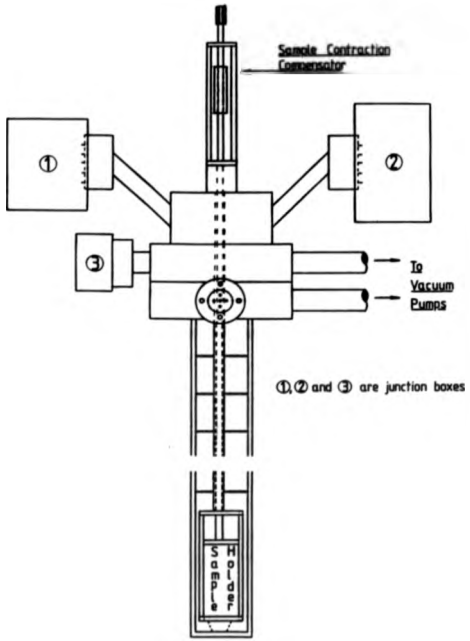

Figure 4:10 A schematic diagram of the cryostat showing the electronic junction boxes, sample contraction compensator and sample holder.

and a rotary pump produces a vacuum of $\sim 10^{-6}$ Torr in the metal chambers when required. Such a vacuum helps to reduce boil-off of liquid helium at elevated sample temperatures, but more importantly extracts moisture from the system before pre-cooling.

A rubber bladder, used for taking gas samples, filled with high grade helium gas connected to the vacuum system via a needle valve allowed for exchange gas to be transferred to the cryostat.

4.8 Electronics

Keem (1975) used Varactor Bridge Operational Amplifiers (Analog Device 311K) that have a high input impedance of $10^{14}\Omega$ in the non-inverting mode for measurements of thermopower and resistivity (see figure [4.11] and figure [4.12] for the experimental configurations). Other specifications include low bias current of ± 10fA, low drift with time ($\pm 100\mu$V/month) and low voltage noise (10μV peak-to-peak) in the bandwidth 0.01Hz-1Hz. The electronics used for this research project is based round the AD311K op amp, because at the time of construction a better or alternative op amp was not found on the commercial market that could be used to measure such high resistances and be relatively cheap. The electronics described in sections 4.8.1 and 4.8.2 is simpler than Keem's circuit (1975) because the computer software and Keithley products now available replace the computational electronics employed by him.

For this AD311K op amp the bandwidth was reduced in order to minimize noise. To obtain the required bandwidth it was necessary to have a low pass filter on the output of the op amp constructed with a time constant of 1 second.

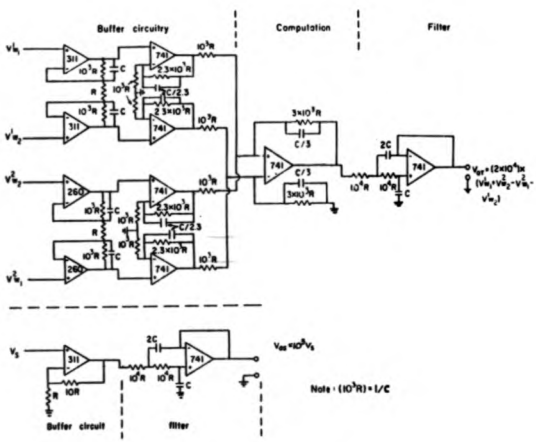

Figure 4:11 The electronics used by Keem (1975) for thermopower and resistivity measurements.

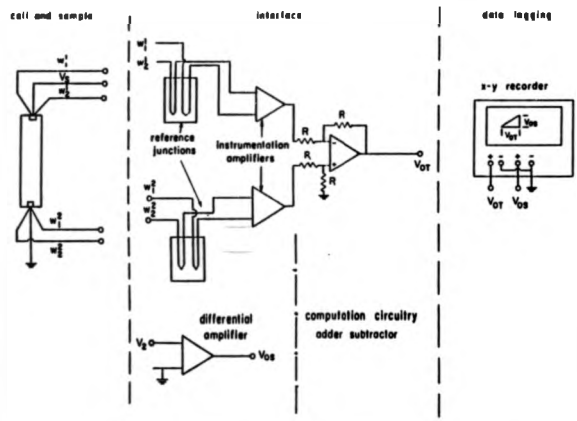

Figure 4:12 The experimental configurations used by Keem (1975) for measuring the thermopower and resistivity.

4.8.1 Thermopower Circuits

For thermopower measurements two separate configurations were developed for different source resistances, taking full advantage of the cryostats design to be able to interchange circuits (see section 4.7). When the source resistance at low temperatures became >100MΩ the AD311K op amp was used. For lower impedances an RS7650 op amp was used that had almost ideal specifications which included a voltage noise of 2μV peak–to–peak, an input impedance of $10^{12}\Omega$ and a bias current of 0.5pA. The RS7650 op amp was compared with a Keithley 181 Nanovoltmeter for a thermopower measurement and were found to agree within the experimental error.

Because a single op amp was used for this measurement one end of the sample was connected to battery common as shown in figure [4.13], instead of at the bottom–most part of the sample. A Keithley 181 Nanovoltmeter measured the signal voltages from the output of the op amps.

4.8.2 Resistivity Circuit

Two AD311K op amps were used for the resistance measurement which did not need such stringent conditions as that for thermopower, because the voltages involved were large compared with the noise voltages. For reasons of grounding, a differential op amp circuit was connected to the output of the two AD311K op amps (see figure [4.14]). A Keithley 195A DMM measured the differential output and when the signal started to become excessively noisy the Keithley 195A was configured to average several voltage measurements, therefore reducing the error.

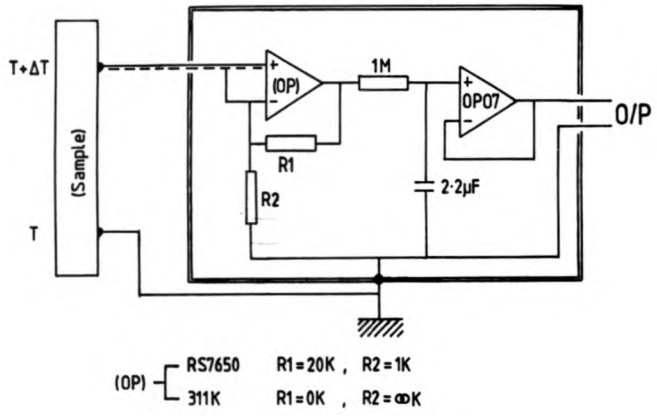

Figure 4:13 The electronics used by the present author for measuring the thermopower using the differential method.

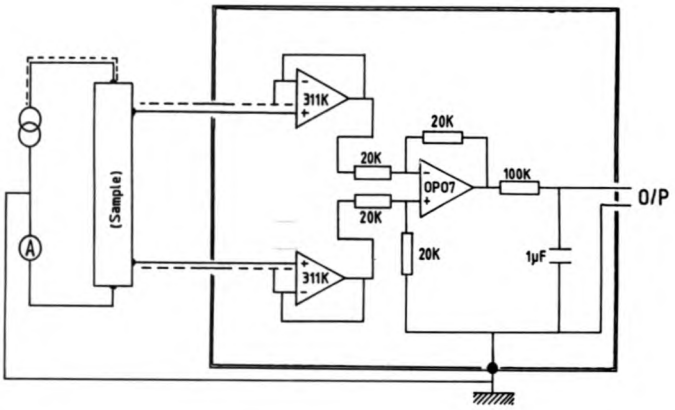

Figure 4:14 The electronics used by the present author for measuring the resistivity.

4.9 Driven Shields

To reduce leakage currents and RC time constants, rigid driven shields (Horowitz and Hill, (1989)) were implemented in the cryostat. Two shields were provided for the voltage sensing wires and one for the current when doing resistivity measurements. So that the driven shields terminated as close to the sample as possible a special pin seal was made. Each pin was made from alumina with a metal seal as shown in figure [4.15]. Because the central wires pass through the pins a soft adhesive, applied using a soldering iron, was used to form a vacuum seal.

4.10 Software

For total automation a Hewlett Packard 86B computer controlled, using "in house" developed software, all the electronic peripherals via the IEEE interface except for the Oxford Instrument's ITC4 Temperature Controller which used the RS232 interface. A block diagram of the instruments used is given in figure [4.16]. The Keithleys 220 and 175 are a Constant Current source and Picoammeter respectively, which were used for resistivity measurements.

All the data taken were "dumped" to on-line disc drives and a printer for a hard copy.

4.10.1 Thermopower Software

The most critical element of the software, was for producing the required series of temperature gradients across the sample. This was achieved by using a software PID (Proportional-Integral-Differential) routine to control each small heater (see section 4.10.3). Once the PID values were experimentally found a stability of ± 15mK was not uncommon as indicated by the temperature sensor. The voltages of the two

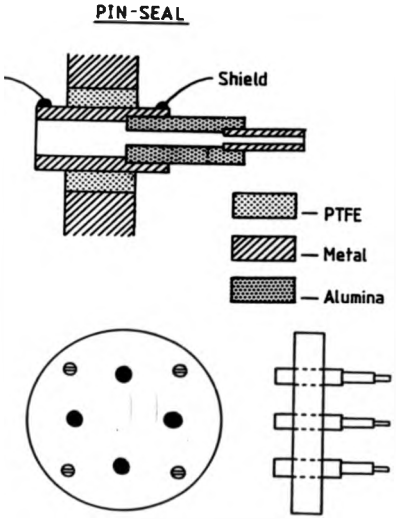

Figure 4:15 A schematic diagram of the pin–seal used. Designed by the present author so that driven shields could be used within the cryostat.

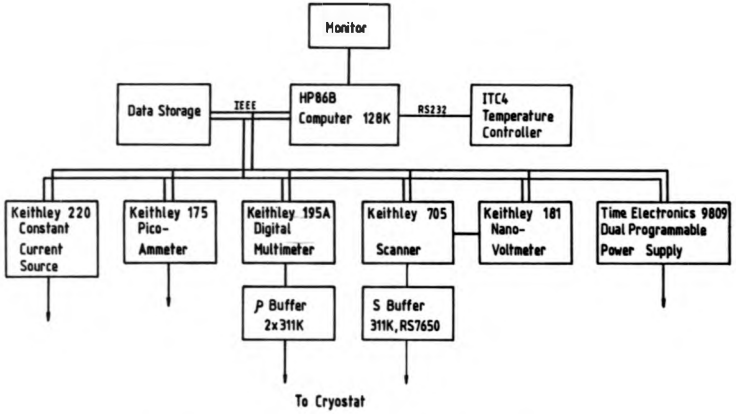

Figure 4:16 A block diagram showing the major pieces of electronics used, which are interfaced to a Hewlett Packard computer for automation.

diodes were measured sequentially, their respective temperatures calculated using polynomials (see section 4.4.2) and these values put into the PID equations. The results of the expressions gave values to send to a dual programmable power supply to alter the heaters. Switching between the diodes of once every second was found to be adequate.

A flow chart of the "in house" software for thermopower measurements is shown in figure [4.17].

For the differential thermopower measurement ($\Delta V/\Delta T$) any number of points from 3 to 7 points can be used for calculating the Seebeck coefficient, the number depends on the time available and accuracy required. Five points were felt to be adequate for this system with their mean temperatures being the same to within 10% of the largest temperature gradient. Once a certain temperature gradient across the sample had been produced the thermoelectric voltage was measured by the buffered Keithley 181 Nanovoltmeter and stored in the computer memory. Then the temperature gradient across the sample was altered for the next point. After all the five points had been measured the Seebeck coefficient, correlation coefficient, error percentage etc. were calculated and all the data sent to a printer and disc drive. By calculating these coefficients through the temperature run any anomalies — the Verwey transition for example — would immediately show and appropriate action could be taken.

4.10.2 Resistivity Software

For the resistance measurement a zero temperature gradient was needed across the sample. Once achieved, using PID control for both small heaters, the temperature was measured before and after the resistance measurement to check for drift. A current was passed through the sample using a Keithley 220 Constant Current

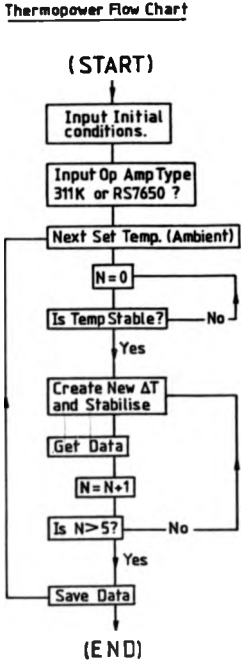

Figure 4:17 A flow chart showing the main features of the software for automation.

source. To reduce errors the current was auto-ranged using computer software until the pre-set volt limit on the Keithley 220 Constant Current source was reached. When the largest current was found it was split so that five in total different currents in the forward and reverse direction could then be sent through the sample. Their respective voltages were read from the AD311K op amps by the Keithley 195A DMM and the data analysed by the computer and stored for later use. At all times the power dissipation was <1mW. A flow chart of the program is shown in figure [4.18].

When the final measurement for resistivity or thermopower had been taken, the next ambient temperature set-point value was sent to the Oxford Instruments ITC4 Temperature Controller. The sample temperature was read by one of the silicon diodes. When stable, the next set of measurements would then be taken.

This method of control was continued until all the measurements had been taken.

4.10.3 PID Control

This section only intends to give a synopsis of three term temperature control because many books have been published on this subject.

Temperature controllers use complex mathematical algorithms to achieve good temperature stability and fast response to the set temperature. The technique used here for the three term PID control is very basic but the principle still holds. Each term of the PID control is dealt with individually and the result of each calculation accumulated to produce a single number interpreted as the power output.

For proportional control, power is delivered to the heater that is proportional to the set temperature minus the measured temperature. Hence,

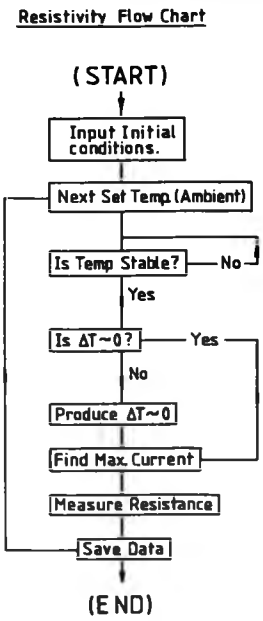

Figure 4:18 A flow chart showing the main features of the software for automation.

$$P_{Pro} = K_P(T_S - T_M)$$

where T_S is the set temperature,

T_M is the measured temperature

and K_P is the proportionality constant. If K_P is large then the expression reduces to an on–off control. If K_P is not too large then the temperature will remain, after steady state, ΔT below the set temperature because of heat losses. This ΔT can be reduced by increasing K_P but this can lead to an on–off situation. Consequently, another term is required.

Integral control increases the output power by a proportional amount given by the set temperature minus the measured temperature, similar to the above proportional control. But unlike proportional control this result is added to all the previous calculated values:

$$P_{Int(N)} = P_{Int(N-1)} + K_I(T_S - T_M)$$

where $P_{Int(N-1)}$ is the latest incremental power output,

$P_{Int(N)}$ is the "up–to–date" power output,

and K_I is a proportionality constant. When the constant (K_I) of proportionality has been experimentally found the measured temperature should be stable about the set temperature once time has been given for the system to settle.

Differential control calculates the gradient of the temperature versus time curve and gives an output proportional to this. It only takes effect when the temperature sensor see's a sudden temperature change — like opening of a furnace door — and delivers power quickly to overcome the losses. Because this situation is rare in cryogenic systems, differential control tends not to be used. For this very reason the differential term was put to zero.

The basic mathematical expression for three term PID control is therefore as follows:–

$$P_{OUT} = P_{Pro} + P_{Int} + P_{Diff}.$$

4.11 Test Results and Conclusion

The test results obtained using the above apparatus of magnetite and "pure" nickel are shown in figures [5.3–5.4] and reported in "The Journal of Scientific Instruments", (Phillips et al, (1989)). The vast majority of thermopower measurements have in the past used thermocouples for temperature measurements and for the first time silicon diodes have been used here giving good results.

Chapter 5

RESULTS AND DISCUSSION

5.1 Introduction

Because the apparatus was designed, built and tested "in house" a few standard samples were analysed before commencing measurements on single crystal zinc and manganese ferrites. The results show that the investigations using this apparatus plus electronics (explained in section 5.2), can reproduce accurately data previously obtained by past authors. Electrical conductivity and thermopower measurements on zinc ferrite ($Zn_XFe_{3-X}O_4$) and manganese ferrite ($Mn_XFe_{3-X}O_4$) with $0 \leq X \leq 1$ over the temperature range 4.2K-300K are then presented. The gross features of the results are outlined and then detailed analysis of the data from the zinc and manganese systems is made in terms of current theories.

5.2 Reasons for Present Work

By increasing the accuracy and reducing noise on the data at the lowest temperatures, behaviours such as $\Theta \propto T^{1/2}$ and $\sigma \propto T^{S}$ (see sections 2.2.5 and 2.3.5) should be more easily observed. However, these two ferrite systems do have their compli-

cations:

I) Zinc ferrite when being produced evaporates zinc oxide from the sample surface unlike that of manganese ferrite where loss of manganese is not encountered (see section 4.2.1). Sample preparation and surface analysis was essential.

II) At low temperatures for high values of zinc concentration ($X \geq 0.8$), magnetic disorder (at the Néel temperature, T_N) could have an effect on the results (Tinsley, (1975). See Table 5.3.).

III) Although manganese has an A-site preference (see Chapter 3) a small proportion of the cations are effectively "frozen" in on the octahedral sites and this could influence the conduction process.

By comparing these two ferrite systems with each other and those discussed in Chapter 3, a better understanding of the conduction processes in spinel ferrites is hoped to be obtained.

5.3 Calibration of Apparatus

Yeung (1982) measured the electrical conductivity and thermopower of nickel ferrites with $0 \leq X < 1$ over the temperature range 10K-1200K. The ionic formula for nickel substitutions is:

$$\text{Nickel} \quad [Fe^{3+}]_A[Ni_X^{2+}Fe_{1-X}^{2+}Fe^{3+}]_B O_4^{2-} \tag{5.1}$$

and for zinc and manganese ferrite:

$$\text{Zinc} \quad [Zn_X^{2+}Fe_{1-X}^{3+}]_A[Fe_{1-X}^{2+}Fe_{1+X}^{3+}]_B O_4^{2-} \tag{5.2}$$

$$\text{Manganese} \quad [Mn_X^{2+}Fe_{1-X}^{3+}]_A[Fe_{1-X}^{2+}Fe_{1+X}^{3+}]_B O_4^{2-} \tag{5.3}$$

with $0 \leq X \leq 1$.

To show that the new experimental apparatus designed was sensitive to the potentially subtle features associated with electrical changes within the samples measured — if any — electrical conductivity measurements were made upon similar nickel ferrites with $0 \leq X \leq 0.2$; for high impedance measurements, X=0.8 was chosen to compare with Yeung's X=0.9 nickel ferrite. The G-Factor (see equations (5.5) and (5.11)), which is believed to be sensitive to the effects of electron–electron interactions, is calculated for these measured ferrites. As can be seen in figure [5.1] the graphs for $0 \leq X \leq 0.2$ compare favourably with Yeung's X=0.1 data. The pronounced peaks are associated with the Verwey transition (Verwey, (1939)). Figure [5.2] shows plots of the G-Factor data for nickel ferrite with X=0.8 and X=0.9 against temperature, there is good agreement considering the difference in the value of X. It is worth noting here that in the previous and present work the Verwey transition, as indicated by the peak, is completely suppressed for X=0.2.

Because the apparatus with electronics is a new design and thermopower measurements are more difficult to make compared to electrical conductivity measurements, owing to the very small thermal voltages involved and the need to monitor temperature gradients, more samples have been tested. Magnetite (Fe_3O_4) was chosen as a **standard** for testing the apparatus because it is the building block of all spinel ferrites and pure nickel metal because of the reliability of the data on it. Graphs of the data obtained are shown in figures [5.3–5.4]. The plots indicate good agreement with previous author's measurements (Grieg and Harrison (1965), Blatt et al (1967), Whall et al (1986)). To extend this thermopower calibration further, nickel ferrites with X=0.2 and X=0.8 were measured. The data are shown in figure [5.5]. These plots compare X=0.8 with data of concentration X=0.9 obtained by Griffiths et al (1970) and X=0.2 with Yeung's X=0.2 nickel concentration. The rate of change with temperature of the curve for Griffith's X=0.9 is very similar to that

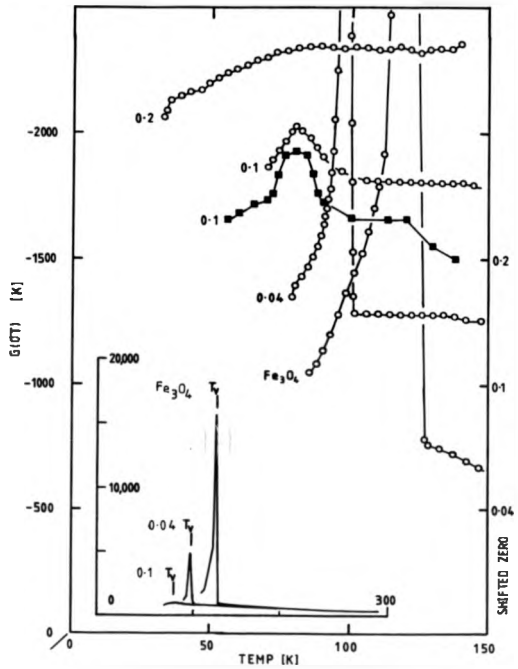

Figure 5:1 A plot of G(σT) versus temperature for $Ni_XFe_{3-X}O_4$ with X$\leq$0.2. The Verwey transitions, T_V, are clearly shown; o: present author; ■: Yeung, (1982).

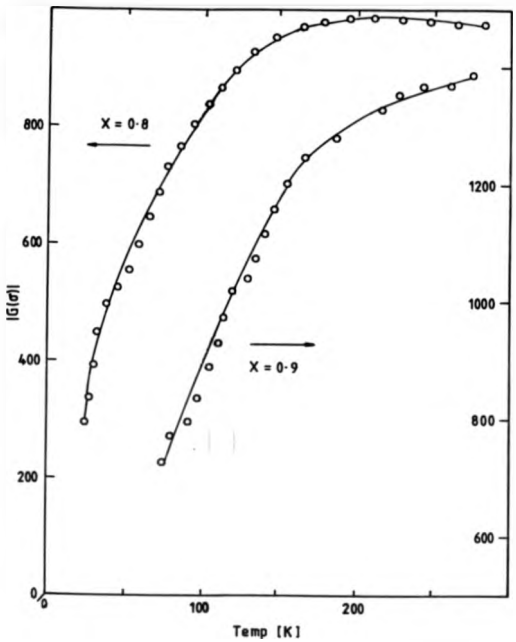

Figure 5:2 The G–factor of $Ni_XFe_{3-X}O_4$ versus temperature; X=0.8 — present author, X=0.9 — Yeung (1982).

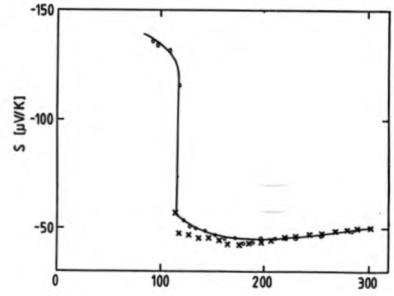

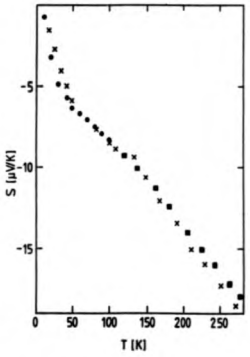

Figure 5:3 The thermopower of magnetite versus temperature. o: present author used silicon diodes as the temperature sensors, ×: Whall et al (1986) used thermocouples.

Figure 5:4 Thermopower of pure Nickel metal versus temperature; ×: present author; ■: Blatt et al, (1967); •: Grieg and Harrison, (1965).

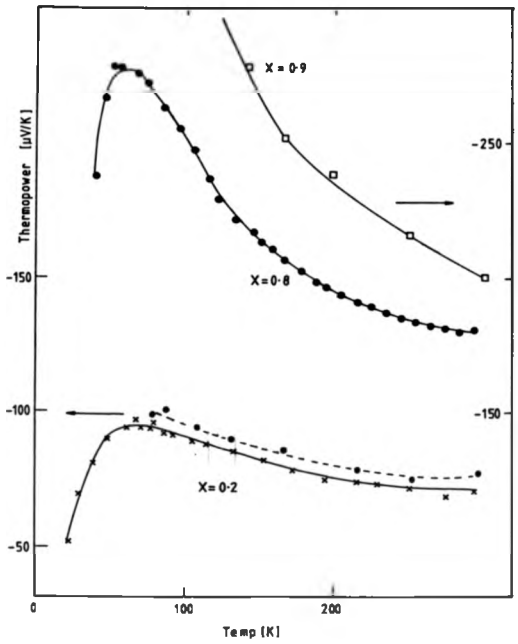

Figure 5:5 $Ni_XFe_{3-X}O_4$ thermopower data plotted against temperature; •: present author; ×: Whall et al, (1986); □: Griffiths et al, (1970).

of the present author's X=0.8, while the data plots for nickel concentration X=0.2 are nearly identical.

5.4 Outline of Thermopower and Electrical Conductivity Results

The logarithm of the conductivity ($Log_{10}\sigma$), for various manganese and zinc ferrites, is plotted versus reciprocal temperature (100/T) for the temperature range 7.7K–300K in figures [5.6–5.9]. As can be easily observed, the behaviour is non–linear i.e. the slopes of the curves vary with temperature.

For both zinc and manganese ferrites the resistivity at room temperature increases with increasing X (see equations (5.1) and (5.2) for ionic formulae). At lower temperatures (T<50K) the opposite occurs for manganese ferrite — the resistivity, at constant temperature, gradually falls for increasing X. Zinc ferrite is similar to manganese at low temperatures until X>0.6 where the resistivity begins to increase again.

For low values of X there is no indication of a Verwey transition for both manganese and zinc ferrite except when X=0. This shows that the metal–insulator transition is small or completely suppressed for $X \geq 0.1$, which supports Miyahara's (1972) work. However, the data can be treated so that it is more sensitive to such features — see section 5.5.

The thermopower results for zinc and manganese are plotted versus temperature and are shown in figures [5.10–5.12]. The absolute Seebeck coefficients of both ferrite systems increase with increasing X at all temperatures. A peak is observed at approximately 70K (T_S) where the plots then fall towards zero with decreasing temperature and gently fall with increasing temperature.

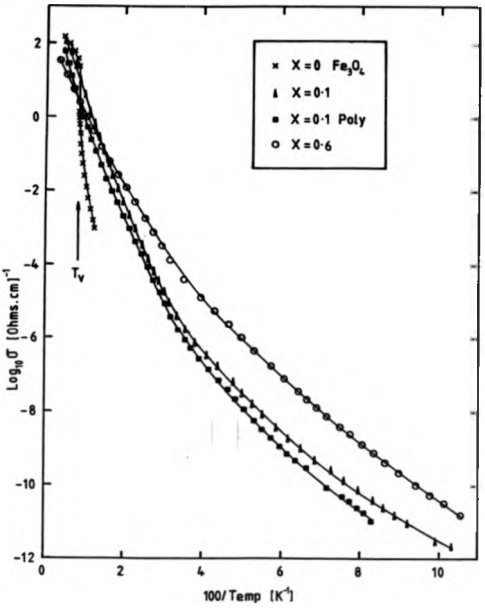

Figure 5:6 Plot of $Log_{10}\sigma$ versus 100/Temp for $Zn_xFe_{3-x}O_4$.

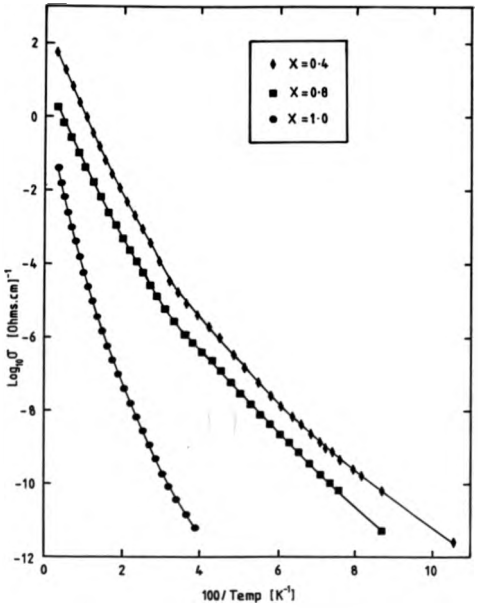

Figure 5:7 Plot of $Log_{10}\sigma$ versus 100/Temp for $Zn_XFe_{3-X}O_4$.

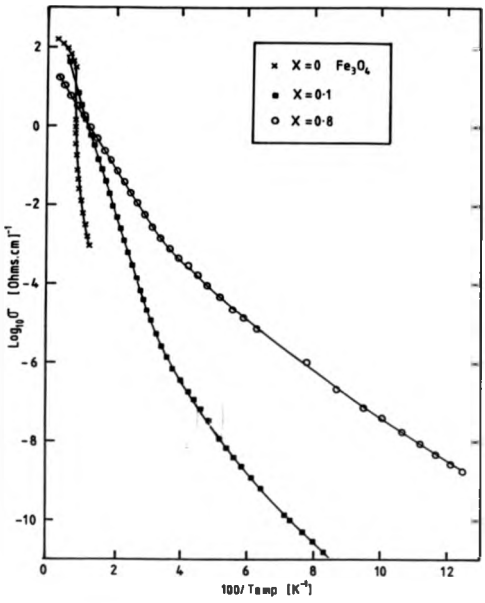

Figure 5:8 Plot of $Log_{10}\sigma$ versus 100/Temp for $Mn_xFe_{3-x}O_4$.

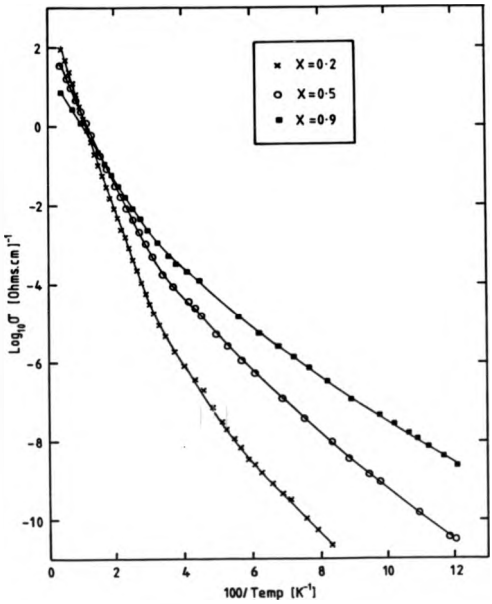

Figure 5:9 Plot of $Log_{10}\sigma$ versus 100/Temp for $Mn_XFe_{3-x}O_4$.

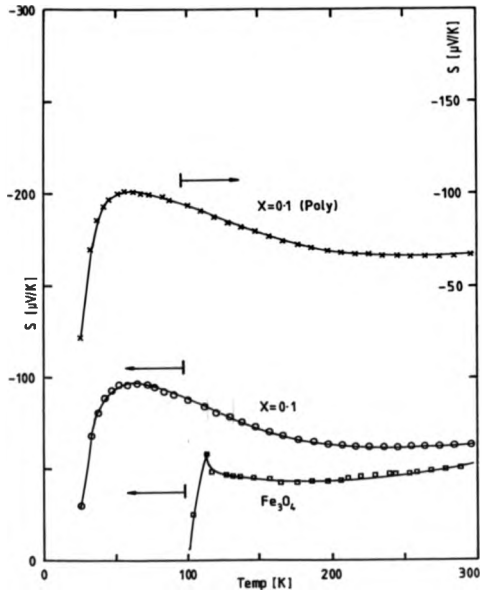

Figure 5:10 The thermopower of $Zn_xFe_{3-x}O_4$ with $X \leq 0.1$ plotted against temperature.

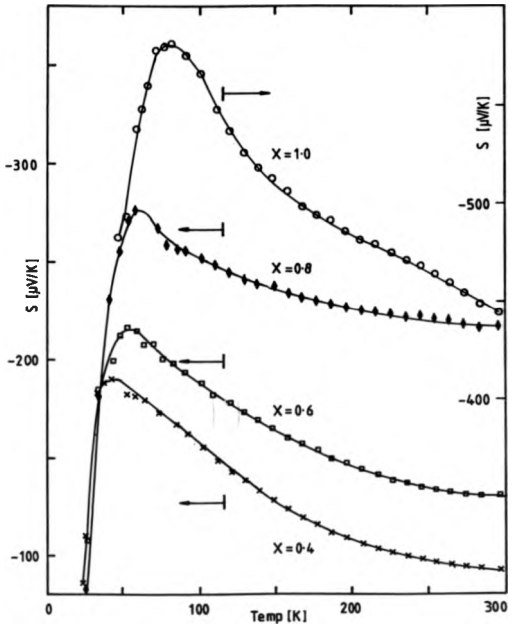

Figure 5:11 The thermopower of $Zn_xFe_{3-x}O_4$ with X>0.1 plotted against temperature.

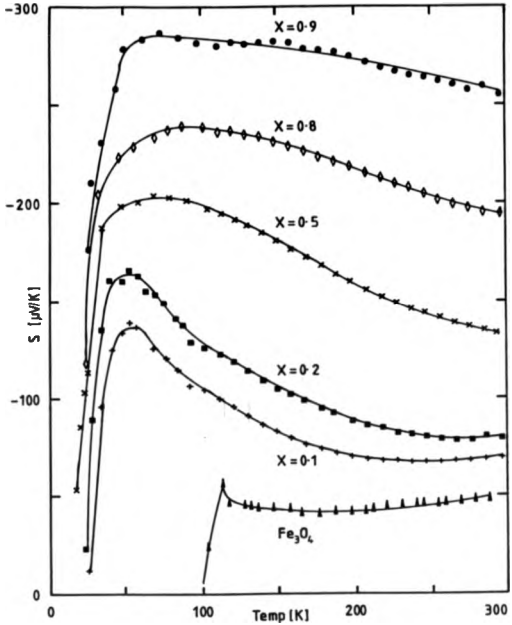

Figure 5:12 The thermopower of $Mn_XFe_{3-X}O_4$ with $0 \leq X < 1$ plotted against temperature.

It is worth noting here that the thermopower data for different manganese ferrite compositions do not overlap in contrast to earlier results of Simsa and Brabers (1988) (see figure [3.13]): Salerno (1986) did not observe this feature either (see figure [3.15]). The present author can only surmise that Simsa and Brabers measured a bad sample batch.

5.5 Analysis of the Electrical Conductivity Results

Whall et al (1986) have argued that ferrite systems (see Chapter 3), in particular nickel ferrites, have a conduction process which can be described by Miller-Abrahams (1960) theory. The model they have adopted for Fe_3O_4 is a band of Anderson localized states having a "natural" random potential distribution for $T>T_V$ due to electron–electron interactions.

When zinc or manganese is added to the spinel sample the ions go onto the A–sites (Verwey and Heilmann (1947), Lotgering (1964)). Unlike that of nickel ferrite where the disorder occurs on the B–sites (Whall et al, (1986)), the disorder is on the A–sites for zinc and manganese ferrite. Hence, substitution on the tetrahedral site causes increasing disorder (as measured by the standard deviation of the number of nearest neighbour impurity ions) for increasing X until at X=0.5 where the random potential peaks and then falls to zero for increasing X i.e. becoming more ordered. For nickel ferrite, the random potential disorder increases for increasing X and becomes a maximum for X=1.

Because the adiabatic small polaron model (Austin and Mott, (1969)), Miller-Abrahams (1960) and Ihle–Lorenz (1975) theories all predict a T^{-1} pre–exponential

dependence then the conductivity is assumed to be of the form:-

$$\sigma \propto T^{-1}\mathrm{EXP}(-W/kT) \tag{5.4}$$

where W is the activation energy. Figures [5.6–5.9] do not show any dramatic changes in the conductivity except for magnetite. A more sensitive approach used by Whall et al (1986) is to calculate

$$G(\sigma T) = -\frac{\mathrm{dLn}(\sigma T)}{d(1/T)} = -\frac{W}{k} + \frac{T}{k}\frac{dW}{dT} \tag{5.5}$$

When the activation energy is approximately constant, then the first term of equation (5.5) is the most important. When in the vicinity of the Verwey transition or the Néel point, where the activation energy changes quickly with respect to temperature, then the second term of equation (5.5) is the most dominant. The graphs of $G(\sigma T)$ are shown in figures [5.13–5.14] for both manganese and zinc ferrite.

For completeness the G-Factor has been calculated for zinc and manganese ferrite with a $T^{-3/2}$ pre-exponential. Such a result is expected for polaron hopping in the absence of a Coulomb Gap (Emin, (1973)). As can be seen in figures [5.15–5.16] the salient features are approximately the same as those in figures [5.13–5.14].

As a simplification, small polaron effects are assumed not to play a major role in the conduction processes considered here for the following reasons:-

I) Austin and Mott (1969) discuss the nearest-neighbour separation and predict a reduction in the polaron binding energy due to overlapping polarization clouds.

II) Mott (1974) has argued that for high concentrations of carriers the polaron binding energy will be small if there are more than 0.1 carriers per site: for manganese and zinc ferrite this occurs when $X \geq 0.8$.

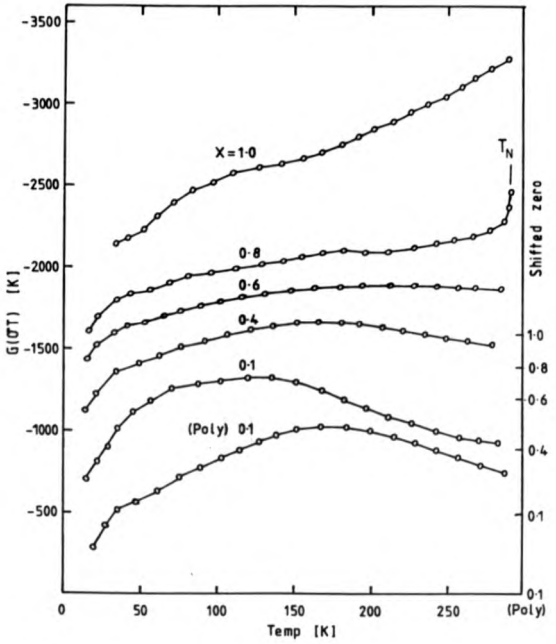

Figure 5:13 $G(\sigma T)$ $[dLn(\sigma T)/d(1/T)]$ of $Zn_XFe_{3-X}O_4$ with $0 \leq X \leq 1$ plotted against temperature. Each plot has a shifted origin, which is indicated on the right–hand side. The sharp rise on the $Zn_{0.8}Fe_{2.2}O_4$ plot is interpreted as being due to the onset of magnetic disorder at the Néel point, T_N.

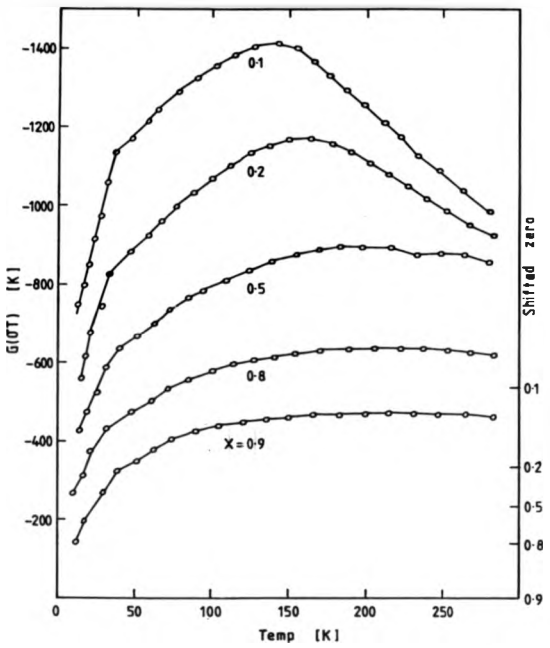

Figure 5:14 $G(\sigma T)$ $[dLn(\sigma T)/d(1/T)]$ of $Mn_XFe_{3-X}O_4$ with $0 \leq X < 1$ plotted against temperature. Each plot has a shifted origin, which is indicated on the right–hand side.

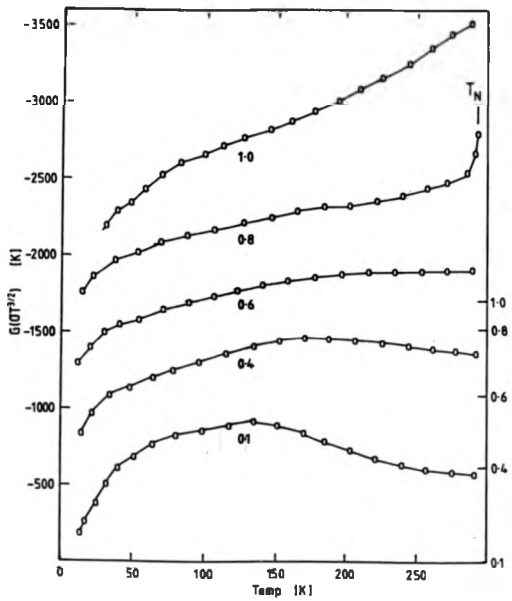

Figure 5:15 $G(\sigma T^{3/2})\,[d\mathrm{Ln}(\sigma T^{3/2})/d(1/T)]$ of $Zn_XFe_{3-X}O_4$ with $0 \leq X \leq 1$ plotted against temperature. Each plot has a shifted origin, which is indicated on the right–hand side. The sharp rise on the $Zn_{0.8}Fe_{2.2}O_4$ plot is interpreted as being due to the onset of magnetic disorder at the Néel point, T_N.

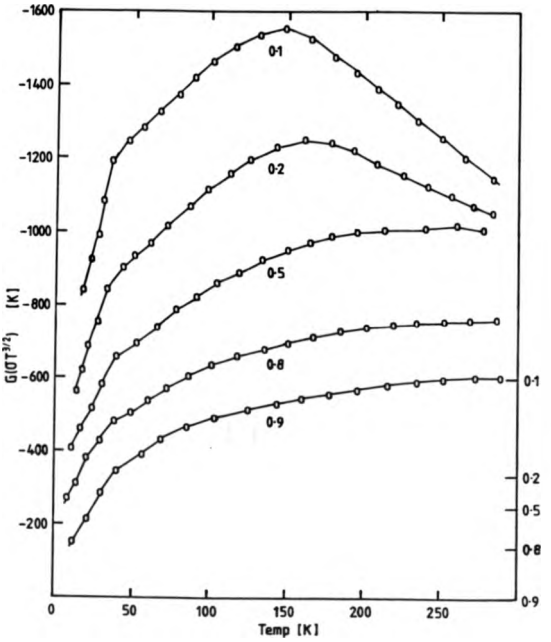

Figure 5:16 $G(\sigma T^{3/2})\,[dLn(\sigma T^{3/2})/d(1/T)]$ of $Mn_XFe_{3-X}O_4$ with $0 \leq X < 1$ plotted against temperature. Each plot has a shifted origin, which is indicated on the right-hand side.

III) Magnetite at room temperature has a relatively high mobility ($0.1 \rightarrow 1 cm^2V^{-1}s^{-1}$). Following Emin (1975) it is expected that the small polaron activation energy will be small for such a high mobility because of the lattice memory effects which give rise to correlated hopping of carriers.

IV) From specific heat measurements Gronvold and Sveen (1974) find the Debye temperature T_D for this series of compounds to be ~600K. Ihle (1984) finds the largest electron-phonon coupling constant for Fe_3O_4 to be at temperature $\hbar\omega_0/k$=816K. Therefore, at temperatures below 300K $T \ll T_D < \hbar\omega_0/k$: Emin (1974, 1975) finds for such conditions that the polaron hopping rates for both optical- and acoustic phonon assisted hopping are similar to the single phonon hopping rates (Miller and Abrahams, (1960)).

The first point to notice in figures [5.13-5.14] is that there is no Verwey transition, as defined by a **sharp** peak in the G-Factor, observed in any of the samples unlike the case of nickel ferrite (see figure [5.1]). Therefore T_V must be suppressed for $X<0.1$. This is not surprising because Miyahara (1972) observed a rapid drop in the change in conductivity at the Verwey transition when the zinc content was $X<0.04$. (The author has made some measurements on germanium ferrites (Barlow and Phillips, (1987)) and this system also shows that the Verwey transition is suppressed for $X<0.1$).

Both manganese and zinc ferrite $G(\sigma T)$ data show a peak for low values of X whilst for higher values of X the peak is not so well defined — if it exists at all. But all plots show for lowering in temperatures a fall in $G(\sigma T)$. For ease of interpretation of the data, the temperature T_G at which this fall in $G(\sigma T)$ occurs is used as a division between low and high temperatures. It is proposed that the gross

features of the data may be explained as follows:-

For values of X≤0.4 — It is expected that coulomb interactions will occur due to the large number of electrons on the B-sites. Thus, as the temperature is lowered the electrons become more ordered, hence increasing the activation energy necessary for hopping conduction. This is indicated in figures [5.13–5.14] by the increase in $G(\sigma T)$ over the temperature range 300K – T_G. (The effect of electron ordering on the density of states as the temperature is varied is shown in figure [2.8]). Then, at even lower temperatures the activation energy begins to fall, which is possibly due to many-electron hopping occurring ($\sigma \propto T^5$, see section 5.5.2).

For values of X>0.4 — The absence of the peak in the G-factor over the temperature range T_G – 300K indicates that electron-electron interaction effects have been suppressed by the substitutional disorder. Therefore, nearest-neighbour hopping is believed to be occurring. At lower temperatures, the energy for phonon assisted hopping will reduce and the energy width of the conducting layer will be small enough so that conduction will take place by variable-range hopping in a band having a constant density of states (Mott and Davis, (1979)). Consequently, at low temperatures the conductivity is expected to obey a $T^{-1/4}$ law.

All the details mentioned here will be dealt in more depth in the following sections.

At this point it is worth comparing the G-factor features of both single crystal and polycrystalline zinc X=0.1, which are shown in figure [5.13]. At low temperatures (<100K) the activation energies are approximately the same. At ~100K the single crystal activation energy produces a plateau and then falls off with increasing temperature. The polycrystalline sample also has a plateau but at ~200K, and then its activation energy falls also. Consequently, there is a large difference in the activation energies at T>100K due only to sample type — possibly due to grain boundaries. Therefore, to analyse a ferrite system in detail the samples **must**

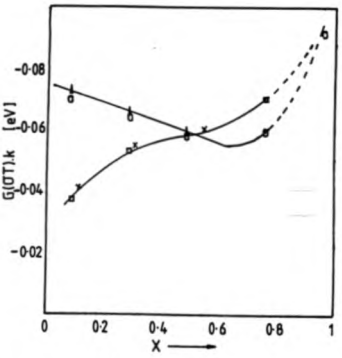

Figure 5:17 Values of $G(\sigma T).k$ versus X for $Zn_XFe_{3-X}O_4$ at different temperatures; T=150K: o; T=290K: □; T_C: ▲. Gillot et al (1981) data at 290K: ×.

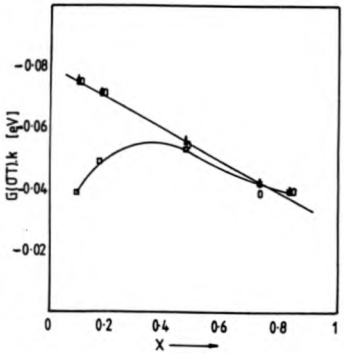

Figure 5:18 Values of $G(\sigma T).k$ versus X for $Mn_XFe_{3-X}O_4$ at different temperatures; T=150K: o; T=290K: □; T_C: ▲.

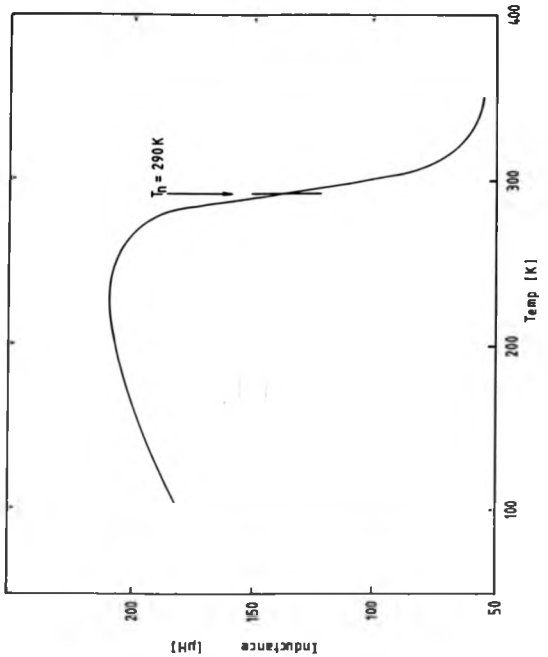

Figure 5:19 The measured inductance of $Zn_{0.8}Fe_{2.2}O_4$ versus temperature. The temperature at which dI/dT is the largest is taken as the Néel temperature.

preferably be single crystal. However, figure [5.10] shows no significant difference between the thermopowers for X=0.1.

5.5.1 High Temperatures — $T > T_G$

The $G(\sigma T).k$ values for manganese and zinc ferrite at temperatures 290K, 150K and T_G are plotted versus X in figures [5.17-5.18]. For easier interpretation the manganese ferrite data will be discussed followed by the zinc ferrite data. For manganese ferrite at T=290K, $G(\sigma T).k$ passes through a peak at X$\sim$0.4. At 150K and T_G the $G(\sigma T).k$ data for X>0.4 coincides with data at T=290K. But, for X<0.4 $G(\sigma T).k$ increases and is believed to be due to activation across the Coulomb Gap. Therefore, at T=290K the Coulomb Gap must be suppressed. So the $G(\sigma T).k$ data plot at T=290K for all X indicates nearest neighbour hopping and the peak possibly caused by disorder on the A sites (see section 5.6.2). The $G(\sigma T).k$ data for zinc ferrite for X<0.5 is similar to manganese ferrite data. For X>0.5 $G(\sigma T).k$ increases with X. The increase in $G(\sigma T).k$ for $ZnFe_2O_4$ is expected (see earlier). At 290K the $G(\sigma T).k$ for $Zn_{0.8}Fe_{2.2}O_4$ maybe due to influence of magnetic ordering/disordering when near the Néel temperature — see figure [5.13]. It is possible that at 150K the magnetic disorder may also influence the $G(\sigma T).k$ for $Zn_{0.8}Fe_{2.2}O_4$. Whall et al (1987) have interpreted the Néel point anomaly as a rapid change in the activation energy with temperature i.e. $dW/dT \gg 0$ in equation (5.5). The Néel temperature was confirmed by making inductance measurements on the sample over the temperature range 100K-350K, shown in figure [5.19]. The Neel temperature was taken at the point where the rate of change in the gradient was a maximum.

Figure [5.17] also shows the activation energies of zinc ferrite obtained by Gillot et al (1981), which show good agreement.

In the nearest neighbour hopping regime the conductivity activation energy

is given by (Jones and Schaich (1972), Zvyagin (1973)),

$$W = \frac{\int N(E)|E - E_f|.dE}{\int N(E).dE} \tag{5.6}$$

The Fermi level can be calculated using (Roberts and Schmidlin (1983), Whall et al (1984)),

$$c = \frac{\int^{E_f} N(E).dE}{\int N(E).dE} \tag{5.7}$$

and by assuming that the density of states has the Gaussian form,

$$N(E) = \frac{N_0 EXP(-E^2/2b^2)}{b\sqrt{2\pi}} \tag{5.8}$$

where b is the standard deviation and N_0 the concentration of sites. Using equations (5.7) and (5.8) the ratio $E_{f(O)}/b$ can be calculated. It should then be possible to calculate the width of the band B=2b by ignoring a possible polaron contribution to W and writing $W=k.G(\sigma T)$. Unfortunately, the second approximation is only correct if E_f is slowly varying with temperature which is not true at high temperatures and/or high X, when the electron gas has non degenerate behaviour. The analysis of the thermopower, section 5.6, will be used to throw more light on this problem.

5.5.2 Low Temperatures — $T<T_G$

Variable-Range Hopping — $X \geq 0.4$

Many authors (Simsa et al (1988) for instance) working in the field of hopping, plot their data to a known power law and see how close the fit is. The present author thinks that this is unwise as it assumes that a particular power law is obeyed. So as not to force fit the data to a pre-determined power law a more, but not completely, general equation is assumed. Following (Hill, (1976)):

$$\sigma = AT^{-M}.\mathrm{EXP}[-(T_0/T)^N] \tag{5.9}$$

where T_0 is given by equation (2.21). By differentiating with respect to (1/T) the power N can be extracted, thus:

$$G(\sigma) = \frac{d\mathrm{Ln}(\sigma)}{d(1/T)} = M.T - N.T_0^N.\left[\frac{1}{T}\right]^{N-1} \tag{5.10}$$

Making the assumption that T_0 is large (Zvyagin (1973) and Mott (1979) give $T_0 \gg 10^4$K) and dealing with low temperatures, then:

$$\mid G(\sigma) \mid = N.T_0^N.\left[\frac{1}{T}\right]^{N-1} \tag{5.11}$$

Thus,

$$\mathrm{Ln} \mid G(\sigma) \mid = \mathrm{Ln}(N.T_0^N) + (1-N).\mathrm{Ln}(T) \tag{5.12}$$

Therefore, if a power law exists (i.e. N is constant) within the temperature range of interest, a straight line will be obtained that has a gradient of $(1-N)$. Plots of Ln|G(σ)| versus Ln(T) are shown in figures [5.20-5.21] for manganese and zinc ferrite where a straight line is indeed observed at low temperatures. For high values of X (i.e. $X \geq 0.4$) the measured slope is 3/4, corresponding to a $T^{1/4}$ law, whereas

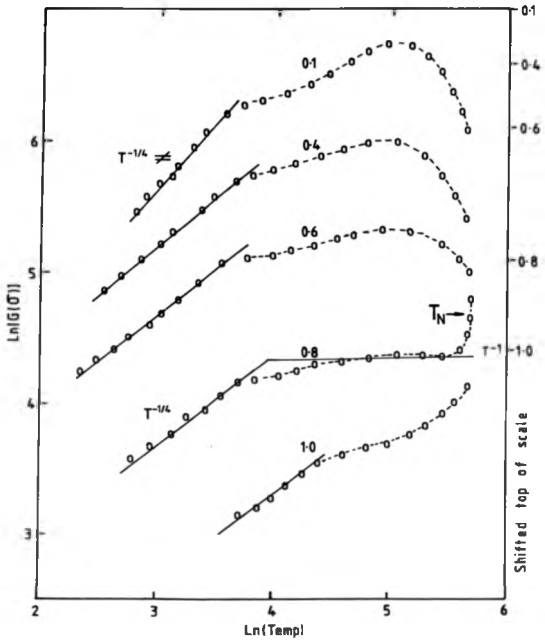

Figure 5:20 A plot of $\mathrm{Ln}|G(\sigma)|$ for $Zn_XFe_{3-X}O_4$ with $0 \leq X \leq 1$ versus temperature. The $T^{-1/4}$ law is indicated by the solid line.

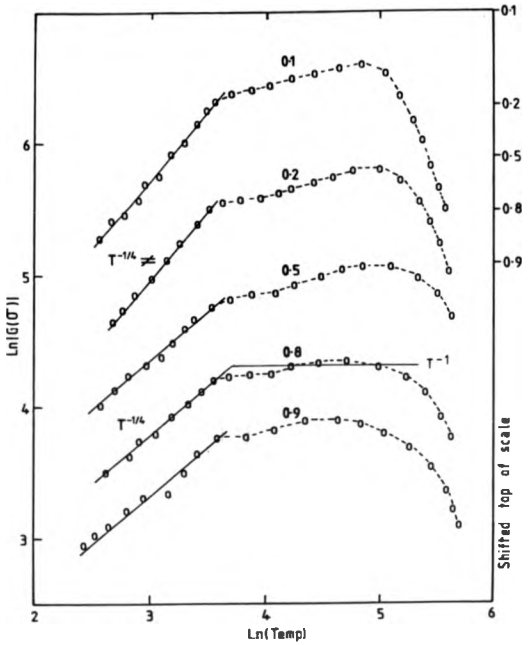

Figure 5:21 A plot of $\mathrm{Ln}|G(\sigma)|$ for $Mn_xFe_{3-x}O_4$ with $0 \leq X < 1$ versus temperature. The $T^{-1/4}$ law is indicated by the solid line.

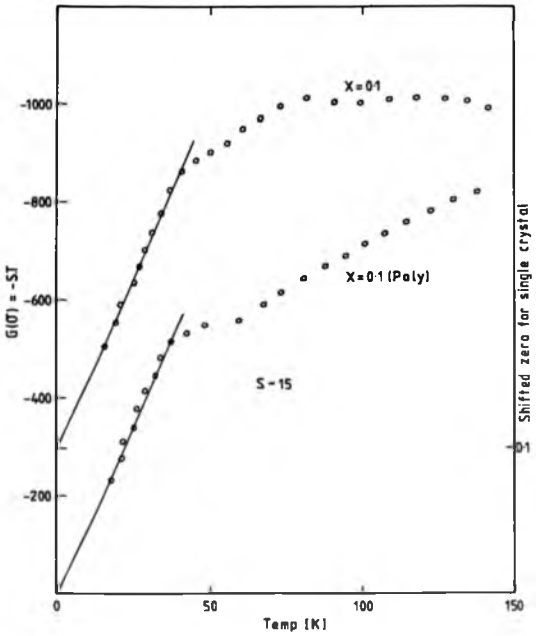

Figure 5:22 $G(\sigma)$ versus temperature for $Zn_XFe_{3-X}O_4$ with $X \leq 0.1$. The solid lines have a slope$\sim$15.

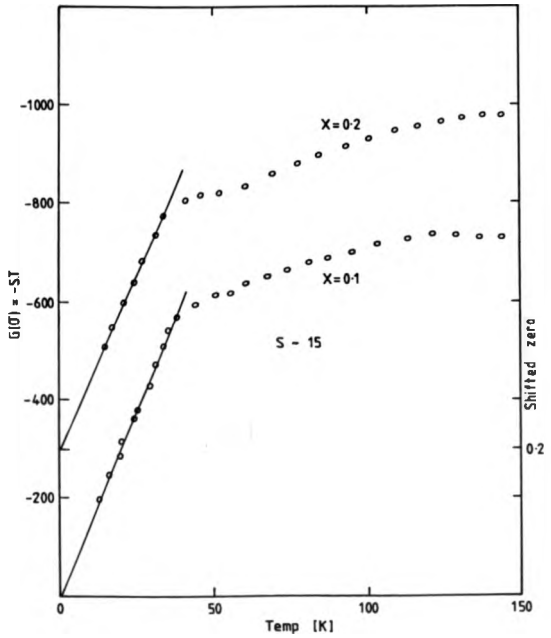

Figure 5:23 $G(\sigma)$ versus temperature for $Mn_XFe_{3-X}O_4$ with $X \leq 0.2$. The solid lines have a slope$\sim$15.

for low values of X a $T^{-1/4}$ law is not found, but a straight line does exist. This latter behaviour will be dealt with later in this section and is interpreted as "many-electron" or "variable number" hopping conduction (Pollak, (1980)). The $T^{-1/4}$ law regime is taken as variable-range hopping conduction in a region of constant density of states i.e. $N(E)=N_0$.

Not one of the graphs show the conductivity to have a $T^{-1/2}$ law (Efros and Shklovskii, (1975)). Graener et al (1979) fitted their results on $Fe_3O_{4-X}F_X$ to a $T^{1/4}$ law, as did Kuipers (1978) who investigated $Ti_XFe_{3-X}O_4$ and Simsa et al (1988) who looked at $Mn_XFe_{3-X}O_4$. Whall et al (1986) also described their measurements in terms of a $T^{1/4}$ law, and demonstrated further that a $T^{1/2}$ law was inappropriate.

By plotting $G(\sigma)$ versus $T^{3/4}$, T_0 can be found more accurately by calculating the gradient. The values of T_0 for zinc and manganese ferrite are given in Tables 5.3-5.4 respectively. Whall et al (1986) finds for nickel ferrite $T_0 \sim 10^8$K. Using a square band approximation in equations (5.6) and (5.7) the density of states can be shown to be $N_0=(0.5\text{-}c+c^2)/(Wa^3)$, where $c=(1-X)/2$ and $W \sim k.G(\sigma T)$, assuming no polaron contribution — this is justified in section 5.6.3. Substituting this density of states approximation and $T_0 \sim 10^7$K (Tables 5.3-5.4) into $T_0=\beta\alpha^3/kN_0$ (equation 2.21), where α^{-1} is the radius of localization and $\beta=21.2\pm1.2$ (Efros and Shklovskii, (1984)) the value of $\alpha a \sim 8$ is calculated.

Mott (1968) gives for the temperature at which the conduction changes from variable-range to nearest-neighbour hopping:

$$kT_1 \sim \frac{W}{\alpha a} \tag{5.13}$$

Pollak and Knotek (1979) obtain a similar expression (equation (2.37)). The intersection of the two lines representing the $T^{-1/4}$ and T^{-1} shown in figures [5.20-5.21] is taken as the transition temperature T_1. The values of αa obtained from (5.13) are shown in Tables 5.3-5.4, and are of the order of 8-9 for both manganese and zinc

ferrite, compared to $\alpha a \sim 5$ for nickel ferrite (Whall et al (1986)). For the nearest-neighbour hopping distance:-

$$a = \frac{a_0}{\sqrt{8}} \tag{5.14}$$

where $a_0 \cong 8.4$Å (the lattice parameter for Fe_3O_4 and all X for zinc ferrite (Gillot et al, (1981)). Using equation (5.14) the radius of localization (i.e. α^{-1}) can be calculated and found to be $\alpha^{-1} \sim 0.37 \pm 0.07$Å (see Tables 5.3-5.4). Nickel ferrite (Whall et al, (1986)) has a radius of localization of 0.44 ± 0.04Å. This indicates that all three ferrite systems, nickel, zinc and manganese, have very similar localization radii.

Many-Electron Hopping — X<0.4

The compositions of manganese and zinc ferrite (X<0.4) that did not show a $T^{1/4}$ law are now considered. Because of the high concentration of electrons on the B-sites it is possible that we have been observing "many electron" or "variable number" hopping conductivity at low temperatures (Mott (1976), Pollak and Knotek, (1979)). For this type of conduction Pollak and Knotek's (1979) analysis gives (equation (2.47)):-

$$\sigma = A.T^S \tag{5.15}$$

where A and S are constants and $S \gg 1$. Differentiating with respect to (1/T) then,

$$G(\sigma) = \frac{\mathrm{dLn}(\sigma)}{d(1/T)} = -S.T \tag{5.16}$$

Figures [5.22-5.23] show plots of $G(\sigma)$ versus temperature for zinc and manganese ferrites. The gradients of the straight lines are ~15. Pollak and Ortuno (1985) give a typical value of S~20. Whall et al (1986) calculated gradient values of ~10 for nickel ferrite. Therefore, many-electron hopping has possibly been observed in these two ferrite systems. From section 2.3.5 $S = 3\alpha a/2\mathrm{Ln}2$ which gives $\alpha a \sim 7$ for zinc and manganese ferrite (see Tables 5.3-5.4). These values compare favourably with those

obtained from the variable–range to nearest–neighbour hopping transition using equation (5.13).

Referring to figures [5.13–5.14] the increasing slope of $G(\sigma T)$ versus temperature for decreasing temperature is interpreted as the development of a Coulomb Gap (see section 5.5.1). The conductivity and activation energy across the Gap are given by:–

$$\sigma \propto T^{-1} EXP(-E_G/2kT) \quad \text{and} \quad k.G(\sigma T) = -E_G/2 \tag{5.17}$$

where E_G is the width of the Coulomb Gap. For both manganese and zinc ferrite $E_G/2 \sim 0.07$eV. Whall et al (1986) calculate the same value for nickel ferrite.

Pollak and Knotek (1979) give for the transition temperature to many–electron hopping:

$$kT_2 = \frac{E_G}{4\alpha a} \tag{5.18}$$

As a crude approximation, T_2 will be taken as the temperature at which equation (5.16) breaks down. Using $T_2 \sim 42$K for both zinc and manganese ferrite and $\alpha a \sim 7$ (see Tables 5.3–5.6) $E_G/2 \sim 0.05$eV. This value is in good agreement with the value calculated using equation (5.17) considering the approach taken.

5.6 Analysis of the Thermopower Results

As can be seen in figures [5.10-5.12] the thermopower has a peak at approximately 70K (T_S) for all X. The thermopower data will be sectioned at these peaks duplicating the approach taken for G(σT) data. To the right of the peak the data regime will be labeled "High Temperatures" and to the left labeled "Low Temperatures".

Analysis of the data will make extensive use of the relationship for the Peltier heat (Zvyagin, (1973)),

$$\epsilon\Pi = \frac{\int N(E).(E - E_f).dE}{\int N(E).dE} \tag{5.19}$$

5.6.1 High Temperatures — $T > T_S$

It is convenient to separate the data into two categories once more, corresponding to high and low X.

Case A where X≥0.6

Here we replace our presumably more accurate Gaussian density of states (equation (5.8)) by a rectangular band,

$$N(E) \begin{cases} = N_0 & \text{for } 0<E<B \\ = 0 & \text{otherwise} \end{cases} \tag{5.20}$$

with $E_f<0$, and write for the concentration of carriers:

$$c = \frac{\int_0^B \frac{N(E)}{1 + EXP(E - E_f)/kT}.dE}{\int_0^B N(E).dE} \tag{5.21}$$

where c=(1-X)/2, giving the Fermi energy:

$$E_f = kT.Ln\left[\frac{e^{Bc/kT} - 1}{1 - e^{B(c-1)/kT}}\right] \qquad (5.22)$$

The logarithm can only be expanded if $-1 \leq Bc/kT \leq 1$ and $-1 \leq B(c-1)/kT \leq 1$, which dictates that $B \leq kT$. Assuming these limits are fulfilled the Fermi level is:-

$$E_f \sim kT.Ln\left[\frac{c}{1-c}\right] + \frac{B}{2} + \frac{B^2(2c-1)}{24kT} + \cdots\cdots \qquad (5.23)$$

From $\Pi = ST$ and $e\Pi = B/2 - E_f$ (i.e. $e\Pi = E - E_f$) then,

$$S \sim -\frac{k}{e}\left[Ln\left[\frac{c}{1-c}\right] + \left[\frac{B}{kT}\right]^2\left[\frac{2c-1}{24}\right]\right] \qquad (5.24)$$

Plotting $\Pi.T$ versus T^2 then the gradient will be $k/e.Ln[(1-X)/(1+X)]$ and the intercept $B^2X/(24ke)$. Equation (5.24) indicates that the thermopower appears to "look like" Heikes law (equation 3.5), but it has the opposite sign. Also, the intercept for all the experimental plots has a negative value whereas equation (5.24) gives a positive value. If only the magnitude of the gradient and intercept are considered, then the values of X calculated from the gradient give an average accuracy greater than 10%, and the bandwidth greater than kT from the intercept — but $B > kT$ violates the limits for expansion. Therefore, another approach needs to be considered with the bandwidth possibly greater than kT.

Whall et al (1984) have considered a constant density of states with $B > kT$ and the Fermi level in the gap and they calculate the Fermi level to be:-

$$E_f = kT.Ln(c) + kT.Ln\left[\frac{B}{kT}\right] \qquad (5.25)$$

Therefore,

$$S = \frac{1}{eT}\left[\frac{B}{2} - kT.Ln(c) - kT.Ln\left[\frac{B}{kT}\right]\right] \qquad (5.26)$$

To test the validity of equation (5.26) the thermopower activation energy is calculated by differentiating with respect to 1/T. The activation energy is:-

$$G_S = \frac{dS}{d(1/T)} = -\frac{B}{2e} + \frac{kT}{e} \tag{5.27}$$

N.B. Whall et al (1984) calculate

$$\frac{G(\sigma T).k}{e} \sim -\frac{B}{2e} + \frac{kT}{e} \tag{5.28}$$

which is identical.

By plotting the thermopower versus the reciprocal of the temperature the activation energy (G_S) can be calculated from the slope. The plots of thermopower versus 1000/T for $Zn_{0.8}Fe_{2.2}O_4$ and $Mn_{0.8}Fe_{2.2}O_4$ are shown in figure [5.24] and [5.25] respectively. The bandwidths for zinc and manganese ferrite are calculated using equation (5.27) and are shown in Tables 5.3–5.4: all the bandwidths are greater than kT. Using these bandwidths in equation (5.26) the value of X is found at T=290K and compared with those experimentally found using EPMA — see Tables 5.1 -5.2 and section 4.2.2. It is easily seen that the two values of X agree to within 7%. Srinivasan and Srivastava (1981) have also compared thermopower data for various values of zinc ferrite with Ln(c) — derived from the electrical neutrality equation — and show good agreement with the present work (see Table 3.1). For lower values of X the EPMA and thermopower results give different values of X, presumably because the condition $E_f<0$ no longer applies.

When the Fermi level is in the gap the conductivity and thermopower activation energy should agree (see equations (5.27–5.28)), if not then the "extra" energy may be due to a polaron contribution. (For $X \geq 0.8$ it is possible that a small polaron hopping may have been observed — see section 5.5 subsection II). Therefore,

$$G(\sigma T).k/e - G_S = W_P \tag{5.29}$$

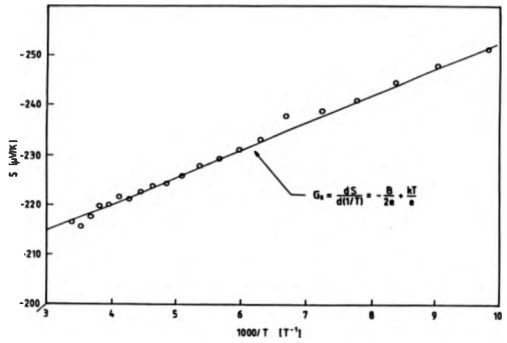

Figure 5:24 Thermopower versus 1000/Temperature for $Zn_{0.8}Fe_{2.2}O_4$

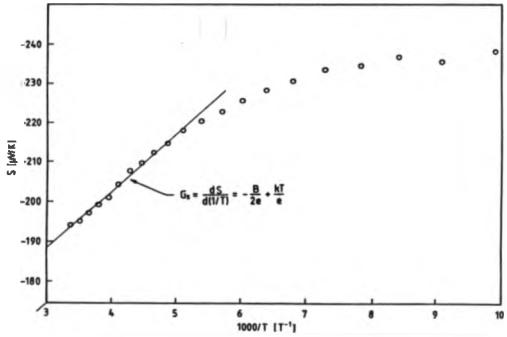

Figure 5:25 Thermopower versus 1000/Temperature for $Mn_{0.8}Fe_{2.2}O_4$

where W_P is the polaron activation energy. Only $X \geq 0.65$ for manganese ferrite can be considered and not zinc, because of the reasons mentioned above (see section 5.5.1). Equation (5.29) gives $W_P > 0$ and if an adiabatic polaron has been observed then W_P is 0.026eV and 0.029eV for $Mn_{0.8}Fe_{2.2}O_4$ and $Mn_{0.9}Fe_{2.1}O_4$ respectively. However, if the the polaron is of the non-adiabatic type then $G(\sigma T^{3/2}).k/e$ should be used and not $G(\sigma T).k/e$. The relationship between $G(\sigma T^{3/2})$ and $G(\sigma T)$, using equation (5.4), can be shown to be:-

$$G(\sigma T) = G(\sigma T^{3/2}) + \frac{T}{2} \tag{5.30}$$

Whall et al (1987) have analysed $MnFe_2O_4$ for $T \geq 300K$ using the non-adiabatic polaron hopping model, and assuming that the conductivity activation energy (W) is equal to $G(\sigma T^{3/2}).k$ they obtain $W_P = 0.04eV$ for $MnFe_2O_4$ at T=300K. Using $G(\sigma T^{3/2}).k$ at T=290K for both $Mn_{0.8}Fe_{2.2}O_4$ and $Mn_{0.9}Fe_{2.1}O_4$ the polaron term was calculated to be 0.038eV and 0.041eV respectively, thus indicating good agreement.

Case B — $X \leq 0.6$

Here we assume a rectangular band once more but with $E_f > 0$. For this case, Whall (1981) finds from an Effective Medium Theory, making the assumption that the density of states is approximately constant but slowly varying with energy, the thermopower to be:

$$S = A/T + B.T \tag{5.31}$$

and from the Kelvin-Onsager relation $S = \Pi/T$ the Peltier heat is:-

$$\Pi = A + BT^2 \tag{5.32}$$

Because $e\Pi = E - E_f$ then "A" $= -E_f(0)$; a direct indication of where the Fermi level is at T=0K. Graphs showing plots of $e\Pi$ versus T^2 are shown in figures [5.26-5.27]. For low X the fit is quite pronounced, but the length of fit reduces as X increases. In our

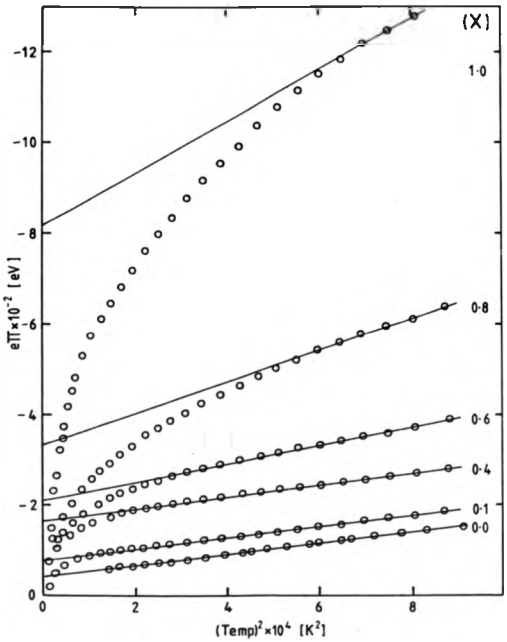

Figure 5:26 A plot of eΠ versus the square of the temperature for $Zn_XFe_{3-X}O_4$ with $0 \leq X \leq 1$. The number of data points fitting the solid line falls for increasing X.

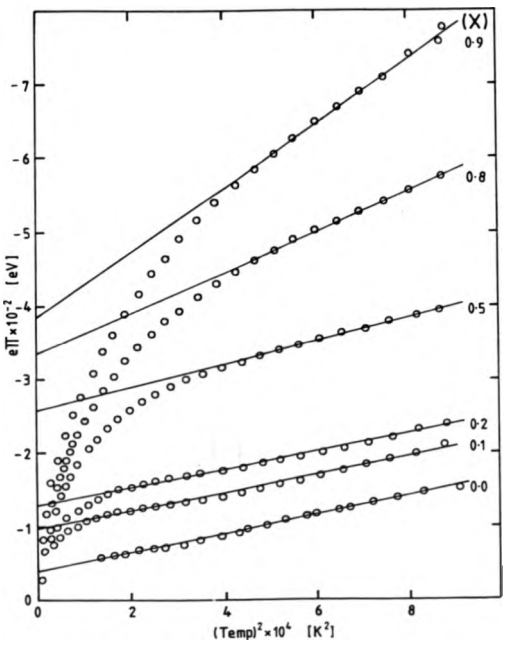

Figure 5:27 A plot of eΠ versus the square of the temperature for $Mn_XFe_{3-X}O_4$ with $0 \leq X < 1$. The number of data points fitting the solid line falls for increasing X.

picture, low values of X have electron–electron interaction effects and high values of X a small polaron contribution (see section 5.5.1 and 5.6.1 Case A respectively), therefore this picture is only applicable to 0.4<X<0.65. As can be seen in figures [5.26–5.27] $Zn_{0.6}Fe_{2.4}O_4$ and $Mn_{0.5}Fe_{2.5}O_4$ show good agreement.

For X<0.65 where W_P is expected to be small and E_f is slowly varying with temperature we can assume that W∼G(σT).k. From equation (5.32) eΠ=−E_f(T) and equation (5.6):–

$$\frac{G(\sigma T).k}{E_{f(T)}} = \int_0^{E_{f(T)}/b} \frac{2exp(-t^2/2)}{\sqrt{2\pi}}.dt \; + \; \left[\frac{b}{E_{f(T)}}\right] \frac{2exp(-E_{f(T)}/2b)}{\sqrt{2\pi}} \qquad (5.33)$$

Using normal distribution tables the bandwidth (B=2b) at room temperature can be calculated, which are shown in Tables 5.3–5.4.

5.6.2 Bandwidth

As explained in above, for X≥0.65 B is taken from the thermopower data and X<0.65 B is taken from the conductivity data and thermopower data. It is clear that a peak occurs and this feature can possibly be explained by analysing the ionic disorder of the ferrite system, because as discussed in the Theory chapter (section 2.2.3) the disorder influences the bandwidth. The ionic formulae of manganese and zinc ferrite are given in equations (5.2–5.3). Assuming the concentration on the A-sites has a binomial distribution, the standard deviation of the cation distribution is proportional to $\sqrt{X.(1-X)}$ (i.e. σ^2=npq). This function is plotted on the same figure [5.28] as the bandwidths for the two ferrite systems. All three plots show a peak with both sides falling to 0. Clearly, the disorder on the A–sites plays a major role in determining the width of the conduction band.

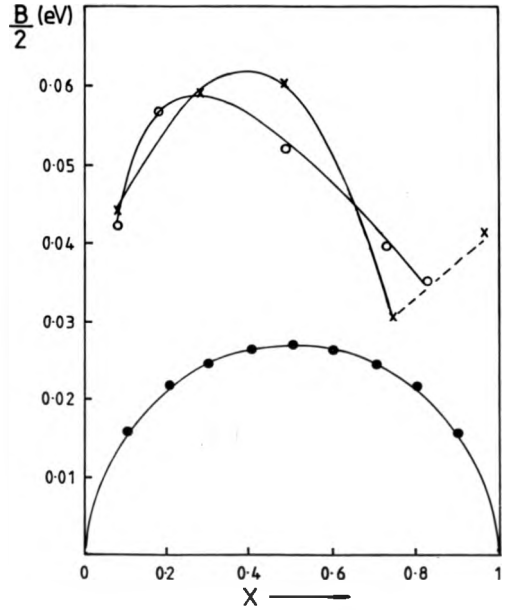

Figure 5:28 The calculated half-bandwidths plotted versus X; x: $Zn_XFe_{3-X}O_4$; o: $Mn_XFe_{3-X}O_4$. •: $A\sqrt{X(1-X)}$ — the the expected half-bandwidth curve due to disorder on the A-sites.

Non-linear screening in lightly doped and highly compensated semiconductors has been considered by Shklovskii and Efros (1971). They argued that the standard deviation of the fluctuations in impurity concentration is given by:-

$$b \propto \frac{N_t^{2/3}}{n^{1/3}} \tag{5.34}$$

where N_t is the total impurity concentration and n the electron concentration. Using a binomial approximation in equation (5.34), the bandwidth can be shown to be:-

$$b \propto X^{1/3} \tag{5.35}$$

where X is the cation concentration. Obviously, from figure [5.28], equation (5.35) does not correlate with the bandwidth. Therefore, screening of the impurity atoms by the electrons does not seem to play a major role in determining the width of the band.

5.6.3 Comparison of G(σT) and eΠ

Here we make use of the rectangular band approximation once more.

Figure [5.29] shows G(σT).k-eΠ versus X at T=290K. For X<0.65, G(σT).k ∼W (see above) and W→eΠ as X→0.6 in agreement with equations (5.6) and (5.19). For X>0.6 where eΠ=W, G(σT).k≠W as can easily be seen from equations (5.6), (5.25) and (5.27), which suggest |eΠ|>|k.G(σT)|. The results for manganese ferrite are clearly in agreement with this interpretation whereas, this is not so for zinc ferrite. The discrepancy is possibly explained as being due to an increase of G(σT) due to magnetic disorder for X=0.8 and due to grain boundaries for the polycrystalline sample X=1.0. Similar behaviour is seen when the data at T=200K, figure [5.30], are examined. At T=150K, figure [5.31], the behaviour may be explained by assuming E_f(150K)>0 for all X in which case k.G(σT)∼W and W→eΠ at high X. This behaviour is consistent with equation (5.6) and (5.19) and with a negligible

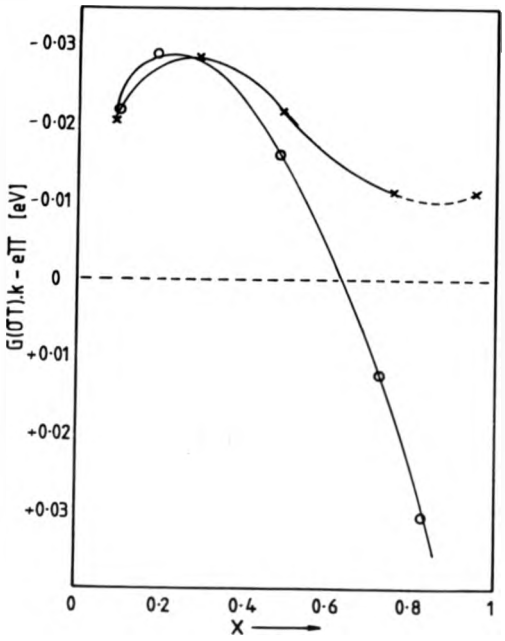

Figure 5:29 A plot of $G(\sigma T)-e\Pi$ versus X at room temperature; o: $Mn_XFe_{3-X}O_4$; ×: $Zn_XFe_{3-X}O_4$.

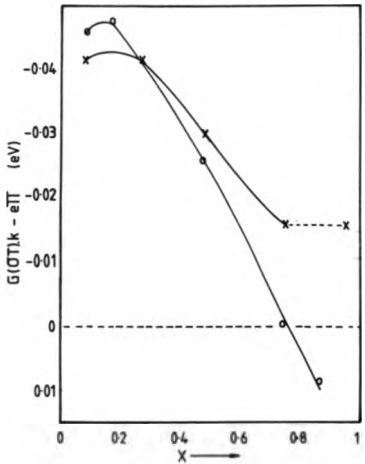

Figure 5:30 A plot of G(σT)–eΠ versus X at T=200K; o: $Mn_XFe_{3-X}O_4$; ×: $Zn_XFe_{3-X}O_4$.

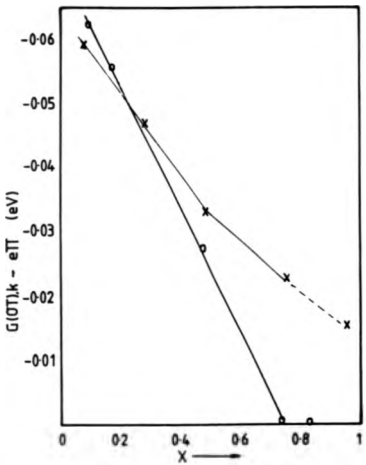

Figure 5:31 A plot of G(σT)–eΠ versus X at T=150K; o: $Mn_XFe_{3-X}O_4$; ×: $Zn_XFe_{3-X}O_4$.

value of W_P at T=150K. The absence of a maximum in figure [5.31] as compared to figure [5.29], is attributed to the formation of a Coulomb Gap at low temperatures which could enhance W without increasing eII.

5.6.4 Low Temperatures — $T<T_S$

Case A $X \geq 0.4$

The peak in the thermopower of $Ni_XFe_{3-X}O_4$ with $0.4 \leq X \leq 0.8$ has been interpreted by Whall et al (1986) as being associated with variable-range hopping having energies comparable with the energy bandwidth of conduction states and show:-

$$S = \Pi/T = \frac{(E_M - E_f)}{2eT} \tag{5.36}$$

for a rectangular density of states function. $E_M = kT_0^{1/4}T^{3/4}$ is the energy width of states above E_f contributing to the conduction and $E_f(>0)$ is the energy width of states below the Fermi energy contributing to the conduction. The thermopower maximum then occurs at a temperature:-

$$T_S \sim \left[\frac{4E_f}{kT_0^{1/4}}\right]^{4/3} \tag{5.37}$$

The values of T_S calculated from equation (5.37) are in fair agreement with the measured ferrite data.

In the case of nickel ferrite the $T^{-1/4}$ law in the conductivity extends to temperatures above T_S. Unfortunately, this is not true for zinc and manganese ferrite (see figures [5.20–5.21]) and so equation (5.36) will overestimate the thermopower for $T>T_1$ (see section 5.5.2). Therefore, a modified procedure has been adopted. Noting that the maximum value of E_M is B–E_f and that the conductivity activation energy increases with temperature until the nearest-neighbour hopping regime commences

at T_{NN}, whereupon $G(\sigma T)$ saturates, we write:-

$$E_M = \left[\frac{T}{T_{NN}}\right]^{3/4} (B - E_f(0)) \tag{5.38}$$

To calculate the Fermi energy we put:-

$$E_f(0) = \frac{(1-X)}{2} B \tag{5.39}$$

and to obtain a reasonable agreement with the data we take $B=2\sqrt{2}b$, somewhat larger than the value assumed in section 5.6.2. The values of 2b are given in Tables 5.3-5.4. For $Zn_{0.8}Fe_{2.2}O_4$ and $Mn_{0.8}Fe_{2.2}O_4$ T_{NN}~140K. Calculated and experimental values for $Zn_{0.8}Fe_{2.2}O_4$ and $Mn_{0.8}Fe_{2.2}O_4$ are shown in figures [5.32-5.33]. Considering the crudeness of the calculations the result must be considered as encouraging. An improved fit would require more detailed knowledge of the density of states function and of $E_M(T)$. The magnitudes, shapes and peaks of the theoretical curves are in approximate agreement with the experimental results.

At temperatures $T_1 \ll T_S$ corresponding to $W \ll 2\sqrt{2}b$ we expect, following Zvyagin (1973), Overhof (1975) and Kosarev (1975), that $S \propto T^{1/2}$ and $Ln\sigma \propto T^{-1/4}$. It has been possible to measure electrical conductivity at temperatures down to 7K and to see the expected $T^{-1/4}$ behaviour. $S \propto T^{1/2}$ has not been confirmed for thermopower as shown in figures [5.32-5.33]. However, this may be due to the fact that it has only been possible to measure the thermopower down to ~20K.

Case B X<0.4

In the present picture we interpret the peak in the thermopower for X<0.4 as being due to the transition from excitations across a Coulomb Gap to many electron hopping. We might expect $T_{NN} > T_S \sim T_2$ where T_2 is the temperature of onset of the law for σ given by equation (5.16). Tables 5.5-5.6 show this is indeed the case. Whall et al (1986) conjecture that in the region $T<T_2$ the thermopower varies roughly as T. Unfortunately, our thermopower data do not extend to low enough temperatures to test this suggestion.

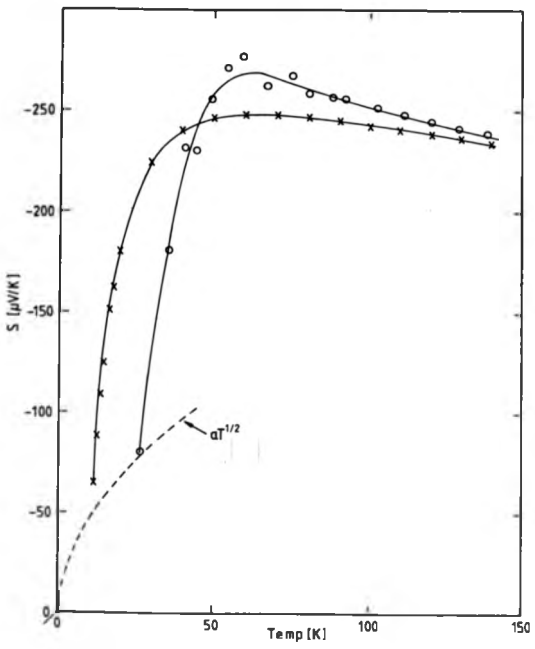

Figure 5:32 Thermopower of $Zn_{0.8}Fe_{2.2}O_4$ versus temperature;
o: measured; ×: calculated using equation (5.38).

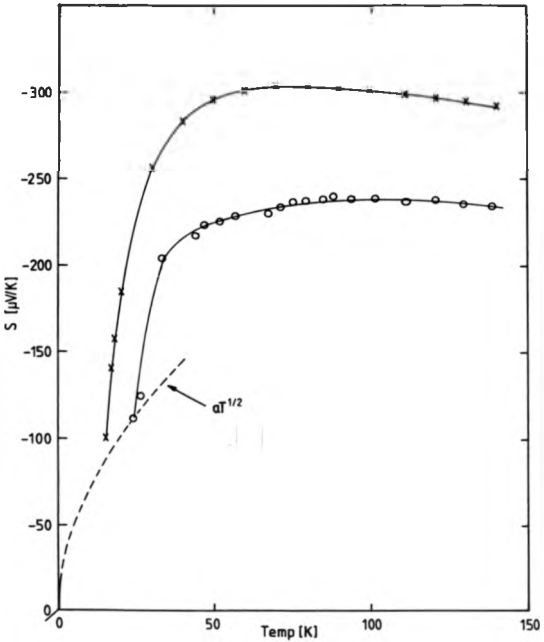

Figure 5:33 Thermopower of $Mn_{0.8}Fe_{2.2}O_4$ versus temperature; o: measured; x: calculated using equation (5.38).

Table 5.1: EPMA results and calculated values of X using Ln[(1-X)/2] — see section 5.6.1 — for $Zn_XFe_{3-X}O_4$

Nominal X value	Measured X value	Calculated X value
0.0	0.00	--
0.1	0.08 (Poly)	--
0.1	0.08	--
0.4	0.29	--
0.6	0.48	0.43
0.8	0.76	0.81
1.0	0.96 (Poly)	0.97

Table 5.2: EPMA results and calculated values of X using Ln[(1-X)/2] — see section 5.6.1 — for $Mn_XFe_{3-X}O_4$

Nominal X value	Measured X value	Calculated X value
0.0	0.00	--
0.1	0.09	--
0.2	0.17	--
0.5	0.47	0.36
0.8	0.73	0.71
0.9	0.84	0.85

Table 5.3: Zinc Ferrite.

Value X	T_0 (K)$\times 10^7$	B (eV)	αa	α^{-1} Å	T_N (K)
0.0	--	--	--	--	830
0.1	--	0.088	6.9	0.43	780
0.4	3.0	0.118	9.0	0.33	710
0.6	2.4	0.123	9.8	0.30	580
0.8	2.3	0.061	8.0	0.37	290
1.0	--	0.081	--	--	<30

Table 5.4: Manganese Ferrite.

Value X	T_0 (K)$\times 10^7$	B (eV)	αa	α^{-1} Å	T_N (K)
0.0	--	--	--	--	830
0.1	--	0.085	6.9	0.43	810
0.2	--	0.115	6.9	0.43	780
0.5	0.9	0.104	8.3	0.36	725
0.8	1.8	0.079	7.8	0.38	650
0.9	0.7	0.071	8.2	0.36	550

Table 5.5: Zinc Ferrite.

Value X	T_S (K)	T_G (K)	T_1 (K)	T_2 (K)	T' (K)	G_S (eV)
0.1	63±14	125	--	43	--	--
0.4	46±10	165	60	--	50	--
0.6	53±10	215	50	--	47	--
0.8	61±10	--	55	--	47	-0.0056
1.0	80±10	--	--	--	--	-0.0157

Table 5.6: Manganese Ferrite.

Value X	T_S (K)	T_G (K)	T_1 (K)	T_2 (K)	T' (K)	G_S (eV)
0.1	51±10	140	--	42	--	--
0.2	51±10	160	--	38	--	--
0.5	75±14	205	53	--	41	--
0.8	94±15	217	45	--	34	-0.0146
0.9	78±22	235	45	--	34	-0.0109

Chapter 6

SUMMARY and CONCLUSION

The most detailed investigation of the electrical properties of zinc and manganese ferrous ferrites reported to date has been carried out. It has been demonstrated that the results may be interpreted in terms of hopping in a disordered medium, modified to some extent by electron-electron interaction and polaron effects. Specific achievements are as follows:

I) Silicon diodes have been shown to offer advantages for resistivity and thermopower measurements.

II) Data of improved accuracy as compared to previous works has been presented.

III) Percolation theory predictions (equations (5.6) and (5.19)) for the conductivity activation energy and the Peltier heat have been shown to give a satisfactory description of the results.

IV) Estimates have been made of the energy widths ("Bandwidths") of conduction states and their variation with X has been described in terms of the theory.

V) The theory has been used to account for the variation of ther-

mopower S as Ln(c) at high X.

VI) The characteristic shape of the thermopower temperature curve near the peak in S has been accounted for.

VII) The formation of a Coulomb Gap at low X has been inferred from the data.

VIII) Evidence has been presented for many-electron hopping at low temperatures and low X.

IX) An analysis of the variable range hopping and many-electron hopping, etc, has led to a value for the effective radius of the electronic state ($\sim$0.4Å).

X) A polaron contribution ($\sim$0.04eV) to the conductivity activation energy at 300K of $Mn_{0.8}Fe_{2.2}O_4$ and $Mn_{0.9}Fe_{2.2}O_4$ has been deduced.

XI) No evidence was found for the much quoted $Ln\sigma \propto T^{-1/2}$ variation predicted for variable-range hopping in a Coulomb Gap.

Further work should include efforts to extend the measurements down below 20K, in order to test the prediction that $S \propto T^{1/2}$ for the low temperature limit of variable-range hopping. Measurements of Hall mobility and magnetorestistance over a wide range of temperatures should also be made for detailed comparisons with theory.

REFERENCES

Adler D., Solid State Phys., (1968), **21**, 1.

Ambegaokar V., Halperin B.L. and Langer J.S., Phys. Rev. B. (1971), **4**, 2612.

Anderson P.W., Phys. Rev., (1956), **102**, 1008.

Anderson P.W., Phys. Rev. (1958), **109**, 1492.

Austin I.G. and Mott N.F., Adv. Phys., (1969), **18**, 41.

Barlow R.D., Jones M.R.B., Phillips P.J., Pointon A.J. and Whall T.E., J. Appl. Phys., (1987), **61**, 3546.

Barlow R.D., (1991), To be published.

Blatt F.J., Flood D.J., Rowe V. and Schroeder P.A., Phys. Rev. Lett., (1967), **18**, 395.

Böttger H. and Bryksin V.V., Solid State Comm., (1977a), **23**, 227.

Böttger H. and Bryksin V.V., Phys. Stat. Sol. (b), (1977b), **80**, 569.

Böttger H. and Bryksin V.V., Phys. Stat. Sol. (b), (1977c), **81**, 97.

Böttger H. and Bryksin V.V., Phys. Stat. Sol. (b), (1977d), **81**, 433.

Brabers V.A.M., Phys. Stat. Sol., (1969), **33**, 563.

Brabers V.A.M., J. Crystal Growth, (1971), **8**, 26.

Caldwell F.R., (1965), Temeratures of thermocouple reference junctions in an ice bath, Journal of Research NBS-C, Engineering and Instruments, 69, C-11.

Camphausen D.L, Coey J.M.D. and Chakraverty B.K., Phys. Rev. Lett., (1972), **29**, 657.

Cole B.C., Electronics (magazine), (1989), 88.

Crevecoeur C. and Wit H.J., J. Phys. Chem. Solids, (1970), **31**, 783.

Cullen J.R and Callen E., J. Appl. Phys., (1970), **41**, 879.

Cullen J.R and Callen E., Phys. Rev. Lett., (1971), **26**, 236.

Cullen J.R and Callen E., Phys. Rev. B., (1973), **7**, 397.

Edwards J.T. and Thouless D.J., J. Phys. C., (1972), **5**, 807.

Efros A.L., J. Phys. C, (1976), **9**, 2021.

Efros A.L. and Shklovskii B.I., J. Phys. C., (1975), **8**, L49.

Efros A.L. and Shklovskii B.I. : "Electronic Properties of Doped Semiconductors", (1984), Springer Verlag series.

Emin D., Electronic and Structural Properties of Amorphous Semiconductors, Ed. P.G. Comber and J. Mort, (1973).

Emin D., Phys. Rev. Lett., (1974), **32**, 303.

Emin D., Adv. Phys., (1975), **24**, 305.

Emin D., Phys. Rev. Lett., (1975), **35**, 882.

Fleishman L., Licciardello D.C. and Anderson W.P., Phys. Rev. Lett., (1978), **40**, 1340.

Funatogawa Z., Miyata N. and Usami S., J. Phys. Soc. Japan, (1959), **14**, 854.

Gibbons D.J. and Spear W.E., J. Phys. Chem. Solids, (1966), **27**, 1917.

Gillot B., Phys. Stat. Sol. (a), (1982), **69**, 719.

Gillot B., Benloucif R.M. and Rousset A., Phys. Stat. Sol. (a), (1981), **65**, 205.

Gillot B. and Jemmali F., Phys. Stat. Sol. (a), (1983), **76**, 601.

Graener H., Rosenberg M., Whall T.E. and Jones M.R.B., Phil. Mag. B, (1979), **40**, 389.

Grieg D. and Harrison J.P., Phil. Mag., (1965), **12**, 71.

Griffiths B.A., Elwell D. and Parker R., Phil. Mag., (1970), **22**, 163.

Gronvold F.and Sveen A., J. Chem. Thermoodyn., (1974), **6**, 859.

Hall J.A., "The Measurement of Temperature", Chapman and Hall Ltd., (1966), 23.

Hastings J.M. and Corliss L.M. Phys. Rev., (1956), **104**, 328.

Heikes R.R. and Ure R.W. Jr., "Thermoelectricity": Science and Engineering (Interscience Publishers Inc. New York London), (1961).

Hill R.M., Phys. Stat. Sol. (a), (1976), **35**, K29.

Holstein T., Ann. Phys., (1959), **8**, 325.

Horowitz P. and Hill W., "The Art of Electronics", Cambridge University Press, 2nd Ed., (1989).

Hust J.G., Rev. of Sci. Instr., (1970), **41**, 622.

Igra R.A., Rao M.G. and Scurlock R.G., International Cryogenic Engin. Conf. Berlin 11, Procs., (1986), 617.

Ihle D. and Lorenz B., Phys. Stat. Sol. (b)., (1973), **58**, 79.

Ihle D. and Lorenz B., Phys. Stat. Sol. (b)., (1974), **63**, 599.

Ihle D. and Lorenz B., Phil. Mag. B, (1980), **42**, 337.

Ihle D., Phys. Stat. Sol. (b), (1984), **121**, 217.

Jones M.R.B., Thesis: "Preparation and Electrical Properties of Ferrous ferrites", Portsmouth Polytechnic, (1985).

Jones R. and Schaich W., J. Phys. C, (1972), **5**, 43.

Jonker G.H., J. Phys. Chem. Solids, (1959), **9**, 165.

Keem J., Chemical Instrumentation, (1975), **6(2)**, 133.

Kirkpatrick S., Proceedings of the 11th International Conference, Garmisch, (1974), 183.

Knotek M.L., Pollack M., Donovan T.M. and Kurtzman H., Phys. Rev. Lett., (1971) **30**, 853.

Kohane T. and Silverman B.D., J. Phys. Soc. Japan, (1962), **17**, 249.

Kopp J. and Slack G.A., Cryophysics, (1971), 22.

Kosarev V.V., Sov. Phys. Semicond., (1975), **8**, 897.

Kuipers A.J.M., Thesis: "Electrical Transport in the Mixed Series $Fe_{3-x}Ti_xO_4$", Eindhoven University, Holland, (1978).

Landolt–Börnstein, II Band, 6 Teil, Springer–Verlag, (1959), 931.

Lavine J.M., Phys. Rev., (1959), **114**, 482.

Lotgering F.K., J. Phys. Chem. Solids, (1964), **25**, 95.

Lorenz B. and Ihle D., Phys. Stat. Sol. (b)., (1975), **68**, K189.

Miller A. and Abrahams E., Phys. Rev., (1960), **120**, 745.

Miyata N., J. Phys. Soc. Japan, (1961), **16**, 206.

Miyahara Y., J. Phys. Soc. Japan, (1972), **32**, 629.

Mobius A., Elefant D., Heinrich A., Muller R., Schumann J., Vinzelberg H. and Zies G., J. Phys. C, (1983), **16**, 6491.

Mott N.F., Phil. Mag., (1966), **13**, 989.

Mott N.F., Adv. Phys., (1967), **16**, 49.

Mott N.F., J. Non–Crystalline Solids, (1968), **1**, 1.

Mott N.F., "Metal–Insulator Transitions", (1974): (London: Taylor and Francis Ltd), Electronic and Structural Properties of Amorphous Semiconductors, Ed P.G. LeComber and J. Mort (New York: Academic Press), p1.

Mott N.F., J. Phys. C., (1975), **8**, L239.

Mott N.F., Phil. Mag., (1976), **34**, 643.

Mott N.F., Festkörperprobleme **XIX**, (1979), 331.

Mott N.F. and Davis E.A., "Electronic Processes in Non–Crystalline Materials", (1979), 2nd edition, (Oxford: Clarendon).

Mott N.F. and Jones H., (1936), "The Theory of the Properties of Metals and Alloys", (Oxford: Clarendon).

Movaghar B. and Schirmacher W., J. Phys. C., (1981), **14**, 859.

Nicholls G.D., Adv. Phys., (1955), **4**, 113.

Overhof H., Phys. Stat. Sol. (b), (1975), **67**, 709.

Oxford University, Cryogenic Facilities group, Clarendon Laboratory, OXFORD.

Phillips P.J., Whall T.E. and Parker E.H.C., J. Phys. E: Sci. Instrum., (1989), **22**, 986.

Pollak M., (1978), "The Metal Non-Metal Transition in Disordered Systems", (Eds: Friedman and Tunstall, SUSSP).

Pollak M., Phil. Mag., (1980), **42**, 781.

Pollak M. and Knoteck M.L., J. Non-Crystalline Solids, (1979), **32**, 141.

Pollak M. and Ortuño M., Electron Electron Interactions in Disordered Systems, Eds. A.L. Efros and M. Pollak, (1985).

Powell R.L., Caywood L.P. and Bunch M.D., Temperature its Measurement and Control in Science and Industry, Reinhold Publishing Corporation, 3, II, (1962).

Rao M.G., Scurlock R.G. and Wu Y.Y., Cryogenics, (1983), **23**, 635.

Roberts G.G. and Schmidlin F.W., Phys. Rev. B, (1983), **28**, 2001.

Salerno N., Thesis: "Measurements of the electrical properties of ferrite materials", Portsmouth Polytechnic, (1986).

Schieber M., J. Appl. Phys., (1964), **33-35**, 1072.

Shklovskii B.I. and Efros A.L., Sov. Phys. JETP, (1971), **33**, 468.

Simsa Z. and Schneeweis O., Czech. J. Phys., (1972a), **B22**, 1331.

Simsa Z., Simsova J. and Brabers V.A.M., 11 International Conference of the Physics of Semiconductors, (ICPS) Proceedings: Warsaw, (1972b), 2.

Simsa Z. and Brabers V.A.M., IEEE Transactions on Magnetics, (1988), **24**, 1911.

Southampton University, (Data sheet on Silicon Diodes), Institute of Cryogenics, SOUTHAMPTON.

Street G.B. and Gill W.D., Phys. Stat. Sol., (1966), **18**, 601.

Srinivasan G. and Srivastava C.M., Phys. Stat. Sol. (b), (1981), **103**, 665.

Srinivasan G., Phys. Rev. B., (1971), **4**, 2581.

Swartz D.L. and Swartz J.M., Cryogenics, (1974), 67.

Tinsley C.L., Thesis: "A study of the relation between conductivity and magnetic order in magnetite and its solid solutions with nickel and zinc ferrite", Portsmouth Polytechnic, (1975).

van de Pauw L.J., Philips Res. rep., (1958), **13**, 1.

Verwey E.J.W., Nature, (1939), **144**, 327.

Verwey E.J.W. and Heilmann E.L., J. Chem. Phys., (1947), **15**, 174.

Vescan L., Telnic T.M. and Popecu C., Phys. Stat. Sol. (b)., (1972), **54**, 733.

Whall T.E., J. Phys. C., (1981), **14**, L887.

Whall T.E., Rigo M.O., Jones M.R.B. and Pointon A.J., Journal de Physique, (1977), **Tome 38**, C1–229.

Whall T.E., Yeung K.K., Proykova Y.G.and Brabers V.A.M., Phil. Mag. B, (1984), **50**, 689.

Whall T.E., Yeung K.K. and Proykova Y.G., Phil. Mag. B, (1986), **54**, 505.

Whall T.E., Salerno N., Proykova Y.G. and Brabers V.A.M., Phil. Mag. B, (1987), **56**, 99.

White G.K., Experimental Techniques in Low Temperature Physics, Clarendon Press, Oxford, (1979).

Yamzin I.I., Belov N.V. and Nozik Yu.Z., J. Phys. Soc. Japan, (1962), **17**, B–C, 55.

Yeung K.K., Thesis: "Conduction Processes of Ferrites", Portsmouth Polytechnic, (1982).

Zvyagin I.P., Phys. Stat. Sol. (b), (1973), **58**, 443.